THE EFFECTS OF FUNCTIONALIZATION ON ADSORPTION PROPERTIES OF MICROPOROUS MATERIALS

A Dissertation
Presented to
The Academic Faculty

by

Gregory Edward Cmarik

In Partial Fulfillment
Of the Requirements for the Degree
Doctor of Philosophy in the
School of Chemical and Biomolecular Engineering

Georgia Institute of Technology

December 2014

THE EFFECTS OF FUNCTIONALIZATION ON ADSORPTION PROPERTIES OF MICROPOROUS MATERIALS

Approved by:

Dr. Krista S. Walton, Advisor
School of Chemical and Biomolecular Engineering
Georgia Institute of Technology

Dr. Christopher W. Jones
School of Chemical and Biomolecular Engineering
Georgia Institute of Technology

Dr. Yoshiaki Kawajiri
School of Chemical and Biomolecular Engineering
Georgia Institute of Technology

Dr. J. Carson Meredith
School of Chemical and Biomolecular Engineering
Georgia Institute of Technology

Dr. Jake Soper
School of Chemistry and Biochemistry
Georgia Institute of Technology

Date Approved: June 30, 2014

Dedicated to the Katrina class of Tulane University, 2009.

ACKNOWLEDGEMENTS

I would like to thank my mother and father for their support, inspiration, and love. I would like to thank my advisor for her guidance and patience. I would like to thank all of the fellow members of the Walton Research Group: Paul, Kit, Bin, Reddy, Yougui, Yang, Katrina, Christine, Mango, Himanshu, Nick, Karen, Mike, Yang, Ken, and Bogna.

TABLE OF CONTENTS

LIST OF TABLES

LIST OF FIGURES

Page

LIST OF SYMBOLS

λ	wavelength of the incident radiation
d	distance between parallel crystal planes
θ	angle of incidence
n	integer value
P	pressure
P_o	vapor pressure
p_i	partial pressure of component i
E_n	energy of desorption
v	volume of gas adsorbed
v_m	monolayer volume
c	BET constant
R_g	ideal gas constant
T	absolute temperature
A	slope of BET plot
I	intercept of BET plot
N_{av}	Avogadro's number
a	coverage area of a single molecule
m	sample mass
V	liquid molar volume of the adsorbate
q_{sat}	saturation capacity

b	adsorption affinity
b_o	adsorption affinity at reference temperature T_o
b_∞	adsorption affinity at infinite temperature
T_o	reference temperature
t	adsorption interaction heterogeneity parameter
Q	enthalpy of adsorption
V_{gas}	gas molar volume
V_{liq}	liquid molar volume
q_{st}	isosteric
y_n	gas phase fraction of component n
x_n	adsorbed phase fraction of component n
$f_n(t)$	isotherm equation for integration
P^o	hypothetical vapor pressure at mixture loading
n_i	number of moles of component i adsorbed
$S_{1,2}$	adsorption selectivity for component 1 over component 2
θ_i	fractional loading
H_i	Henry's constant
RH	relative humidity
C	measured concentration
C_o	concentration at feed conditions
mol	mole
$sccm$	standard cubic centimeters per minute
u	interstitial velocity

D_{eff}	effective diffusivity
U_{total}	overall heat transfer coefficient
ε	voidage
$2*R_p$	particle radius
k_D	linear driving force coefficient
Cp_{gas}	molar heat capacity, gas
Cp_{solid}	specific heat capacity, solid
L	bed length
V_o	superficial velocity
ρ_b	bed density

LIST OF ABBREVIATIONS

BET	Brunnauer-Emmett-Teller
cc	cubic centimeter
CSD	Cambridge Structural Database
CUS	Coordinatively Unsaturated Site
DMF	N,N-dimethylformamide
erf	error function
exp	exponential function
IAST	Ideal Adsorbed Solution Theory
IGA	Intelligent Gravimetric Analyzer
MEA	Monoethanolamine
MFC	Mass Flow Controller
MIL	Materials d'Institute Lavoisier
MOF	Metal-Organic Framework
MS	Mass Spectrometer
NO_x	Nitrogen Oxides
OMS	Open-Metal Site
PAF	Porous Aromatic Framework
PCP	Porous Coordination Polymer
PCN	Porous Coordination Network
PID	Proportional-Integral-Derivative

PSA	Pressure Swing Adsorption
psi	pounds per square inch
psia	pounds per square inch absolute
PSM	Post-Synthetic Modification
PTFE	Polytetrafluoroethylene
PXRD	Powder X-Ray Diffraction
RPSA	Rapid Pressure Swing Adsorption
R^2	R-Squared fitting value
SBU	Secondary Building Unit
SIFSIX	SiF^{-6} based materials
SO_x	Sulfur Oxides
SS	Stainless Steel
316SS	Grade 316 Stainless Steel
std dev	Standard Deviation
TGA	Thermogravimetric Analysis
TSA	Temperature Swing Adsorption
UHP	Ultrahigh Purity
VSA	Vacuum Swing Adsorption
VPSA	Vacuum-Pressure Swing Adsorption
XRD	X-Ray Diffraction
ZIF	Zeolitic-Imidazolate Framework

SUMMARY

The theme of this work is the observation and understanding of the effects of pore functionalization on adsorption properties of stable Metal-Organic Frameworks (MOFs). Over the first two sections of this work, sets of materials with representative pore sizes and functional groups are studied for adsorption properties. Observed trends are used to identify the best pore properties achievable via functionalization for adsorption systems. The third section of this work provides perspective on MOF materials and proposes target pore features for an efficient adsorbent for carbon dioxide capture from flue gas.

The highly stable UiO-66 series of materials was selected for a pure-component adsorption study. The selectivity and capacity for CO_2 can be best enhanced with the smallest, most polar functional group, such as an amino group, but significantly enhance water adsorption. Large, non-polar groups do not yield a hydrophobic material, but may be useful for humid gas separations as pore filling with water is inhibited.

A breakthrough study was conducted using CO_2:CH_4 and CO_2:N_2 mixtures on a set of stable MOFs. UiO-66-NH_2 and UiO-66-DM, where DM=dimethyl, outperform predictions based on published isotherms. UiO-66-DM may be a good candidate for further study due to the combination of partial hydrophobicity and good selectivity.

Several pore features are proposed for a MOF as a humid gas separation medium. The designable nature of MOFs allows for size-matched pores and single-molecule traps which can selectively or cooperatively adsorb CO_2 in the presence of water. Also, these materials would be well suited for advanced pressure swing adsorption systems.

CHAPTER 1

INTRODUCTION

1.1 Metal-Organic Frameworks: A Unique Class of Porous Materials

Porous materials are highly desirable for many applications.[1] Metal-Organic Frameworks (MOFs) are a young class of porous materials.[2, 3] Among the many uses under active research for MOFs are: adsorption,[4-8] catalysis,[9, 10] drug delivery,[11] chemical sensing,[12] non-linear optics,[13] thin films,[14] ferroelectrics,[15] and luminescence.[16] In addition to all these uses, the properties of MOFs enables detailed characterization and thus detailed simulation and prediction of new properties and new uses.[17]

The origin of the term "metal-organic framework" is attributed to Omar Yaghi, a pioneer in MOF development.[18, 19] As the field of materials with similar properties and synthetic techniques has grown, various equivalent general names have been proposed, such as Porous Coordination Polymers (PCPs) and Networks (PCNs).[20-22] Despite the various naming schemes, both for the entire class of materials and especially for individual materials, the field has grown at an enormous rate within the past two decades.[23] For the remainder of this work, all inorganic-organic hybrid porous materials of a modular, crystalline nature will be referred to as MOFs.

1.1.1 *Development of MOFs*

MOFs are a chemically diverse class of materials, synthesized from the connection of organic linkers and metal secondary-building units (SBUs). The field of MOF research continues to grow and yield interesting and novel materials primarily due to the extraordinarily large number of choices of both organic linkers and inorganic

SBUs.[24] Primarily, synthesis occurs by dissolving an organic linker and a metal salt in a solvent, such as DMF, and subsequent heating in a sealed vessel, and numerous methods for directing the synthesis have been developed.[25] The resulting material retains unreacted materials and solvent, requiring washing and activation before the pores can be utilized.[26] The organic linkers are any number of multi-dentate ligands, including polycarboxylates[27] and azolates.[28] The SBUs form *in situ* in nearly all cases for MOF synthesis allowing for one-pot synthesis.

One of the first techniques for obtaining various properties in MOFs was termed isoreticular synthesis. The term isoreticular is defined as "having the same network topology."[19] While maintaining linker and SBU connectivity, varying the organic linker yields a series of isoreticular materials, an example series is shown in Figure 1.1. One of the consequences of this control is the ability to "tune" the properties of the material in an incremental fashion. For instance, addition of an amino group to the benzene ring of terephthalate yields a material with significantly improved adsorption affinity in comparison to the unfunctionalized material.[29] Further extension of this technique leads to multifunctional materials[22, 30] and unique properties.[31]

Under certain circumstances, changing the organic linker leads to an entirely new material.[32] This change lead to one of the most important series of isoreticular materials, MOF-74.[33] Instead of replacing the organic linker, the metal introduced in synthesis can be varied from Zn to Mg, Ni, Co, Fe, or Mn, yielding a series of isostructural materials with varying properties.[34-36] The resulting series, known by the names of (M)MOF-74, (M)CPO-27, and M/DOBDC, where M is the metal symbol, has yielded record-breaking adsorption properties and high selectivities.[36, 37] A property found in this series of

materials is the coordinatively-unsaturated site (CUS) or open-metal site (OMS), which is essentially an adsorbate-accessible metal cation, a highly active site for adsorption[36] and catalysis.[10] OMSs were first observed in HKUST-1, a copper-paddlewheel SBU, and this material remains one of the most investigated materials for adsorption study.[38]

A series of important and highly stable MOFs are isoreticular to MIL-53 (Materials of Institute Lavoisier).[39] These materials show significant flexibility and transition from narrow 8.5Å pores to wide 13Å pores. This flexibility, or "softness," enables many separations that are difficult with rigid materials.[8] Most MOFs show some degree of flexibility, ranging from rotation and bending of organic linkers up to large unit cell size changes. Flexibility has an impact on virtually all adsorption properties, particularly diffusion rates, heats of adsorption, and selectivity.

Multi-step synthetic methods have been developed which utilize OMS and organic functionalities within the pore spaces to produce new functional materials. After the material is synthesized and washed, post-synthetic modifications (PSM) can be conducted on the chemically active functional groups exposed in the pore space.[40, 41] Major PSM methods include amine grafting on OMS,[42, 43] condensation reactions on amine groups,[44] ligand exchange,[45, 46] and metal substitution.[47, 48] These techniques are able to introduce functionalities within the pore space which are not obtainable via direct synthetic technique due to various incompatibilities.

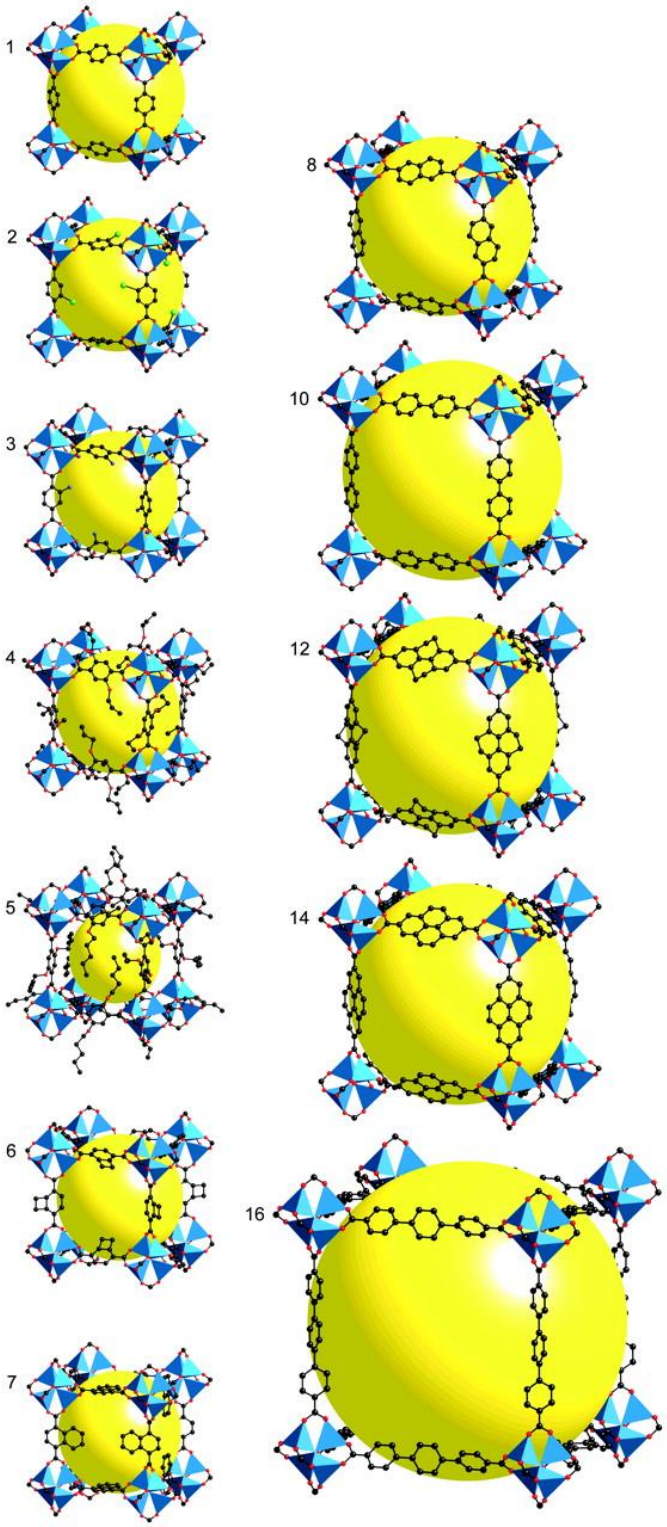

Figure 1.1. Examples of the IRMOF series of materials exemplifying the ability to control pore size and functionality via control of the organic linker. Reproduced from Eddaoudi, et al.[19]

1.2 Synthesis of MOFs

MOFs synthesis is a bottom-up approach, which is the process of making a complex product from basic building-blocks. The general approach to MOF synthesis is to combine a metal ion source and an organic ligand in a solvent, then heat the solution in a sealed vessel for some period of time in a temperature controlled oven.[25, 49] This method is known as solvothermal synthesis or conventional synthesis. If water is the solvent, then the method is known as hydrothermal synthesis. Nearly all MOFs require a unique set of conditions, especially when identical reaction solutions can yield multiple products or polymorphs with a variation in time or temperature.[50]

The metal ion source is typically a salt with nitrate as the counterion. Altering the anion in the metal source can lead to significantly different MOF structures.[51] Modulators can also be added to affect particle growth or alter the MOF structure. Typically, modulators are weak acids which can coordinate with the metal ions in solution, stabilizing or inhibiting transient structures, thus allowing a degree of control over nucleation and growth.[52]

The synthesis temperature can range from 323K-523K, where a particular temperature may be optimal for producing a particular MOF. Choice of synthesis temperature is typically determined by trial-and-error, as there are many unknown factors influencing the synthesis mechanism. Among the limiting factors are solvent and ligand stability at high temperatures as well as pressure limitations of vessels.

The typical vessels used for synthesis are either PTFE-lined stainless steel autoclaves or borosilicate glass vials ranging from 20 to 60 mL. Autoclaves are used

when autogenous pressures may exceed the rating for glass vials. Most syntheses can be conducted in glass vials, which is preferred as they are low cost and single use.

Alternative synthesis methods include electrolysis, microwave, mechanical, and solvent-free methods. These methods often require optimization for each individual material but have potential for more rapid synthesis with more uniform product quality but require specialized reaction vessels and optimization of synthesis conditions.

1.3 Stability

One of the most serious problems encountered during MOF development is the issue of stability of the materials in contact with water vapor.[53] Many of the first MOF materials would decompose quickly on exposure to air leading to degradation of porosity, function, and crystallinity.[54] The concept of stability has become a major factor of consideration for new material reports in recent years. Stability is also a major driving force for further study of a material and its potential commercialization.[55] The criteria for stability vary significantly from report to report and the resulting ability to classify materials on a scale of stability remains a subjective process.

Numerous papers have been published on the subject of stability, attributing the propensity to degrade on a number of factors. As with all chemical systems, reactivity can either originate from thermodynamic or kinetic factors. Thermodynamic factors can essentially be simplified to the difference between the bond energies of products and reactants.[53] This has been utilized to predict most carboxylate-based MOFs to be unstable, as hydrolysis will be energetically favorable.

The complexity behind predicting kinetic stability poses a significant challenge. Attribution of the degree of stability to certain factors has been a case-by-case operation, highly dependent on human intuition and experimental design. Several recent works have begun to systematically study the factors and have identified several mechanisms to inhibit MOF degradation.[56-59] Among these inhibition factors are steric hindrance, ligand exchange rates, and high connectivity.

The first factor has been studied by Jasuja, et al. and has shown that the highly susceptible zinc-carboxylate bonds can be protected from attack by water with a bulky, methylated ligand.[56] The next factor prediction and understanding of the chemical stability of MOFs lies in their alternate name, Porous Coordination Polymer. The field of coordination chemistry provides a useful series of trends for prediction of MOF stability.[57] Ligand exchange rate is a property of each metal and varies with oxidation state.[58] Among the commonly used ions, Cr^{+3} and Al^{+3} have slow exchange rates and are also found to yield stable MOFs. Finally, high connectivity helps prevent structure loss because, when a single ligand-metal bond is broken, a cascading structural collapse doesn't occur, a property exemplified by UiO-66.[59]

1.4 Adsorption

As with other porous materials, the applications for MOFs are diverse. One of the applications is adsorption where the adsorbent provides an energy efficient medium for separation. Of particular interest is bulk separation of carbon dioxide from flue gas and bulk separation of CO_2 or N_2 from CH_4 in natural gas. Additionally, trace contaminant

removal is of major importance for various industrial applications such as pipeline transport of natural gas.

Adsorption is the process by which molecules, known as adsorbates, are concentrated near a solid surface in excess of the bulk concentration. This reversible process is energetically favorable and the released energy is dissipated as heat. As with other exothermic processes, higher temperatures lead to lower adsorption performance. Also, mass transfer rates are important as the process of adsorption is a transfer of material from a bulk gas phase to an adsorbed phase within a solid porous particle.

Different adsorbents and adsorbates interact to different degrees and are generally classified into two general regimes, chemical and physical. For chemical adsorbents (chemisorbents), the dominant adsorption mechanism is reversible chemical reactions between adsorbates and surface functionalities. For physical adsorbents (physisorbents), electrostatic interactions between adsorbates and the pore surface result in attractive forces between the adsorbate and adsorbent. Adsorption affinities differ for each adsorbate species which leads to selective adsorption and inevitably to the ability to separate a mixture. Selection of various pore functionalities can enhance or inhibit certain adsorption interactions.

1.4.1 *Effect of Functional Groups*

The effect of functional groups on the adsorption properties of various porous materials is an extensively studied topic but new works continue to produce unexpected results.[30] The effect of each functional group is highly dependent on the porous material as well as the mechanism of adsorption. For chemisorption, the chemical reactivity between the functional group and the target adsorbate are essential for improved

adsorbent performance. Although other factors come into play when a material is to be utilized in a real-world system, they won't be discussed here for chemisorbents. For physisorption, the primary effect of functional groups is alteration of electrostatic and dispersive forces exerted between the adsorbate and pore walls.

Physisorption involves the sum of attractive forces exerted between adsorbates and solid surfaces. One way of understanding this is to imagine a potential energy well near the solid surface into which the adsorbate molecule enters and reduces the overall energy of the system. In order to increase these attractive forces, two major approaches can be used. The first is to place multiple surfaces in close proximity in order for a single adsorbate molecule to adsorb at a site with multiple overlapping potentials. The second is to increase the intensity of the potential energy well at the adsorption site by increasing either the intensity of electrostatic interactions or geometrically matching the partial charges of the adsorbate with the functionality.

Nanoporous material research has greatly improved the ability to obtain various pore sizes and shapes, which directly relates to the ability to maximizing overlapping potentials. MOF research allows some degree of control over pore size and shape due to the predictability of isoreticular structures. When two MOFs are synthesized with identical SBUs, adjustment of the organic linker can lead to predictable pore size changes in many cases. Also, with elongated linkers, some MOFs can form interpenetrated structures, where two complete networks are intermeshed. These interpenetrated materials can possess smaller pores than an isoreticular structure with shortened linkers, thus enabling an alternative route to achieving pore size control.

The diverse nature of organic chemistry allows for a vast number of accessible organic functionalities. The two most common linkers used in MOFs, terephthalate and imidazolate, are highly amenable to functionalization. Addition of functional groups with strong partial charges have been shown to improve adsorption in all classes of adsorbent materials. Commonly targeted groups are hydroxyl, amino, nitro, and carboxyl functionalities, all of which have been tested in certain MOF families for their effects on adsorption. The correlation between increased adsorbed amounts and the properties of these functional groups is not linear, but a general ranking of their performance shows that the smallest and most polar functional groups often show the best performance on a per mass of adsorbent basis.

1.4.2 *Mixture Adsorption*

Previous sections only discuss pure-component adsorption, but most adsorbents are used to separate mixtures. For equilibrium adsorption, two additional factors arise. The first is competition between gas molecules for adsorption sites. The second is adsorbate-adsorbate interactions. At low pressures and low loadings, the competition is close to thermodynamically ideal, but deviate significantly as loadings and pressures increase. Some systems, particularly those with water vapor adsorption, are highly non-ideal at all loadings. Mixture isotherms for nearly ideal systems are computationally easy to predict from pure-component isotherms, but more non-ideal systems require experimental measurement to verify any predictions.

For dynamic mixture adsorption, the impact of diffusion becomes highly relevant. In some cases, when two molecules have similar adsorption properties, the difference in diffusion rates can be significant enough to allow kinetic separations. This is especially

important for molecular sieves where pore sizes are almost equivalent to the kinetic diameter of adsorbates.[60] As pore features and adsorption properties vary greatly between each adsorbent-adsorbate pair, general rules are difficult to extrapolate. Among the features which each have unique interactions are one dimensional channels, chamber-window systems, interconnected channels, and three dimensional structures.

Measuring mixture adsorption requires a combined adsorption apparatus and gas analyzer. Measuring equilibrium mixture adsorption is typically accomplished with a volumetric system while dynamic measurements can be done with a breakthrough system. Equilibrium measurements use a combination of composition analysis and mixture equations of state to determine uptake. Breakthrough instruments pass a mixture through a small adsorbent bed and measure outlet composition as a function of time. Volumetric methods are highly accurate even with small sample sizes, but may not be able to produce kinetic data, whereas breakthrough experiments can yield nearly all relevant data if the system is sufficiently well designed and the sample is large.

1.4.2.1 Breakthrough Analysis

The simplest dynamic adsorption experiment is known as breakthrough, a name derived from the characteristic series of events of adsorption, saturation, and eventual "breaking through" of feed components. Measurement of the concentration of components downstream of the bed over time yields the breakthrough curve. Initially, the bed is purged of adsorbed species by a weakly adsorbing gas such as helium. As the feed stream of known composition is passed through the bed, the mixture components will adsorb and eventually saturate the bed in a progressive manner. As the bed nears saturation, a fraction of the feed gas mixture will break through the bed and be detected,

with the fraction rising to match the inlet concentration at complete bed saturation. The time for this breakthrough to occur and the shape of the resulting breakthrough curve are intrinsically tied to the experiment.

The factors which affect breakthrough include mass transfer rates, heat effects, and mixture adsorption effects.[61] Each of these reduces the effectiveness of the bed and thus allows feed gas to breakthrough in a shorter period of time.

1.4.3 *Adsorption Cycles*

Since adsorption is a function of both the system pressure and temperature, the two major adsorption cycles control these properties in order to adsorb and release various mixture components in a predictable manner. Pressure swing adsorption (PSA) is generally a process where separation is achieved by adsorbing gas at an elevated pressure then driving desorption by reducing the system pressure. Temperature swing adsorption (TSA) is generally a process where a component is strongly adsorbed at constant pressure and desorption is driven by elevating the bed temperature. Typically the gas mixture is divided into two portions based on how the adsorbent bed retains each component. The more strongly adsorbed materials are retained while a purified product stream of weakly adsorbing material passes through the bed. Regeneration of the bed involves desorption of the strongly adsorbed species and removal from the bed, allowing for the process to be repeated.

PSA processes are generally used for bulk gas separations and can be optimized to produce either fraction of the mixture at high purity at the expense of the purity of the other fraction. The most well-known PSA cycle is the Skarstrom cycle,[62, 63] where two adsorbent beds are used in conjunction to create a continuous separation process. In this

cycle, one bed is adsorbing at high pressure and producing the raffinate while the other bed is being regenerated at low pressure and producing the extract. In between these stages are pressurization and blowdown phases of the cycle, where the bed pressure is rapidly changed. This cycle, as originally designed for air separation, produces a high purity raffinate stream while the extract is released as waste. Various optimizations and increased cycle complexity can yield higher purity and/or recovery of either extract or raffinate.

Two major factors come into play outside of the adsorbent performance with regard to PSA cycles. The first is temperature control, as most PSA processes operate nearly adiabatically. Heat transfer rates are slow while the heat of adsorption can be significant and lead to temperature rises of many tens of degrees Centigrade. Dissipation of this heat is essential to improving the utilization of the bed, and remains an engineering hurdle for implementation. The second is mechanical stability, as large pressure changes can generate large forces in the bed. If adsorbent particles are crushed to dust, the material can elutriate downstream or have significantly reduced performance. Both of these factors are important for PSA systems design, in addition to the properties of the material.

TSA processes are well suited to removal of strongly adsorbing species at dilute conditions and constant pressure. The general process involves strongly adsorbing one component while producing a high purity raffinate, then regenerating the bed by adding heat, usually in the form of steam or hot gas. If properly designed, the extract can also be obtained in high purity, but is usually considered waste as it is mixed with the heat transfer fluid.

1.4.4 *Mass Transfer Effects*

The general method for characterizing adsorbent materials is to determine the properties when the material is at thermal and chemical equilibrium with its surrounding environment. Naturally, in real-world applications, the ability to wait until everything has reached equilibrium is not economically viable. The importance of mass transfer cannot be understated when attempting to transition materials from development to implementation phases. Typically, these measurements and calculations are only conducted on the best candidate materials, due to the difficulty in controlling extraneous effects. These effects include particle size, particle texture, and the instrument characteristics.

A focus only on the micropore diffusion or only on the bulk and macropore diffusion allows for a simplified understanding. Generally, micropore diffusion will not be the dominant factor in adsorption systems unless the pores are very narrow or molecules adsorb strongly in the pores. These factors are often found in molecular sieves or small pore materials with CUS or exposed cations. Most MOFs studied to date have fast diffusion rates due to the significant flexibility of the coordination and covalent bonds found throughout the material, even if the structure is rigid.[64, 65]

The adsorbent material must be in a form which can be handled in bulk industrial processes, typically a mechanically robust pellet. The pellet form compresses individual adsorbent crystals together along with a binder, a process which forms macropores and other unpredictable textural properties. These properties have an impact on mass transfer rates which must be empirically determined for a pelletization process. Binder typically accounts for 10-30% of the pellet mass and thus reduces the total performance.

Pelletization of MOFs has recently become a subject of increased study as it has been shown that MOFs produce robust pellets without any or very little binder.[66-68]

1.5 Critical Research Needs

Each of the concepts and techniques introduced previously are important to the understanding of adsorbents and for further development of materials for separations. As MOFs are a young and rapidly growing class of materials, the understanding of the new properties accessible via MOFs an essential endeavor. Three major factors must be considered in order to advance the understanding of MOFs as adsorbents.

The first factor is studying inherently stable MOFs for their pure-component adsorption properties. Modifying MOFs in a systematic manner in an attempt to cover a representative set of pore features would allow for a better understanding of how to modify other MOFs for improved performance. By measuring the gas uptake at equilibrium conditions and at various temperatures, heats of adsorption and ideal selectivity can be calculated as well as predictions of mixture adsorption behavior. Together, all of these properties are important for design and implementation of these materials at a larger scale.

The second factor is measuring the dynamic adsorption behavior of another set of MOFs with representative pore features in order to understand their effect on non-equilibrium adsorption. Mixture adsorption measurements obtained via breakthrough experiments enable a direct observation of the effects of adsorbing multiple gases simultaneously. The breakthrough times provide information about how much gas can be adsorbed before the bed is no longer effective for separations and therefore must be

regenerated. The data can be further used to build a model to verify the results and determine factors not obtainable by the direct measurements.

The third factor is creating a connection between the reports of MOF stability, gas adsorption, and water adsorption properties to propose structures and methods for producing an effective water-tolerant CO_2 adsorbent. Previously published research has identified certain mechanisms and others have been proposed which govern the water-induced degradation of MOFs. Further, producing a stable MOF that adsorbs enough CO_2 in the presence of water vapor for useful applications requires a focus on different pore features. Currently, the focus is on single functionalities that strongly interact with CO_2 but water always adsorbs more strongly. Therefore a focus on multiple CO_2-specific interactions at adsorption sites and shape matched pores may be the way to proceed.

1.6 Overview of This Dissertation

The following work describes the development of trends for design of optimal MOFs in adsorption applications. Chapter 3 is taken directly from a peer-reviewed article published in *Langmuir*.[69] This work discusses the measurement of pure-component gas adsorption data on a series of isostructural MOFs varied by the presence of a functional group on the organic linker. The MOF series chosen was based on the highly stable UiO-66 materials and the functional groups were chosen to represent for polar, hydrophobic, and hydrogen-bonding capability. From the results, trends are discerned which indicate that the smallest, most polar functional group leads to the highest CO_2 selectivity. Also, UiO-66 shows multiple adsorption sites due to the metal cluster.

In Chapter 4, the dynamic adsorption capacity and separation capability of a series of MOFs is explored with breakthrough experiments and modeling. Due to small batch sizes during normal MOF synthesis, a micro-bed breakthrough apparatus was utilized to test the materials. Due to the construction of the apparatus, the typical assumptions applied to breakthrough measurements are not valid, leading to a model of high complexity. The results of this work indicate that the best selected MOF, UiO-66-NH_2, performs about half as well as zeolite NaY, chosen as a standard. The results further indicate that the multiple sources of uncertainty in this experimental setup prevent its further use in obtaining exact quantitative measurements, but retains suitable qualitative and model validation capabilities.

In Chapter 5, the extensive library of knowledge of MOFs in general is explored in order to gain perspective on the attributes which can be used to develop a water-tolerant adsorbent for flue gas capture. By removing situations which are more properly suited for other classes of adsorbents, the best candidate system for carbon capture from flue gas is vacuum swing adsorption. The features of MOFs which impart stability, provide for selectivity of CO_2 over other gases, and do not induce strong water adsorption are reviewed. Utilizing these pieces of information, a series of target structures are proposed which may possess suitable properties for carbon dioxide capture.

In Chapter 6, the conclusions to this work are presented and recommendations for future work are discussed.

1.7 References

1. Furukawa, H., et al., *The chemistry and applications of metal-organic frameworks.* Science (New York, N.Y.), 2013. **341**: p. 1230444.

2. Zhou, H.-C., J.R. Long, and O.M. Yaghi, *Introduction to metal-organic frameworks.* Chemical reviews, 2012. **112**: p. 673-4.

3. Rowsell, J.L.C. and O.M. Yaghi, *Metal–organic frameworks: a new class of porous materials.* Microporous and Mesoporous Materials, 2004. **73**: p. 3-14.

4. Sumida, K., et al., *Carbon dioxide capture in metal-organic frameworks.* Chemical reviews, 2012. **112**: p. 724-81.

5. Suh, M.P., et al., *Hydrogen storage in metal-organic frameworks.* Chemical reviews, 2012. **112**: p. 782-835.

6. Wu, H., et al., *Commensurate adsorption of hydrocarbons and alcohols in microporous metal organic frameworks.* Chemical reviews, 2012. **112**: p. 836-68.

7. Li, J.-R., J. Sculley, and H.-C. Zhou, *Metal-organic frameworks for separations.* Chemical reviews, 2012. **112**: p. 869-932.

8. Horike, S., S. Shimomura, and S. Kitagawa, *Soft porous crystals.* Nat Chem, 2009. **1**(9): p. 695-704.

9. Corma, a., H. García, and F.X. Llabrés i Xamena, *Engineering metal organic frameworks for heterogeneous catalysis.* Chemical reviews, 2010. **110**: p. 4606-55.

10. Lee, J., et al., *Metal-organic framework materials as catalysts.* Chemical Society reviews, 2009. **38**: p. 1450-9.

11. Horcajada, P., et al., *Metal-organic frameworks in biomedicine.* Chemical reviews, 2012. **112**: p. 1232-68.

12. Kreno, L.E., et al., *Metal-organic framework materials as chemical sensors.* Chemical reviews, 2012. **112**: p. 1105-25.

13. Wang, C., T. Zhang, and W. Lin, *Rational synthesis of noncentrosymmetric metal-organic frameworks for second-order nonlinear optics.* Chemical reviews, 2012. **112**: p. 1084-104.

14. Bétard, A. and R.A. Fischer, *Metal-organic framework thin films: from fundamentals to applications.* Chemical reviews, 2012. **112**: p. 1055-83.

15. Zhang, W. and R.-G. Xiong, *Ferroelectric metal-organic frameworks.* Chemical reviews, 2012. **112**: p. 1163-95.

16. Cui, Y., et al., *Luminescent functional metal-organic frameworks.* Chemical reviews, 2012. **112**: p. 1126-62.

17. Getman, R.B., et al., *Review and analysis of molecular simulations of methane, hydrogen, and acetylene storage in metal-organic frameworks.* Chemical reviews, 2012. **112**: p. 703-23.

18. Li, H., et al., *Design and synthesis of an exceptionally stable and highly porous metal-organic framework.* Nature, 1999. **402**(6759): p. 276-279.

19. Eddaoudi, M., et al., *Systematic design of pore size and functionality in isoreticular MOFs and their application in methane storage.* Science (New York, N.Y.), 2002. **295**: p. 469-72.

20. Kitagawa, S., R. Kitaura, and S.-i. Noro, *Functional porous coordination polymers.* Angewandte Chemie (International ed. in English), 2004. **43**: p. 2334-75.

21. Kitagawa, S. and R. Matsuda, *Chemistry of coordination space of porous coordination polymers.* Coordination Chemistry Reviews, 2007. **251**(21-24): p. 2490-2509.

22. Zhao, D., et al., *Tuning the topology and functionality of metal-organic frameworks by ligand design.* Accounts of chemical research, 2011. **44**: p. 123-33.

23. Keskin, S., T.M. van Heest, and D.S. Sholl, *Can metal-organic framework materials play a useful role in large-scale carbon dioxide separations?* ChemSusChem, 2010. **3**: p. 879-91.

24. O'Keeffe, M. and O.M. Yaghi, *Deconstructing the crystal structures of metal-organic frameworks and related materials into their underlying nets.* Chemical reviews, 2012. **112**: p. 675-702.

25. Stock, N. and S. Biswas, *Synthesis of metal-organic frameworks (MOFs): routes to various MOF topologies, morphologies, and composites.* Chemical reviews, 2012. **112**: p. 933-69.

26. Farha, O.K. and J.T. Hupp, *Rational design, synthesis, purification, and activation of metal-organic framework materials.* Accounts of chemical research, 2010. **43**: p. 1166-75.

27. Paz, F.a.A., et al., *Ligand design for functional metal-organic frameworks.* Chemical Society reviews, 2012. **41**: p. 1088-110.

28. Zhang, J.-P., et al., *Metal azolate frameworks: from crystal engineering to functional materials.* Chemical reviews, 2012. **112**: p. 1001-33.

29. Rowsell, J.L.C. and O.M. Yaghi, *Effects of functionalization, catenation, and variation of the metal oxide and organic linking units on the low-pressure hydrogen adsorption properties of metal-organic frameworks.* Journal of the American Chemical Society, 2006. **128**: p. 1304-15.

30. Deng, H., et al., *Multiple functional groups of varying ratios in metal-organic frameworks.* Science (New York, N.Y.), 2010. **327**: p. 846-50.

31. Chen, B., S. Xiang, and G. Qian, *Metal-organic frameworks with functional pores for recognition of small molecules.* Accounts of chemical research, 2010. **43**: p. 1115-24.

32. Millward, A.R. and O.M. Yaghi, *Metal-organic frameworks with exceptionally high capacity for storage of carbon dioxide at room temperature.* Journal of the American Chemical Society, 2005. **127**: p. 17998-9.

33. Rosi, N.L., et al., *Rod packings and metal-organic frameworks constructed from rod-shaped secondary building units.* Journal of the American Chemical Society, 2005. **127**: p. 1504-18.

34. Grant Glover, T., et al., *MOF-74 building unit has a direct impact on toxic gas adsorption.* Chemical Engineering Science, 2011. **66**: p. 163-170.

35. Zhang, Q., B. Li, and L. Chen, *First-Principles Study of Microporous Magnets M-MOF-74 (M = Ni, Co, Fe, Mn): the Role of Metal Centers.* Inorganic chemistry, 2013. **52**: p. 9356-62.

36. Caskey, S.R., A.G. Wong-Foy, and A.J. Matzger, *Dramatic tuning of carbon dioxide uptake via metal substitution in a coordination polymer with cylindrical pores.* Journal of the American Chemical Society, 2008. **130**: p. 10870-1.

37. Remy, T., et al., *Selective Dynamic CO 2 Separations on Mg-MOF-74 at Low Pressures: A Detailed Comparison with 13X.* The Journal of Physical Chemistry C, 2013. **117**: p. 9301-9310.

38. Chui, S.S., *A Chemically Functionalizable Nanoporous Material [Cu3(TMA)2(H2O)3]n.* Science, 1999. **283**: p. 1148-1150.

39. Serre, C., et al., *Very large breathing effect in the first nanoporous chromium(III)-based solids: MIL-53 or Cr-III(OH)center dot{O2C-C6H4-CO2}center dot{HO2C-C6H4-CO2H}(x)center dot H2Oy.* Journal of the American Chemical Society, 2002. **124**(45): p. 13519-13526.

40. Cohen, S.M., *Postsynthetic methods for the functionalization of metal-organic frameworks.* Chemical reviews, 2012. **112**: p. 970-1000.

41. Cohen, S.M., *Modifying MOFs: new chemistry, new materials.* Chemical Science, 2010. **1**: p. 32.

42. Hwang, Y.K., et al., *Amine grafting on coordinatively unsaturated metal centers of MOFs: consequences for catalysis and metal encapsulation.* Angewandte Chemie (International ed. in English), 2008. **47**: p. 4144-8.

43. Choi, S., et al., *Modification of the Mg/DOBDC MOF with Amines to Enhance CO 2 Adsorption from Ultradilute Gases.* The Journal of Physical Chemistry Letters, 2012. **3**: p. 1136-1141.

44. Wang, Z. and S.M. Cohen, *Postsynthetic covalent modification of a neutral metal-organic framework.* Journal of the American Chemical Society, 2007. **129**: p. 12368-9.

45. Karagiaridi, O., et al., *Opening ZIF-8: a catalytically active zeolitic imidazolate framework of sodalite topology with unsubstituted linkers.* Journal of the American Chemical Society, 2012. **134**: p. 18790-6.

46. Kim, M., et al., *Postsynthetic ligand exchange as a route to functionalization of 'inert' metal–organic frameworks.* Chemical Science, 2012. **3**: p. 126.

47. Kim, M., et al., *Postsynthetic ligand and cation exchange in robust metal-organic frameworks.* Journal of the American Chemical Society, 2012. **134**: p. 18082-8.

48. Lau, C.H., R. Babarao, and M.R. Hill, *A route to drastic increase of CO2 uptake in Zr metal organic framework UiO-66.* Chemical communications (Cambridge, England), 2013. **49**: p. 3634-6.

49. Lee, Y.-R., J. Kim, and W.-S. Ahn, *Synthesis of metal-organic frameworks: A mini review.* Korean Journal of Chemical Engineering, 2013. **30**: p. 1667-1680.

50. Haouas, M., et al., *In Situ NMR, Ex Situ XRD and SEM Study of the Hydrothermal Crystallization of Nanoporous Aluminum Trimesates MIL-96, MIL-100, and MIL-110.* Chemistry of Materials, 2012. **24**: p. 2462-2471.

51. Gaab, M., et al., *The progression of Al-based metal-organic frameworks – From academic research to industrial production and applications.* Microporous and Mesoporous Materials, 2012. **157**: p. 131-136.

52. Schaate, A., et al., *Modulated synthesis of Zr-based metal-organic frameworks: from nano to single crystals.* Chemistry (Weinheim an der Bergstrasse, Germany), 2011. **17**: p. 6643-51.

53. Low, J.J., et al., *Virtual high throughput screening confirmed experimentally: porous coordination polymer hydration.* Journal of the American Chemical Society, 2009. **131**: p. 15834-42.

54. Kaye, S.S., et al., *Impact of preparation and handling on the hydrogen storage properties of Zn4O(1,4-benzenedicarboxylate)3 (MOF-5).* Journal of the American Chemical Society, 2007. **129**: p. 14176-7.

55. Czaja, A.U., N. Trukhan, and U. Müller, *Industrial applications of metal-organic frameworks.* Chemical Society reviews, 2009. **38**: p. 1284-93.

56. Jasuja, H., et al., *Kinetic water stability of an isostructural family of zinc-based pillared metal-organic frameworks.* Langmuir : the ACS journal of surfaces and colloids, 2013. **29**: p. 633-42.

57. Cook, T.R., Y.-r.R. Zheng, and P.J. Stang, *Metal–Organic Frameworks and Self-Assembled Supramolecular Coordination Complexes: Comparing and Contrasting the Design, Synthesis, and Functionality of Metal–Organic Materials.* Chemical Reviews, 2012. **113**: p. 121102080005003.

58. Helm, L. and A.E. Merbach, *Water exchange on metal ions: experiments and simulations.* Coordination Chemistry Reviews, 1999. **187**: p. 151-181.

59. Wu, H., et al., *Unusual and highly tunable missing-linker defects in zirconium metal-organic framework UiO-66 and their important effects on gas adsorption.* Journal of the American Chemical Society, 2013. **135**: p. 10525-32.

60. Mehio, N., S. Dai, and D.E. Jiang, *Quantum mechanical basis for kinetic diameters of small gaseous molecules.* J Phys Chem A, 2014. **118**(6): p. 1150-4.

61. Ruthven, D.M., S. Farooq, and K.S. Knaebel, *Pressure Swing Adsorption*. Wiley: 1993.

62. Skarstrom, C.W. Oxygen concentration process. United States patent US3237377 A, 1966.

63. Yang, R.T., *Adsorbents: Fundamentals and Applications*. Wiley: 2003.

64. Atci, E. and S. Keskin, *Understanding the Potential of Zeolite Imidazolate Framework Membranes in Gas Separations Using Atomically Detailed Calculations.* The Journal of Physical Chemistry C, 2012. **116**(29): p. 15525-15537.

65. Haldoupis, E., et al., *Quantifying large effects of framework flexibility on diffusion in MOFs: CH4 and CO2 in ZIF-8.* Chemphyschem, 2012. **13**(15): p. 3449-52.

66. Onubogu, K.A., *Effect of Binder Amount and Calcination Temperature on the Physical and Mechanical Properties of Pressed Metal Organic Framework UiO-66.*, 2014, Georgia Institute of Technology.

67. Bazer-Bachi, D., et al., *Towards industrial use of metal-organic framework: Impact of shaping on the MOF properties.* Powder Technology, 2014. **255**: p. 52-59.

68. Peterson, G.W., et al., *Effects of pelletization pressure on the physical and chemical properties of the metal-organic frameworks Cu-3(BTC)(2) and UiO-66.* Microporous and Mesoporous Materials, 2013. **179**: p. 48-53.

69. Cmarik, G.E., et al., *Tuning the Adsorption Properties of UiO-66 via Ligand Functionalization.* Langmuir, 2012. **28**(44): p. 15606-15613.

CHAPTER 2

MATERIALS AND EXPERIMENTAL METHODS

2.1 Material Characterization Methods

2.1.1 *Powder X-Ray Diffraction*

A powerful tool for analyzing the crystal structure of a material for identification and quality purposes is Powder X-Ray Diffraction (PXRD), a variation of X-Ray Diffraction (XRD). The governing process behind XRD is that the atoms, organized in crystal planes, will absorb and re-emit incident radiation, effectively reflecting a fraction of the radiation. When a detector is placed at the correct angle, the reflected radiation from multiple, parallel crystal planes produces constructive interference as predicted by Bragg's Law[1] (Eq. 2.1). As there are numerous crystal planes in a single crystal, the constructive interference results in a set of characteristic peaks at specific angles for the three dimensional crystal structure.

$$n\lambda = 2d \sin\theta \tag{2.1}$$

where λ is the wavelength of the incident radiation, d is the distance between parallel crystal planes, θ is the angle of incidence, and n is an integer value.

PXRD assumes that a powder is a large number of identical and randomly oriented crystals, allowing for all possible crystal orientations to be measured along a single axis. The information obtained from a PXRD scan is a set of peaks above a low

background signal and, without significant analysis, allows for rapid qualitative evaluation of a sample. If the peaks are not significantly greater than the background, then the sample can be regarded as of poor quality. If peaks are missing or located at the wrong position, then the sample can be regarded as contaminated or improperly synthesized. Typical analysis involves comparison of the position of prominent peaks to a simulated pattern obtained from published crystal structure data.

The instrument used to obtain PXRD measurements is an X'Pert PRO X-Ray Diffractometer from PANalytical. The software used to analyze the PXRD data was HighScore® from PANalytical. Published crystal structures were obtained from the Cambridge Structural Database (CSD). The crystal structure files were visualized and simulated PXRD patterns obtained using Mercury.

2.1.2 *Thermogravimetric Analysis*

A thermogravimetric analyzer (TGA) is an instrument with a high temperature furnace and precise mass balance. TGA is a destructive analysis technique and the standard result is a plot of weight versus temperature. Sample prep involves placing roughly 10mg of sample in a crucible, which is placed on the weight balance in the furnace. A purge gas stream is passed over the sample and the system temperature is incrementally raised while weight measurements are recorded. Weight loss as a function of temperature reveals information about the temperature range at which adsorbed species can be removed as well as the temperature range for decomposition. This data is important for determining what activation conditions can be used as well as thermal stability. In this work, TGA is used for determining weight loss of activation, suitable activation temperature ranges, and as a quality test for comparison to published results.

The instrument used is a Netzsch STA 449 F1 Jupiter thermogravimetry analyzer with an attached QMS 403 C Aëolos® quadrupole mass spectrometer. The software used to record and analyze the TGA and MS data was Proteus® thermal analysis software.

2.1.3 *Adsorption*

2.1.3.1 BET Method

Perhaps the most well-known method for characterizing the pore space of a material is N_2 adsorption at 77K, colloquially known as BET analysis. Two important attributes of porous materials is surface area and pore volume. Nitrogen is a relatively inert molecule, easily obtained at high purity, and available as a cryogenic fluid which makes it an excellent candidate for probing those two material attributes. The normal boiling point of N_2 is 77K and measurement at sub-atmospheric pressures (relative pressure $(P/P_o) < 1$) allows probing of the vapor-liquid equilibrium on surfaces.

The BET method, developed by Brunauer, Emmett, and Teller, is a mathematical model for adsorption of gas molecules as multiple layers on a pore surface[2] (Eqs. 2.2 and 2.3). The BET method has five major assumptions. First is that one molecule can adsorb on each distinct adsorption site, eventually forming a complete monolayer. Second is that an adsorbed molecule can act as an adsorption site for additional molecules as additional layers. Third is that the uppermost layer will approximate a liquid phase and will be in equilibrium with the vapor phase. Fourth is that a quantity of heat is required for the adsorption/desorption process, allowing for Arrhenius-type rate equations. The energy of desorption for each molecule in the layer at the solid surface is equivalent and denoted as E_1 while for all additional layers equals $E_2 = E_3 = \ldots = E_n = E_L$, the heat of

liquefaction. Fifth is that the number of layers approaches infinity as P/P_o approaches unity.

$$\frac{\left({}^{p}/_{p_o}\right)}{v\left(1-\left({}^{p}/_{p_o}\right)\right)} = \left(\frac{c-1}{v_m c}\right)\left({}^{p}/_{p_o}\right) + \frac{1}{v_m c} \tag{2.2}$$

$$c = exp\left(\frac{E_1 - E_L}{RT}\right) \tag{2.3}$$

where v is volume of gas adsorbed, v_m is monolayer volume, P/P_o is relative pressure, c is the BET constant, R is the ideal gas constant, and T is absolute temperature.

Plotting obtained data in the correct relative pressure regime yields a linear plot (Eq. 2.4). The standard relative pressure values are between $0.05 < P/P_o < 0.35$, but a lower range may be more appropriate for microporous materials. The factors for determining the relative pressures are discussed in further detail below.

$$\frac{\left({}^{p}/_{p_o}\right)}{v\left(1-\left({}^{p}/_{p_o}\right)\right)} \text{ vs. } \left({}^{p}/_{p_o}\right) \tag{2.4}$$

From this plot, the slope and intercept can be obtained and used to calculate the total surface area and surface area per unit mass of adsorbent (Eqs. 2.5-2.7).

$$\frac{1}{v_m} = A + I \tag{2.5}$$

$$c = 1 + \frac{A}{I} \tag{2.6}$$

$$S_{BET} = \frac{v_m * N_{av} * a}{m * V} \tag{2.7}$$

where A is equal to the slope and I is equal to the intercept of the plotted data, N_{av} is Avogadro's number, a is the coverage area of a single molecule, which for N_2 is 16 $Å^2$, m is sample mass, and V is liquid molar volume of the adsorbate.

One of the most important questions is the accuracy of the BET method for microporous and energetically heterogenous materials such as MOFs. These two aspects may weaken or invalidate assumptions four and five from the above list. The work by Walton et. al. shows that the BET method remains valid for MOFs and other microporous materials and calculations using data at a lower relative pressure range produce more meaningful surface area values[3]. Care must be taken to ensure physically reasonable values (non-negative) are calculated. The best pressure range varies from material to material, but an effective range for most microporous materials is $0.005 < P/P_o < 0.035$. This is the pressure range for BET calculations used throughout this work and is verified as physically reasonable.

A similar surface area calculation is based on the Langmuir model. Often, this method overestimates surface area as it contains assumptions which are invalid for microporous materials. The most important conflicting assumption is that the first

monolayer of adsorbate is formed to completion before any further layers form. Since additional adsorbed layers begin to form before the monolayer is complete, the measured adsorbed amount will be greater than what is actually adsorbed in the monolayer, leading to overestimated surface areas.

One aspect of surface area analysis is the required mass of adsorbent for accurate measurement. A rule-of-thumb is the required minimum mass yields at least one square meter of total surface area. This ensures that enough gas is adsorbed to minimize accuracy error from weighing and pressure measurement. This general rule was supported by the instrument manufacturer's recommendation for sample sizes in the provided operating manual.

The equipment used to measure N_2 adsorption at 77K is a Quadrasorb SI and the software used to analyze the data is QuadraWin from Quantachrome Instruments. Standards testing on the instrument verify accuracy and precision to be within ±5% of excepted values. Measurements are taken from 10^{-4} to 0.995 relative pressure with using UHP grade N_2 from Airgas. Activation of samples is conducted on a FloVac™ Degasser with an attainable vacuum of ~0.010 torr. Sample weight was obtained from the difference of an empty, sealed cell and the same cell loaded with activated sample sealed under N_2. Sample cells are glass tubes with one rounded end where the sample is placed while at the open end a CellSeal™ cap is inserted. The CellSeal™ cap acts as a check valve, preventing lab air intrusion to the sample during transfer and handling.

2.1.3.2 Pure-Component Adsorption

An introduction to adsorption was provided earlier in this work. As was noted, the adsorption process shifts the concentration of molecules from the bulk gas phase

closer to the surface of an adsorbent. This material transfer can be measured by various methods, the two most important being gravimetric and volumetric. Operation of these methods depend on a few common as well as specific corrections and assumptions. The common assumptions for most pure-component adsorption analyses is that the process occurs under isothermal conditions and that there is no mass exchange except for gas molecules in equilibrium between adsorbed and gas phases. Care must be taken to ensure that these assumptions are applicable to each test.

2.1.3.3 Gravimetric Methods

Gravimetric analysis is the direct measurement of sample weight which provides information on the quantity of gas adsorbed by a porous material. The data obtained from a gravimetric analysis instrument is very reliable as the only assumption is that the internal sample temperature equals the ambient temperature in the pressure chamber. Placement of a thermocouple in close proximity to the sample can minimize errors due to heat transfer, except at extremely low pressures where conductive heat transfer is inhibited. Additionally, the instrument can be configured to record data in real-time, yielding adsorption kinetics information and can directly show whether a sample has reached equilibrium. An additional benefit of gravimetric analysis is the ability to attain pre-defined equilibrium pressures.

The measured weight change can be directly used to obtain the excess adsorbed amount. Conversion from excess adsorption to total adsorption involves a secondary measurement of the sample in helium in order to obtain a buoyancy correction. This buoyancy correction has proven to be difficult to obtain with the instruments available. Additionally, this conversion is not necessary for much of this work as differences

between excess and total adsorbed amounts vary less than the measurement error over the pressure range of 0 to 10 bar. Pressures above 10 bar are measured only for presentation and comparison purposes as the focus of this work is on low pressure adsorption. Therefore, all reported values in this work are excess adsorbed amounts.

The equipment used for pure-component gravimetric gas adsorption analysis is an Intelligent Gravimetric Analyzer (IGA-001) from Hiden Isochema, Inc. The software used to record and analyze data was IGASwin Systems Software.

2.1.3.4 Volumetric Methods

Volumetric analysis is the indirect measurement of the amount of gas adsorbed via a mole balance on the gas phase. For this work, the Peng-Robinson equation of state was used to calculate the number of moles of gas in the gas phase. By conducting a mole balance on a reference chamber and the sample chamber, the excess adsorbed amount can be determined. As gas is adsorbed, the pressure in the sample chamber drops until equilibrium is reached. This precludes the ability to reach pre-determined pressures, a difficulty that is easily overcome by fitting data to isotherm models.

Direct measurement of sample temperature is possible in volumetric systems, but the one built and used in this study does not have this capability. Due to the lack of direct temperature measurement, a thermal equilibration time was considered to be 30 minutes and standard operation doubles this time to ensure equilibrium is reached.

The apparatus used to obtain volumetric adsorption data was constructed in-house. Two samples are placed side-by-side in a water bath with a heating and stirring pump maintaining bath temperature. All fitting are of Swagelok® or VCR® type and the valves were ultra-low leak rate valves purchased from Swagelok. Four pressure

transducers and a signal conditioner with display were purchased from Honeywell and used with factory calibrations. Calibration consisted of dead-volume tests with various non-adsorbing materials at various pressures, temperatures, and volumes. Further information about this instrument can be found in Appendix B.

2.1.3.5 Water Vapor Adsorption

Vapor adsorption is challenging, particularly because it is difficult to measure pure-component vapors as a carrier gas flow is often required. Also, there exists the possibility for condensation leading to measurement errors. Two methods are possible, one being a static method where a pure vapor phase is established while the other uses a constant flow of vapor in a carrier gas at a constant composition. Combining the constant flow method with a gravimetric analyzer, isothermal measurements can be obtained in a relatively straightforward manner. With multiple mass flow controllers (MFC) controlling purge, dry carrier, and saturated carrier gas streams, the composition of the flow entering the sample chamber can be set. The difference between the amount of water adsorbed and the carrier gas, often N_2 or He, is great enough to assume only water vapor adsorbs and the carrier is insignificant.

The apparatus used to obtain the water vapor isotherms is an Intelligent Gravimetric Analyzer (IGA-003) from Hiden Isochema, Inc. The original configuration of this instrument was altered by removal of the downstream mass spectrometer, as it was found to have inherent design incompatibilities during operation. Additionally, all exhaust from this instrument was transmitted via tubing to a nearby fume hood. These changes do not affect mass measurement of vapor adsorption in an inert gas. The software used to record and analyze data was IGASwin Systems Software.

2.1.3.6 Breakthrough Analysis

Dynamic bed adsorption, commonly referred to as breakthrough analysis, is a method for measuring non-equilibrium gas adsorption. Three major components are needed: gas supply controllers, a packed bed of sample, and a detector. Steady state flow is established in the bed by flowing a purge gas, such as helium, through at the same rate as the experiment. At the start of the experiment, gas entering the bed is switched from purge to the experimental composition via a valve or switches. The gas mixture passes through the bed with all or a portion adsorbing until the bed reaches saturation. Once the bed is saturated with a component of the mixture, that individual component "breaks through" and is detected downstream. This type of experiment is very relevant to real-world systems and data obtained can be used as-is for design of many applications.

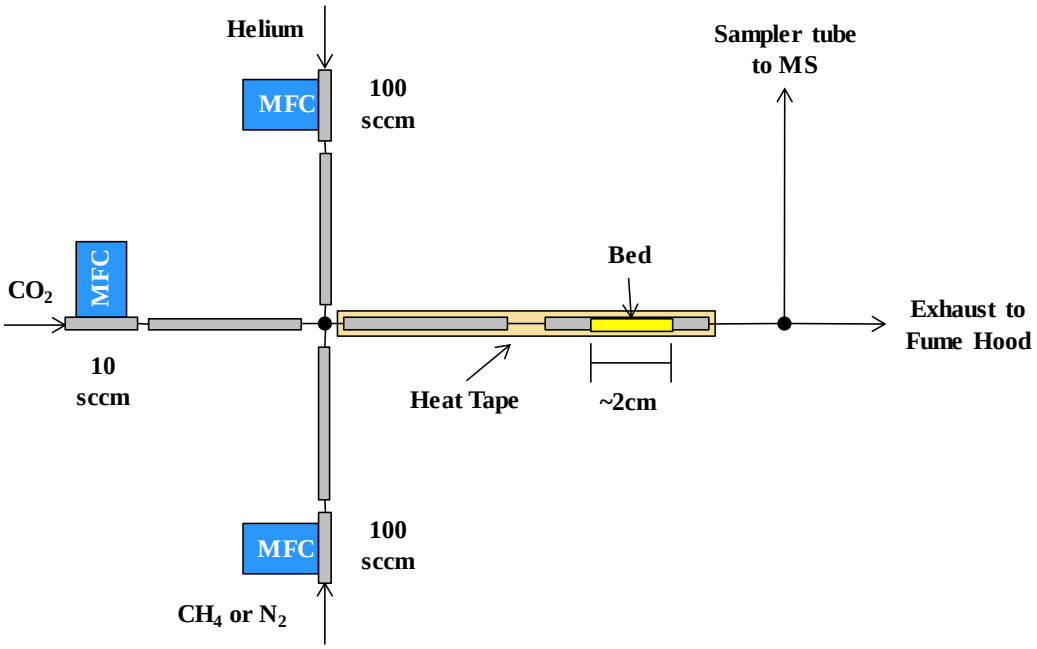

Figure 2.1. Schematic of the instrument used in this study. Flowrate capabilities are presented for MFCs calibrated to N_2.

The apparatus, shown in Figure 2.1, used to measure the breakthrough times of various gas mixtures studied in this work was built by a colleague in the Walton Research Group. It was designed for toxic gas breakthrough experiments and thus was built for remote control in order to place the entire apparatus in a fume hood. A set of external switches was used to control the MFCs. This is a less-than-ideal situation as all mechanical devices, including MFCs, do not operate instantaneously. The MFCs used here are rated to attain set point within 1.5 seconds, which is one order of magnitude less than the breakthrough times measured. All materials were 316SS tubing with VCR® or Swagelok® fittings. The detector was a Hiden DSMS quadrupole mass spectrometer with a rate of measurement of once every 1.8 seconds. The software used to record data was MASsoft. Further details on this process are provided in Appendix A.

2.2 Sample Preparation for Adsorption Experiments

Many porous materials are synthesized in solution or strongly adsorb gases and vapors upon exposure to lab air during normal handling. Whatever molecules are present in the pore space, be it solvent, water, or various gases, must be removed in order to provide pore space for the desired adsorbate. Typical activation entails heating of the sample at reduced pressure, but some considerations are required.

A general activation method, beginning with a material isolated from its reaction solution, typically involves repeated washes. The first series of washes are with a strong solvent, usually the same as used for synthesis, in order to remove unreacted materials from the surface and pores of the material. Additional washes are often conducted in order to exchange the strong solvent with a more readily vaporized solvent. If the

material may be air sensitive, then it is stored in a solvent-laden or "wet" condition until further use, as it has been found to inhibit sample degradation by preventing contact with air. Otherwise, the sample is air-dried, as dry powders are more easily loaded into sample cells. In the case of electrically insulating materials, such as glass, static buildup can cause problems for powder loading and weight measurement. Static can be eliminated with a wipe from anti-static sheets over the outside of the cell and then wiping off residue with a lint-free wipe.

For BET analysis, up to four samples are prepared concurrently. Weights of all sample cell equipment is obtained beforehand. A sample is prepared by loading between 20 and 50 mg of sample into a glass tube which is rounded at one end. A cap with an internal check valve is inserted into the open end of the glass cell, sealing it from further contact with lab air. The capped sample cell is connected to a vacuum manifold and a vacuum is gently applied in order to prevent powder from elutriating. The end of the cell where the sample lays is placed in a heating jacket and the temperature is slowly raised to a prescribed activation temperature, which is maintained by a PID temperature controller. Actual sample temperature is expected to be roughly 20°C below the set point.

For volumetric analysis, two samples can be concurrently tested and are prepared simultaneously. Roughly 50 mg of sample is loaded into a sintered stainless steel filter, acting as a sample pan. The sample pans are covered with only enough aluminum foil to secure the powder. The sample pan is placed into the cell and a number of filler blocks of aluminum foil are placed to minimize cell volume and secure the sample. The two sample cells are connected to a separate vacuum manifold and vacuum is slowly applied and monitored via the pressure transducers. The portion of the cell with the sample is

wrapped in heat tape, taking care to not overlap sections of the tape. The heat tape is connected to a variable autotransformer in order to control the current flow which is adjusted until the desired temperature is maintained. Temperature is monitored with a thermocouple placed between the tape and the metal sample cell surface and is assumed to be equal to the sample temperature due to the high thermal conductivity of steel.

For gravimetric (IGA) analysis, a single sample can be tested at a time. A conical-shaped stainless steel mesh is the sample pan and is suspended from a wire connected to the mass balance. The instrument has a thermocouple immediately beside the sample pan without touching. A stainless steel pressure vessel surrounds both, again without touching. The vessel is sealed by compression on a copper gasket and an external heat source is attached to the outside of the vessel. A vacuum is drawn on the chamber at a rate of 200 mbar/min. Heat is supplied by an external furnace capable of up to 400°C, but the internal chamber temperature is below this due incomplete insulation and poor heat transfer at low vacuum. The temperature is set by adjusting the furnace temperature and monitoring the internal temperature until it reaches within 5°C of the correct temperature. The mass is directly monitored while heat and vacuum are maintained on the sample chamber, allowing for direct observation of completeness of activation.

For breakthrough analysis, a single sample can be tested at a given time. The sample cell is a straight-through run of ¼" SS316 tubing with VCR® fittings on the ends. At each step the total weight is recorded. First, a glass wool plug is inserted, followed by pouring the sample into the cell and tapping the tube to promote settling. Roughly 100mg of sample is used to produce a 2cm long bed. A second glass wool plug is

inserted in order to prevent sagging of the bed which does not require significant force. The cell is connected to the apparatus by gaskets with a sintered filter core, in order to prevent elutriation or blowout. Once the apparatus is sealed, vacuum is applied to the sample cell using a bypass line connected to the vacuum system of the MS. Vacuum is slowly achieved by gradually shutting the system exhaust valve. Heat tape is wrapped around the tube with a thermocouple placed against the metal and power is controlled by a PID temperature controller.

One major consideration for the breakthrough analysis is the configuration of the bed. Since the apparatus necessitates a horizontal orientation, bed sagging can occur which leads to uneven flow through the bed or even a channel can develop. The evidence of this is a disperse breakthrough curve, indicative of bulk mass transfer limitations. Also, low pressure drop would indicate the presence of this problem. Neither of these factors were observed in this work, in fact the calibration and experiment curves were roughly parallel despite being far from plug flow.

2.3 Data Analysis

Software which is required to operate and/or analyze data obtained from a specific instrument is listed in the relevant portion in previous sections. The list of non-instrument specific software used to analyze data or prepare figures is Microsoft Excel, Microsoft Word, Microsoft PowerPoint, OriginPlot, Mercury, Matlab, and ChemSketch. References and citations were managed with Mendeley and EndNote.

2.3.1 *Isotherm Modeling*

Two primary isotherms were used to model the single-component isotherms. The first is the Toth model given (Eq. 2.8) and the second is the Langmuir model (Eq. 2.9).

$$q = \frac{q_{sat} bP}{(1 + (bP)^t)^{1/t}} \tag{2.8}$$

$$q = \frac{q_{sat} bP}{(1 + bP)} \tag{2.9}$$

where q_{sat} is saturation capacity, b is adsorption affinity, and t is a fitting parameter for the Toth equation related to the adsorption interaction heterogeneity.

These models are commonly used to fit a set of discrete data obtained from an isotherm measurement at various pressures and obtain a continuous equation. The Langmuir model can fit most isotherms well, particularly for weakly adsorbing species such as N_2 and CH_4. The Toth model is more accurate for adsorption systems with more heterogeneous interactions such as CO_2. The fit equations obtained from these models can be used to predict many other adsorption properties and further modelling.

2.3.2 *Heat of Adsorption*

Heat of adsorption is an important factor for adsorption processes as the amount of heat required to drive adsorption and desorption during industrial scale cycles can be significant. The adsorption process is an equilibrium process, therefore the Clausius-Clapeyron equation (Eq. 2.10) can be utilized to determine the energy required for the phase transition at various temperatures.

$$\frac{dP}{dT} = \frac{Q}{T\Delta V} \tag{2.10}$$

where Q is enthalpy of adsorption, V is molar volume, P is pressure, and T is temperature.

This equation can be simplified by assuming ideal gas behavior (Eqs. 2.11 and 2.12).

$$\Delta V = V_{gas} * \left(1 - {V_{liq}}/{V_{gas}}\right) \approx V_{gas} = \frac{RT}{P} \tag{2.11}$$

$$\left.\frac{\partial \ln P}{\partial\, {1}/{T}}\right|_{q_{st}} = -\frac{Q}{R} \tag{2.12}$$

where V_{gas} is gas molar volume, V_{liq} is liquid molar volume, and q_{st} indicates the partial derivative is taken at constant loading (isosteric).

This equation can be fit to a plot of lnP vs 1/T at various constant loadings, and the slope is directly related to Heat of Adsorption at that loading. Isotherms measured at three separate temperatures are required, in order to determine a statistically relevant linear fit. The difference in temperature required for accuracy is typically 20K between each isotherm (e.g. 298K, 318K, 338K), although a more precise instrument can allow for a smaller temperature steps. In the case of using the IGA-001 instrument, three isotherms measured every 10K, beginning with 298K, were found to be sufficient.

The heat of adsorption obtained from this equation can be used to produce a more complete isotherm model. Since adsorption is an equilibrium process, it can be modelled by an Arrhenius-type equation. This effect of temperature is incorporated into the adsorption affinity parameter (Eq. 2.13).

$$b = b_o * \exp\left(-\frac{Q}{R}\left(\frac{1}{T_o} - \frac{1}{T}\right)\right) \tag{2.13}$$

where b_o is adsorption affinity at reference temperature T_o.

2.3.3 *Ideal Adsorbed Solution Theory*

Ideal Adsorbed Solution Theory is a computationally easy method for prediction of mixture adsorption. This method, derived by Myers and Prausnitz[4], requires only pure-component isotherms of each gas at a single temperature in order to predict a multicomponent isotherm at the same temperature. The details of the derivation will not be reproduced, but the assumptions and resulting system of equations will be discussed.

The primary assumption is that the adsorbed phase behaves ideally, thus the name of the theory. This assumption is hardly accurate in all systems, particularly in cases where one or both components have dipole moments, strong quadrupole moments, or the potential to hydrogen bond. Examples where it often is a valid assumption are hydrocarbon mixtures, CH_4/N_2, or noble gases. Although CO_2 is not a perfect candidate for applying IAST, mixtures with CO_2 can still be well predicted by IAST. Water

adsorption is in nearly all cases impossible to accurately model using IAST due to the numerous non-idealities which occur as loading increases.

For most cases, the seven equations can be reduced to three by assigning the system pressure (P) and the gas phase composition of both components (y_1, y_2). In the case where $y_1+y_2 < 1$, the remaining fraction in the gas phase, comprised of Helium, was assumed to be completely inert and non-adsorbing, a reasonable assumption. Thus the values to solve for are (P^o*y_1), (P^o*y_2), and x_1 (Eqs. 2.14-2.16).

$$\int_0^{(P^o y_1)} \frac{f_1(t)}{t} dt = \int_0^{(P^o y_2)} \frac{f_2(t)}{t} dt \tag{2.14}$$

$$P * y_1 = (P^o y_1) * x_1 \tag{2.15}$$

$$P * y_2 = (P^o y_2) * x_2 \tag{2.16}$$

where $f_n(t)$ is an isotherm equation, t is an arbitrary integration variable, P is the total system pressure, P^o is the hypothetical pressure corresponding to the adsorbed phase mixture loading, y_i is the gas phase fraction of component i, and x_i is the adsorbed phase fraction of component i.

When this system is solved, the total number of moles adsorbed at the condition of [P,y_1,y_2] can be calculated (Eqs. 2.17-2.19).

$$n_{total} = 1/\left({x_1}/{f_1(P^o y_1)} + {(1-x_1)}/{f_2(P^o y_2)}\right) \quad (2.17)$$

$$n_1 = x_1 * n_{total} \quad (2.18)$$

$$n_2 = (1-x_1) * n_{total} \quad (2.19)$$

where n_{total} is the total number of moles adsorbed and n_1 and n_2 are the number of moles adsorbed for components 1 and 2, respectively.

Finally, selectivity can be calculated (Eq. 2.20).

$$S_{1,2} = \frac{{y_1}/{x_1}}{{y_2}/{(1-x_1)}} \quad (2.20)$$

where $S_{1,2}$ is the adsorption selectivity for component 1 over component 2.

Thus the resulting calculated values of $[n_1,n_2]$ at specified $[P,y_1,y_2]$ allows for fitting a multicomponent Langmuir equation (Eq. 2.21). This equation can be utilized for further modeling efforts with reduced computational load while maintaining accuracy.

$$q_i = \frac{q_{sat,i} b_i P_i}{\left(1 + \sum_j b_j P_j\right)} \quad (2.21)$$

where q_i is the amount of component i adsorbed, P_i is the partial pressure for each gas phase component, and b_i and $q_{sat,i}$ are fitting parameters.

2.4 Mathematical Modeling

The software used to model and predict breakthrough behavior of various materials was Mathematica. This program was chosen for several reasons, including its immediate availability via student licensing, numerous example codes, and robust calculation packages. By eliminating the need to implement and refine mathematical methods, the focus of the work could remain on engineering aspects of the modeled system. Further details are provided in Appendix A.

2.5 References

1. Bragg, W.L., *The structure of some crystals as indicated by their diffraction of x-rays.* Proceedings of the Royal Society of London Series a-Containing Papers of a Mathematical and Physical Character, 1913. **89**(610): p. 248-277.

2. Brunauer, S., P.H. Emmett, and E. Teller, *Adsorption of gases in multimolecular layers.* Journal of the American Chemical Society, 1938. **60**: p. 309-319.

3. Walton, K.S. and R.Q. Snurr, *Applicability of the BET method for determining surface areas of microporous metal-organic frameworks.* J Am Chem Soc, 2007. **129**(27): p. 8552-6.

4. Myers, A.L. and J.M. Prausnitz, *Thermodynamics of Mixed-Gas Adsorption.* Aiche Journal, 1965. **11**(1): p. 121-+.

CHAPTER 3

TUNING THE ADSORPTION PROPERTIES OF UIO-66 VIA LIGAND SUBSTITUTION

Parts of this work are taken from Cmarik, G. E., Kim, M., Cohen, S. M., & Walton, K. S. (2012). Tuning the adsorption properties of UiO-66 via ligand functionalization. *Langmuir* **2012**, 28, 15606.

3.1 Introduction

Adsorption is an important separation process in numerous industrial applications. Two major applications are natural gas sweetening and carbon dioxide capture from flue gas.[1] Solid adsorbents offer one of the most promising routes to energy efficient separations in these processes. Several specific attributes are required when selecting an adsorbent for a separation process. The adsorbent must be stable and reusable, possess high capacity and selectivity for the target molecule, and require minimal energy to regenerate.

Hybrid organic-inorganic adsorbents, such as metal-organic frameworks, have been well studied for their adsorption properties with regard to CH_4 and H_2 storage as well as CO_2 capture.[1-4] Many MOFs have exceptional properties including high adsorption capacity,[5] selectivity,[6] surface areas,[7] and stability.[8, 9] However, a number of concerns still exist surrounding MOF stability, and this has been the focus of several recent studies.[10-12] An important feature of MOFs which offers a route to satisfying the adsorbent selection criteria is the modular nature of the organic linker. One MOF which

has been successfully synthesized with many different functional groups, exhibits exceptional stability, and has good adsorption properties is UiO-66.[13]

The UiO-66 family of microporous materials is based on a 3-D structure of zirconium-oxide clusters and carboxylate linkers. UiO-66 is synthesized with benzene dicarboxylate (bdc^{-2}), and many modified dicarboxylate linkers and even tetracarboxylate linkers have also been successfully used to synthesize functionalized versions of UiO-66.[14, 15] To date, experimental studies have reported the adsorption properties of the parent UiO-66 material[16-18] as well as two functionalized variants,[19] and a computational study has predicted a number of additional functionalized variants.[18] Until now, no experimental study of the impact on the gas and water vapor adsorption properties caused by modulation of the functionalities has been done for the promising UiO-66 family of materials.

Previous studies on the impact of functional groups on adsorption properties for other materials have been published. Two comparable series of MOFs have been synthesized with a number of modified linkers in a similar manner to the UiO-66 materials studied here: IRMOF[20, 21] and DMOF.[22-24] The published results indicate the most promising adsorption enhancements occur for certain polar functional groups; particularly amino, alkoxy, and nitro functional groups.[20] The results also indicate improved hydrophobic character with addition of non-polar functional groups such as naphthyl functionalities.[25, 26] Neither the IRMOF nor the DMOF series of materials are suitable for humid systems due to framework degradation[11] whereas UiO-66 is stable.[13]

In this work, we report the CO_2, CH_4, N_2, and water vapor adsorption properties of UiO-66 and four functionalized variants of UiO-66 including a new material, UiO-66-

2,5-$(OMe)_2$. Additionally, isosteric heats of adsorption are calculated for each of the pure component gases. Amino, nitro, methoxy, and naphthyl functional groups were chosen to be representative of polar, basic and hydrophobic functionalities. The results indicate that the polar functional groups improve CO_2/CH_4 and CO_2/N_2 selectivity with the amino group showing the best performance. All of the materials are shown to be stable after water vapor exposure and adsorb water regardless of the nature of the organic linker.

3.2 Experimental Methods

3.2.1 *Chemicals*

Zirconium(IV) chloride, terephthalic acid, 2-aminoterephthalic acid, 2-nitroterephthalic acid, 1,4-naphthalenedicarboxylic acid, glacial acetic acid, methanol, and N,N-dimethylformamide were procured from commercial sources (Fisher and SigmaAldrich). N,N-dimethylformamide was stored over 3A molecular sieves prior to use, and all other chemicals were used without modification. 2,5-Dimethoxyterephthalic acid was synthesized via Williamson etherification as previously reported.[27]

3.2.2 *Materials Synthesis*

Materials were synthesized following procedures previously reported.[14] A modification of the procedure was used to produce UiO-66-2,5-$(OMe)_2$, specifically, 600 μL of glacial acetic acid was added to the reaction solution and the oven temperature was reduced to 110 °C.

3.2.3 *Materials Activation*

After synthesis was complete, the samples were transferred to centrifuge tubes. The sample powders were recovered by centrifugation and decanting. Washing of the

powders consisted of soaking for 1 hour in 10 mL of fresh DMF followed by centrifugation 3 times. Washed samples were solvent exchanged by soaking for 1 day in 10 mL of methanol followed by centrifugation 3 times. Solvent exchanged samples were dried under vacuum at 105 °C.

3.2.4 *Experimental Methods and Procedures*

Nitrogen adsorption isotherms were obtained at 77 K using a multi-port volumetric apparatus (Quadrasorb, Quantachrome). Pure-component isotherms were measured in a gravimetric adsorption apparatus (IGA-1, Hiden Isochema) from 0 to 20 bar at 25 °C and 0 to 3 bar at 25 °C, 35 °C and 45 °C. Activation of the samples was conducted in situ at 110 °C and under vacuum. The sample density of UiO-66-NH_2 was experimentally determined to be 3.5 g/cc via helium displacement. This density was used for each of the UiO-66 materials in the buoyancy correction of the adsorption isotherm. A density of 3.5 g/cc is significantly higher (~200%) than the estimated sample density of 1.3 g/cc based on the volume and weight of an ideal unit cell of UiO-66-NH_2.[18] The impact of this seemingly large difference on the resulting isotherm is the higher density will show a reduced uptake by less than 2% below 5 bar but up to 8% at 20 bar. Water vapor isotherms were measured using a gravimetric adsorption apparatus (IGA-3, Hiden Isochema) in flowing mode at 1 bar and 25 °C with dry air as a carrier gas. Brunnauer-Emmett-Teller (BET) surface area calculations were conducted over a pressure range of $0.007<p/p_o<0.035$ which produces results consistent with the two criteria for accurate surface area determination put forth by Walton and Snurr.[28]

The gases used in the adsorption experiments are carbon dioxide, methane, nitrogen, helium, and dry air. All gases are Ultra-High Purity or Bone Dry Grade (Airgas).

3.3 Results and Discussion

3.3.1 *Surface Area Analysis*

Nitrogen adsorption at 77 K was used to determine the surface areas of the samples. The results are presented in Table 3.1. The BET surface areas for UiO-66, UiO-66-NH_2, and UiO-66-NO_2 are identical to or slightly higher than previously reported values.[14] The BET surface area for UiO-66-1,4-Naph is higher than previously reported value of 615 m^2/g.[14] UiO-66-2,5-$(OMe)_2$ would be expected to have similar or lower surface area than the nitro- and naphthyl-functionalized materials based on additional framework mass and linker size but instead the opposite result is observed. This result may be attributed to the flexibility of the methoxy groups allowing additional nitrogen to be adsorbed in the monolayer.

Table 3.1. BET Surface Areas of Functionalized UiO-66 Materials (m^2/g)

Sample	BET Surface Area[α]
UiO-66	1105 ± 15
UiO-66-NH_2	1123 ± 64
UiO-66-NO_2	792 ± 27
UiO-66-1,4-Naph	757 ± 9
UiO-66-2,5-$(OMe)_2$	868 ± 31

[α]Results are an average of two independent experiments.

3.3.2 *Carbon Dioxide Adsorption: Pure-Component Isotherms*

As shown in Figure 3.1, the two major regimes of adsorption are plainly evident within the measured range of pressures for the entire series of UiO-66 materials. At low pressures, the polar functionalities show a significant increase in uptake over the non-polar groups. Specifically, UiO-66-NH_2 shows the highest uptake, followed by nearly identical low pressure uptake for the nitro and dimethoxy functionalities. The lower uptakes of UiO-66-NO_2 and UiO-66-2,5-$(OMe)_2$ are attributed to reduced pore volume and surface area induced by the bulkier functional groups.

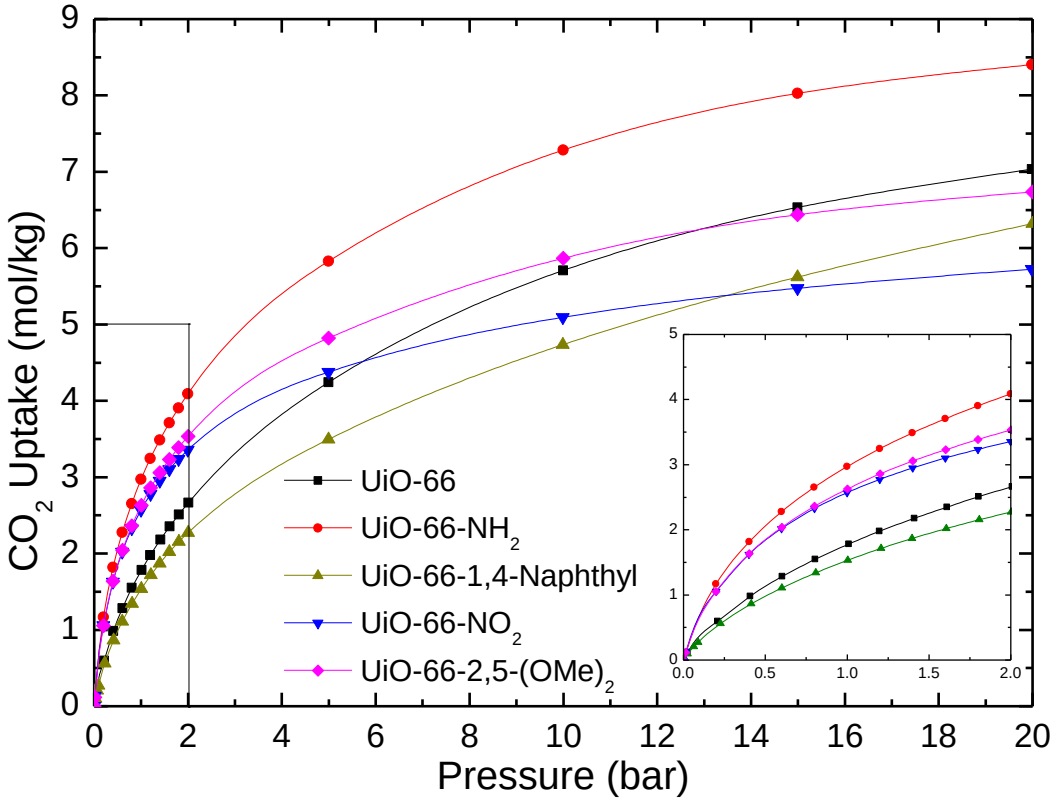

Figure 3.1. CO_2 uptake versus pressure at 298K.

UiO-66 and UiO-66-1,4-Naph exhibit lower uptake at low pressures due to the nonpolar organic linkers. The naphthyl functionality imparts greater molar mass, smaller pore volume, steric hindrance near the metal cluster, and no significantly stronger surface binding sites, thus leading to decreased adsorption performance at higher loadings versus UiO-66.

In the high pressure regime, where pore volume effects become important and the favorable adsorption sites are occupied, the size of the functional group in the pore space becomes evident. Each of the isotherms shows the characteristic plateau at high pressure. UiO-66-NO_2 has the most apparent plateau, but the origin of this effect is not apparent as

this material has similar pore volume and surface area to the naphthyl- and methoxy-functionalized materials. UiO-66-2,5-$(OMe)_2$ likewise shows the limitations of bulky functional groups, but the impact is not as severe as with the nitro group.

3.3.3 *Carbon Dioxide Adsorption: Heat of Adsorption*

An important factor in characterizing adsorbents for practical applications is the isosteric heat of adsorption. Pure-component adsorption isotherms were obtained for each sample at 298 K, 308 K, and 318 K. These isotherms were parameterized using the Toth model[29] given in equations 3.1 and 3.2,

$$\theta = \frac{bP}{(1 + (bP)^t)^{1/t}} \tag{3.1}$$

where P is equilibrium pressure, b is the adsorbent affinity, t describes the heterogeneity of the adsorbent surface, and θ is the fractional loading defined as,

$$\theta_i = \frac{q_i}{q_i^{sat}} \tag{3.2}$$

The isotherms were recalculated at specific CO_2 loadings and the implicitly determined pressures were used in the Clausius-Clapeyron equation to calculate the isosteric heat of adsorption from equation 3.3.

$$\frac{q_{st}}{RT^2} = -\left(\frac{\partial \ln P}{\partial T}\right)_q \tag{3.3}$$

The results of these calculations are shown in Figure 3.2.

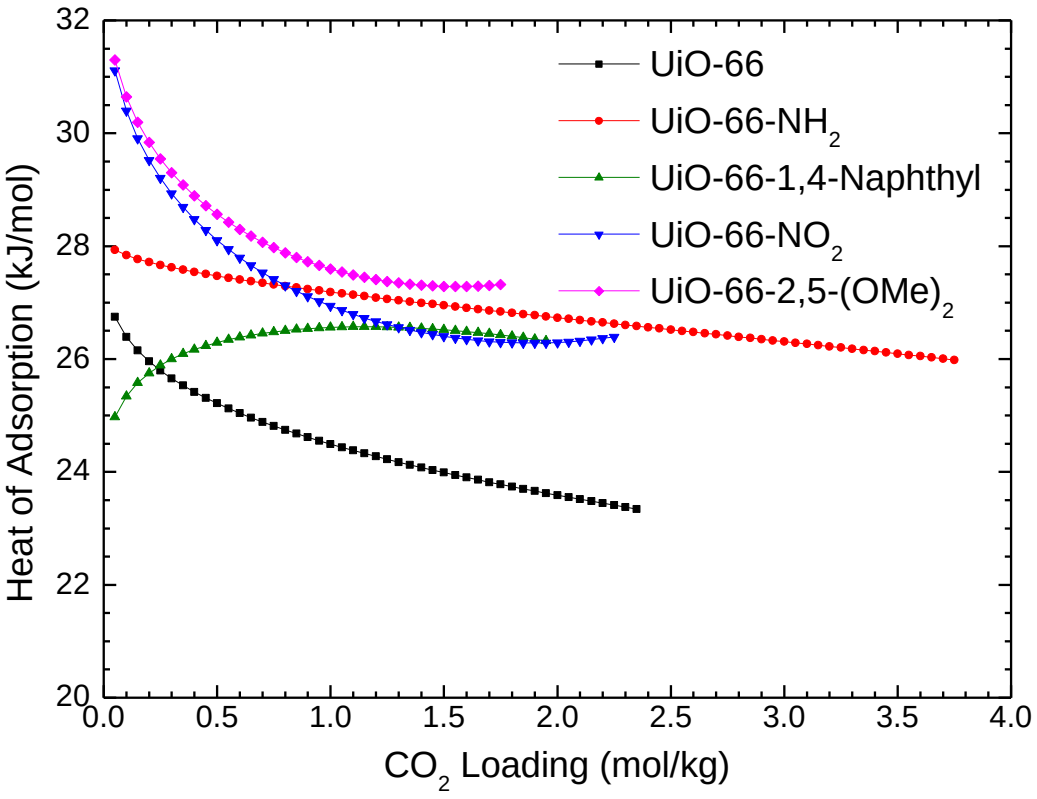

Figure 3.2. Isosteric heat of adsorption as a function of CO_2 loading.

The isosteric heat of adsorption at low loading for UiO-66 is nearly identical to the predicted zero loading heat of adsorption at 27 kJ/mol.[18] As loading increases, the calculated heat of adsorption drops from 26 to 24 kJ/mol, which is slightly below the previously reported experimental values which stay constant at 26 kJ/mol.[16] This

difference is small and may be an artifact of the parameterization using the Toth model. As loading decreases, the heats of adsorption for UiO-66-NO_2 and UiO-66-NH_2 approach the predicted zero loading values.[18] The heats of adsorption for the naphthyl- and methoxy-functionalized materials were not predicted as a part of the computational study.[18]

For the four functionalized materials studied, the plot reveals a few important trends. The first trend is that the heat of adsorption for all of the functionalized materials converges to 27 kJ/mol as loading increases. This may be attributed to the constriction of pores due to the functional groups. The second is that the bulky and polar functional groups show a high initial heat of adsorption and a steep drop as loading increases, which is indicative of the presence of strong adsorption sites. The non-polar naphthyl functionality has the lowest zero loading heat of adsorption and, surprisingly, shows an increase in heat of adsorption as loading increases. This increase suggests the bulky and non-polar aromatic ring sterically hinders access to the stronger adsorption sites at the metal cluster.

UiO-66-NH_2 has a relatively flat isosteric heat of adsorption profile, which is a desirable feature for efficient adsorbent regeneration. This is unlike the other two polar functionalized materials, where the bulky side groups create strong adsorption sites. The great improvement in uptake and increase in heat of adsorption over UiO-66 can thus be attributed to the dipole moment of the amine group and the small functionality size which does not reduce the accessible surface area. No chemisorption occurs with the mildly basic amine, which is evidenced by completely reversible isotherms and low heat of adsorption. This result is consistent with other amine-functionalized MOFs.[3]

3.3.4 *Methane Adsorption: Pure-Component Isotherms*

The methane isotherms in Figure 3.3 show a similar trend to CO_2, in particular the smaller and more polar functional groups lead to an increase in CH_4 uptake. The amino, nitro and methoxy functionalities each show greater uptake over UiO-66 and UiO-66-1,4-Naph at low pressures. This observed trend seems to be a convolution of the surface area and functional group polarity. The only exception seems to be UiO-66-NO_2, which shows a notably higher uptake over the methoxy-functionalized material until high pressures. This result is unlike the trend observed for CO_2 and may be attributed to the large size of the nitro functional group.

UiO-66-NH_2 and UiO-66-NO_2 show the highest uptake of CH_4 at low pressures. The nitro- and methoxy-functionalized materials begin to show a plateau at higher pressures indicative of their smaller pore volumes, but the limited pressure range prevents direct observation of the saturation region.

UiO-66 and UiO-66-NH_2 show lower CH_4 uptake than previously reported values.[16, 18] Since the XRD patterns, BET surface areas, and CO_2 adsorption isotherms are similar, the discrepancy may be attributed to the activation procedures. In the work by Wiersum et al., activation of unfunctionalized UiO-66 was performed at 250 °C in order to remove residual terephthalic acid.[16] However, all materials in this study were activated at 110 °C in order to reduce the risk of thermal degradation of functional groups. The differing activation conditions may account for the disagreement between the adsorption isotherms, but it fails to account for the nearly identical BET surface areas and CO_2 adsorption isotherms. The results presented here seem to be quite self-

consistent because the trend of increasing uptake with surface area and dipole strength is evident.

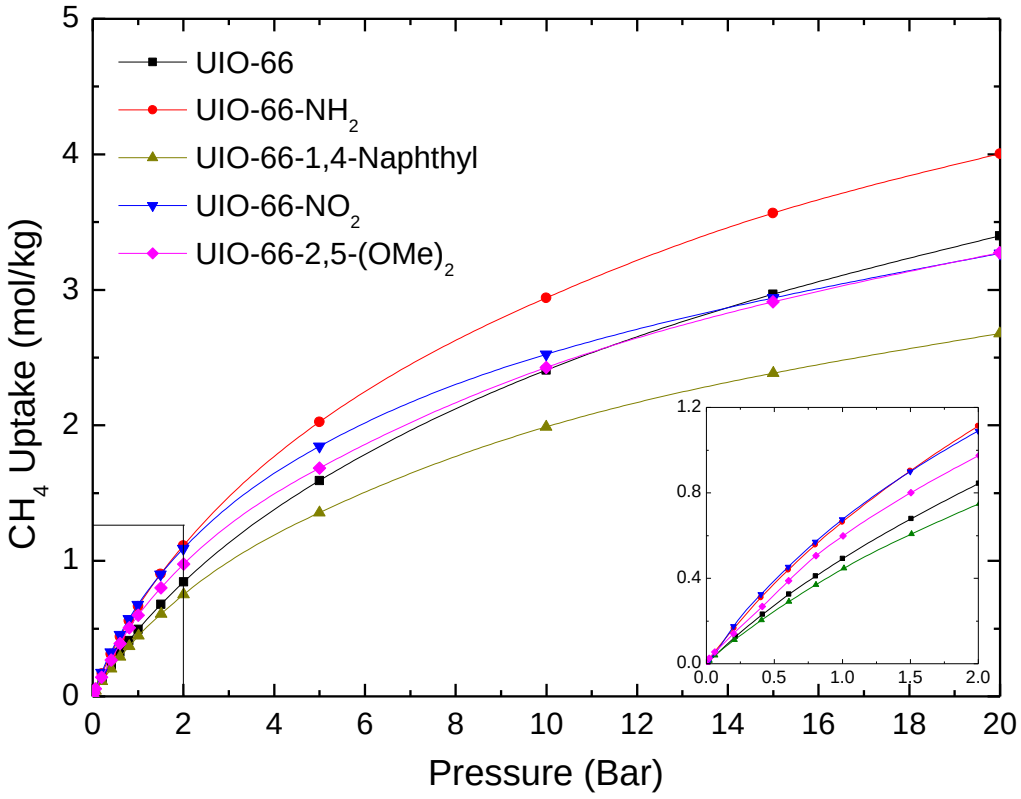

Figure 3.3. CH_4 uptake versus pressure at 298K.

3.3.5 *Methane Adsorption: Heat of Adsorption*

For each methane isotherm, with the exception of UiO-66-NO_2, the *t* parameter in the Toth model was fit to unity. Therefore, the pure-component methane isotherms were fit to the Langmuir model given in equation 3.4,

$$\theta = \frac{bP}{1 + bP} \tag{3.4}$$

where the symbols used are the same as in the Toth model. This change is not significant as methane is a weakly interacting adsorbate, and the isotherms can be well described by a homogenous adsorption surface model. The same method employed previously was used to calculate the heat of adsorption as a function of CH_4 loading. Figure 3.4 shows the results of these calculations.

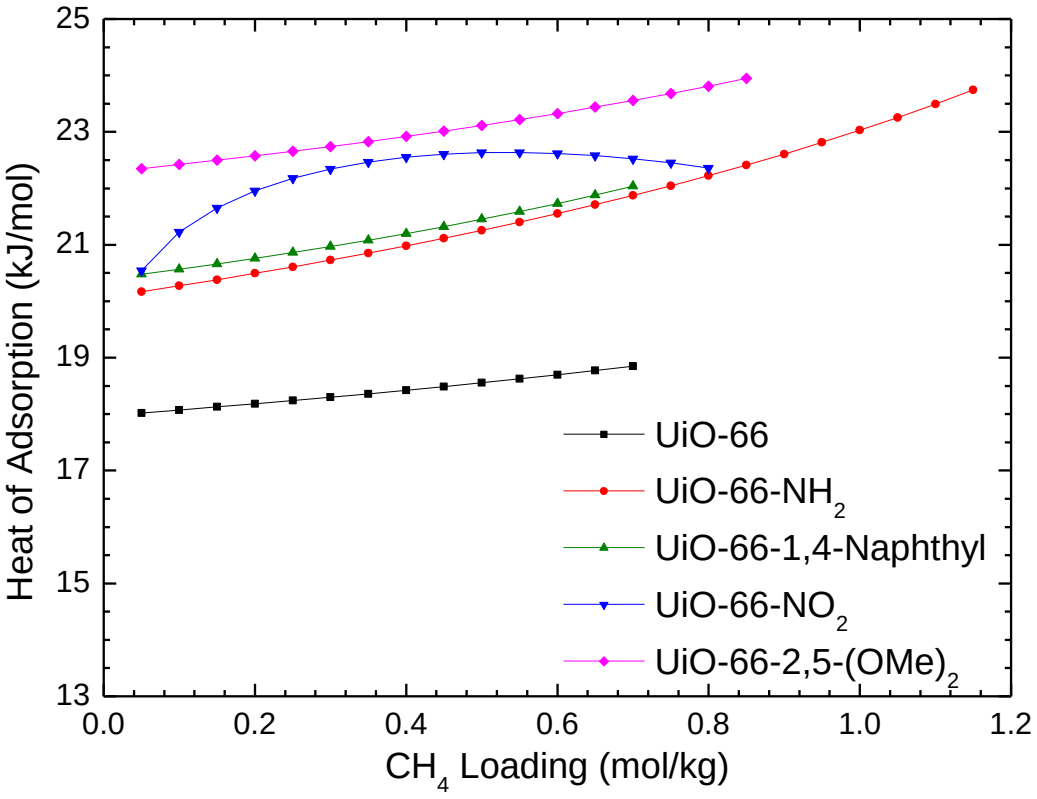

Figure 3.4. Isosteric heat of adsorption as a function of CH_4 loading.

The isosteric heats of adsorption for UiO-66, and UiO-66-NH_2 at zero loading are almost identical to predicted values[18] and results from microcalorimetry studies.[16] The curvature of the plot for UiO-66-NO_2 is inherent to the Toth model whereas the linear plots for the other are due to the use of the Langmuir model. The fact that the Langmuir model fit well for each material indicates a relatively homogenous adsorption environment. Also, the similar heat of adsorption between the polar and non-polar functionalities further confirms this assumption. Therefore, the heat of adsorption should entirely depend on the strength of the dipole-dispersion and dispersion-dispersion interactions. The trend would then be UiO-66-NO_2≈UiO-66-2,5-$(OMe)_2$>UiO-66-NH_2≈UiO-66-1,4-Naph>UiO-66, which is close to what is seen in Figure 3.4.

3.3.6 *Nitrogen Adsorption: Pure-Component Isotherms*

Nitrogen is an excellent probe molecule for determining the structural properties of the materials without the effects of strong surface or chemical interactions. High pressure isotherms were only measured for UiO-66 and UiO-66-NO_2 due the nearly linear nature of the measured isotherms. Since all of the N_2 isotherms are expected to be linear, the remaining materials were only tested at low pressures for heat of adsorption calculations. The results are shown in Figure 3.5.

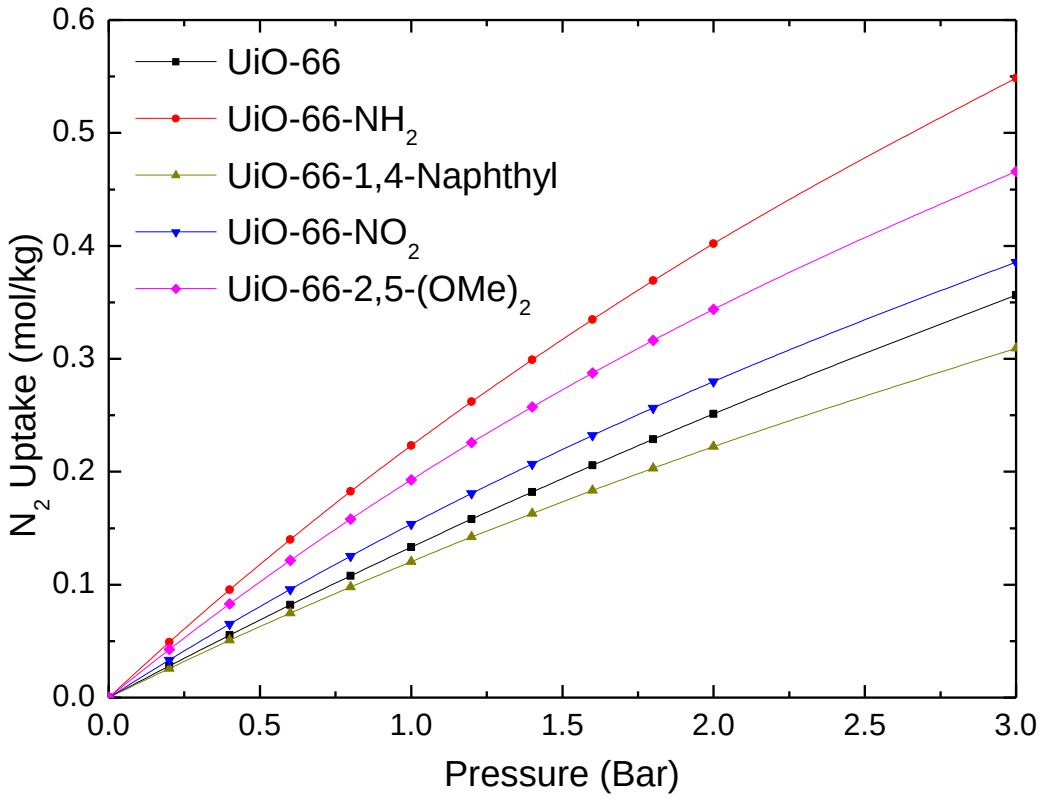

Figure 3.5. N_2 uptake versus pressure at 298K.

The same trends of polarity and surface area are evident just as they were with CO_2 and CH_4. The small, polar amino group has a higher uptake than the bulkier nitro and methoxy groups. UiO-66 remains below the three polar functionalities but above the naphthyl functionality due to lower molar mass.

3.3.7 *Nitrogen Adsorption: Heat of Adsorption*

The pure-component nitrogen isotherms were fit to the Langmuir model. The same method employed previously was used to calculate the heat of adsorption as a function of CH_4 loading. The results of the calculations are shown in Figure 3.6.

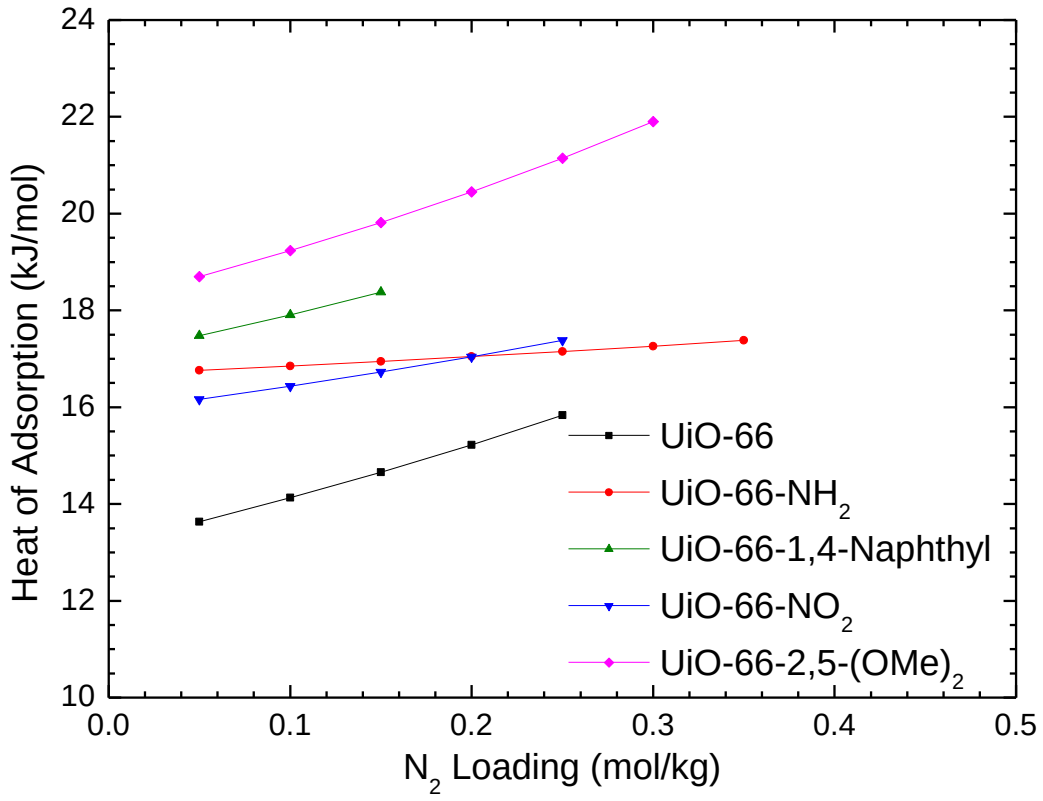

Figure 3.6. Isosteric heat of adsorption as a function of N_2 loading.

As is seen in the plots for CO_2 and CH_4, the isosteric heat of adsorption for UiO-66 is lowest at approximately 14 kJ/mol, and the functionalized materials are clustered higher at around 17 kJ/mol. This increase can be attributed to the reduced pore size of the functionalized materials. Beyond the initial observation that functionalizing the framework leads to an increase in the heat of adsorption, the trends are difficult to discern due to the low uptakes and thus small range of loadings over which the calculations are valid.

3.3.8 *Selectivity*

Selectivity is a fundamentally important issue for gas separation, and one method for determining ideal selectivity is calculating the ratio of the Henry's constants for two gases. Since Toth and Langmuir models were used to parameterize the measured adsorption isotherms for each material and each gas at 298K, 308K and 318K, calculation of the Henry's constant is simply the product of adsorption affinity, b, and saturation capacity, q^{sat}, given in equation 3.5.

$$H_i = q_i^{sat} * b_i \tag{3.5}$$

Table 3.2 shows the ratio of the Henry's constants for each pure-component gas at each measured temperature. The results show a much higher CO_2/N_2 selectivity for each material studied and a higher CO_2/CH_4 selectivity for the amino- and methoxy-functionalized materials over the unfunctionalized prototypical material: MOF-5 (CO_2/CH_4:15.53, CO_2/N_2:17.48).[30]

Table 3.2. Selectivity at various temperatures as determined from a ratio of Henry's constants

	T (K)	UiO-66	-1,4-Naph	$-NH_2$	$-NO_2$	$-2,5-(OMe)_2$
CO_2/CH_4	298	10.1	6.5	17.0	12.3	18.0
	308	7.5	7.3	18.3	10.3	14.2
	318	6.4	5.7	13.0	8.2	13.1
CO_2/N_2	298	37.5	30.0	66.5	51.4	62.2
	308	27.7	33.1	61.5	42.2	52.3
	318	21.9	23.9	43.0	31.7	39.7
CH_4/N_2	298	3.7	4.6	3.9	4.2	3.5
	308	3.7	4.6	3.4	4.1	3.7
	318	3.4	4.2	3.3	3.9	3.0

A more direct comparison of the effect of functional groups can be found in the isostructural family of DMOF-1, where the unfunctionalized materials shows a CO_2/CH_4 selectivity of 3.7[30] and the hydroxyl-functionalized variant, known as USTA-25a, shows a selectivity of 12.5.[31] In this case, the effect of addition of a small, polar functional group leads to a 3.5× increase in zero-loading selectivity, whereas for the UiO-66 materials an increase of only 1.7× is observed. One major difference between the two families of materials lies in the metal cluster of UiO-66. The hydroxylated metal cluster perhaps plays a significant role in CO_2 adsorption which leads to a smaller selectivity improvement upon functionalization of the organic linker in UiO-66.

Another pair of materials, MIL-53(Al) and NH_2-MIL-53(Al), show a CO_2/CH_4 selectivity of 5 and 60 respectively,[32] which is vastly higher than the increase for functionalization of UiO-66. Comparison to this family of materials is less than ideal due to the structural transistions that occur in the MIL-53 materials leading to different pore

structures at zero-loading.[33] In order to provide perspective on the selectivities reported herein, comparison to a number of known materials is given in Table 3.3.

Table 3.3. Selectivity of select reference materials at zero-loading and 298K.

Material	CO_2/CH_4	CO_2/N_2
Zeolite 13X[6]	395	N/A
Zeolite 5A[30]	256	240.56
MgMOF-74[6]	283	N/A
Cu-BTC[34]	21	N/A
MOF-5[30]	15.53	17.48
NH_2-MIL-53(Al)[32]	60	N/A
USTA-25a[31]	12.5	N/A

3.3.9 *Water Vapor Adsorption*

Figure 3.7 shows water adsorption isotherms at 298 K and reveals the hydrophilic and hydrophobic natures of the materials studied. UiO-66 and UiO-66-NH_2 have been previously studied, while the three additional materials are presented for comparison. All materials adsorb significant amounts of water regardless of the functionalities present. With the exception of UiO-66-1,4-Naph, all of these materials show a hysteresis indicative of pore filling.

UiO-66 is a hydrophilic material with an evident step in the isotherm indicative of pore condensation at 20% relative humidity. UiO-66-NH_2 and UiO-66-NO_2 are both hydrophilic and show immediate adsorption of significant amounts of water at low relative humidity. All three of these materials have similar isotherms, which can be attributed to the accessible metal cluster and polar functional groups.

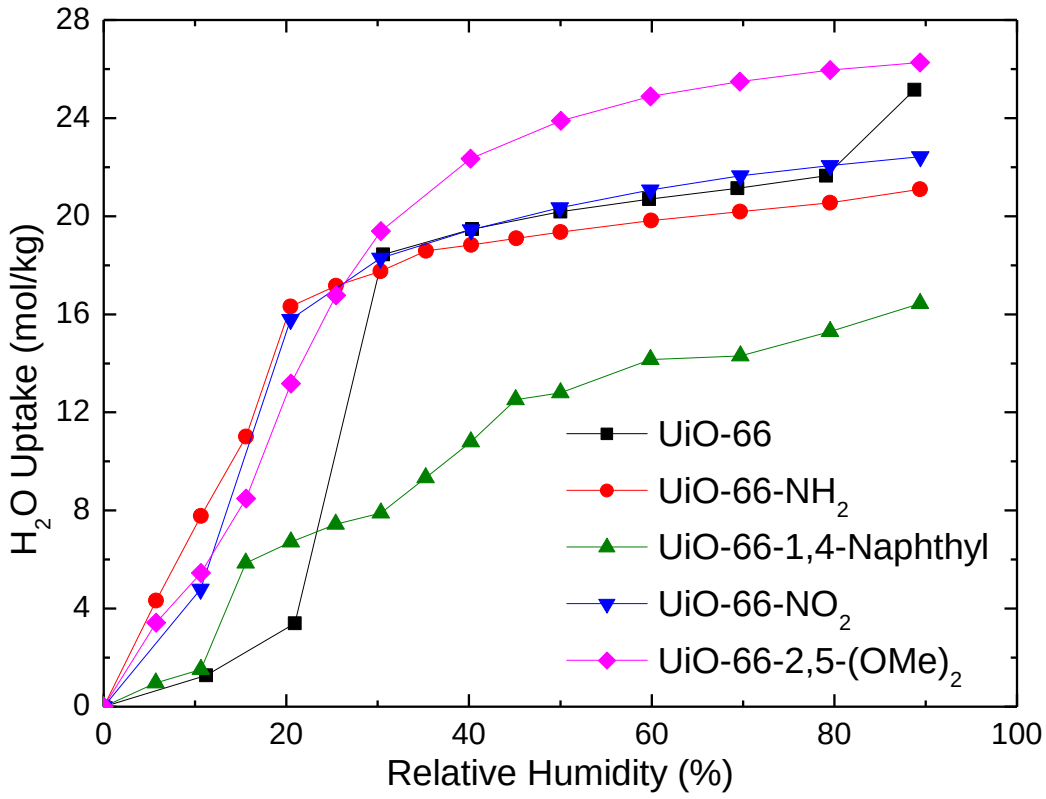

Figure 3.7. H_2O vapor uptake versus Relative Humidity at 298K and 1 bar. UiO-66 isotherm provided for comparison.[12]

UiO-66-1,4-Naph shows the most hydrophobic nature among the five materials but, unlike other naphthyl functionalized materials,[25, 26] it adsorbs significant amounts of water. One step change at 15% is evident, which is similar to all the functionalized materials and may be attributed to interactions with the metal cluster. This material shows a very small hysteresis which indicates pore condensation is limited. The unfunctionalized UiO-66 material shows similar water adsorption at low water vapor concentrations, but adsorbed large amounts of water above 20% relative humidity at the onset of pore filling. This indicates the naphthyl ring inhibits pore condensation of water, but does not prevent water adsorption entirely.

UiO-66-2,5-$(OMe)_2$ showed significant water uptake but no sharp step is evident in the isotherm which would indicate pore condensation. Adsorption saturation occurs above 60% relative humidity, whereas complete pore filling is evident for the amino- and nitro-functionalized variants at 20% relative humidity. As in the case of the naphthyl functionality, the methoxy functional group could inhibit water condensation within the pore.

3.3.10 *Stability*

Each of the samples was tested for stability upon exposure to water vapor via a before and after PXRD comparison. All samples show that structure is retained as evidenced in Figure 3.8. In each case, the peak positions and the ratios of peak heights remain the same indicating no loss of crystallinity. The crystalline structure of the frameworks clearly remain intact, although recent studies on this material show that ligand exchange reactions can occur in the presence of water.[35]

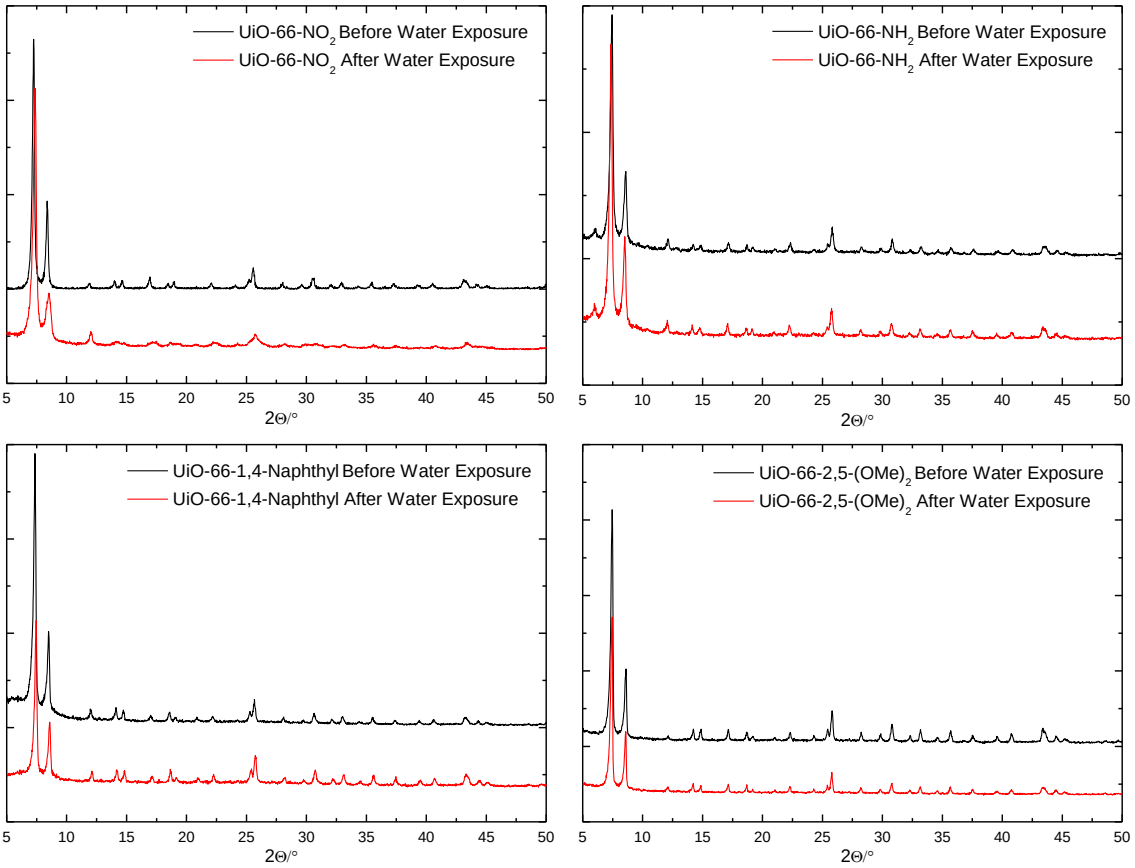

Figure 3.8. Powder XRD patterns before and after exposure to water vapor and subsequent reactivation.

3.4 Conclusions

UiO-66 can be synthesized with functionalized organic linkers and shows a wide variation in adsorption properties as a result of the different functional groups. UiO-66 and the amino-, nitro-, 1,4-naphthyl-, and 2,5-dimethoxy-functionalized versions of UiO-66 were studied. The results show that CO_2, CH_4, and N_2 uptake are improved with addition of small, polar functional groups that do not significantly reduce surface area and pore volume. The polar amino, nitro, and methoxy modifications show selectivity

improvements for CO_2/CH_4 and CO_2/N_2 over UiO-66. The naphthyl functional group is shown to reduce water vapor adsorption and prevent pore filling, but the material is not truly hydrophobic.

The isosteric heat of adsorption for CO_2 at low loading varies significantly between the five materials, but each of the four functionalized materials converge to approximately 27 kJ/mol at higher loadings. The isosteric heat of adsorption for UiO-66-NH_2 is roughly 28 kJ/mol at low loadings and decreases slightly as a function of loading whereas the nitro- and methoxy-functionalized materials have heats of adsorption around 32 kJ/mol at low loadings with a rapid decrease as loading increases. A smaller change in heat of adsorption as a function of loading is desirable in vacuum swing adsorption applications, which indicates that UiO-66-NH_2 is the most promising material studied here for dry applications.

The stability of each material on exposure to water vapor was confirmed with XRD. Water vapor adsorption studies revealed that the amino- and nitro-functionalized materials readily adsorb water and saturate near 20% relative humidity. The methoxy-functionalized material also readily adsorbs water, but does not saturate until approximately 60%. The naphthyl functionalized material did not show hydrophobic character as a significant amount of water was adsorbed, but pore filling did not occur. The good adsorption properties of the methoxy functionalized material and the inhibited water uptake indicates that alkoxy functional groups would be a good candidate for further study in wet applications.

3.5 References

1. D'Alessandro, D.M., B. Smit, and J.R. Long, *Carbon dioxide capture: prospects for new materials.* Angew Chem Int Ed Engl, 2010. **49**(35): p. 6058-82.

2. Keskin, S., T.M. van Heest, and D.S. Sholl, *Can metal-organic framework materials play a useful role in large-scale carbon dioxide separations?* ChemSusChem, 2010. **3**(8): p. 879-91.

3. Sumida, K., et al., *Carbon dioxide capture in metal-organic frameworks.* Chem Rev, 2012. **112**(2): p. 724-81.

4. Lin, X., N.R. Champness, and M. Schroder, *Hydrogen, methane and carbon dioxide adsorption in metal-organic framework materials.* Top Curr Chem, 2010. **293**: p. 35-76.

5. Llewellyn, P.L., et al., *High uptakes of CO2 and CH4 in mesoporous metal-organic frameworks MIL-100 and MIL-101.* Langmuir, 2008. **24**(14): p. 7245-50.

6. Bao, Z., et al., *Adsorption of CO2 and CH4 on a magnesium-based metal organic framework.* J Colloid Interface Sci, 2011. **353**(2): p. 549-56.

7. Furukawa, H., et al., *Ultrahigh porosity in metal-organic frameworks.* Science, 2010. **329**(5990): p. 424-8.

8. Bernt, S., et al., *Direct covalent post-synthetic chemical modification of Cr-MIL-101 using nitrating acid.* Chem Commun (Camb), 2011. **47**(10): p. 2838-40.

9. Kandiah, M., et al., *Synthesis and Stability of Tagged UiO-66 Zr-MOFs.* Chemistry of Materials, 2010. **22**(24): p. 6632-6640.

10. Küsgens, P., et al., *Characterization of metal-organic frameworks by water adsorption.* Microporous and Mesoporous Materials, 2009. **120**(3): p. 325-330.

11. Low, J.J., et al., *Virtual high throughput screening confirmed experimentally: porous coordination polymer hydration.* J Am Chem Soc, 2009. **131**(43): p. 15834-42.

12. Schoenecker, P.M., et al., *Effect of Water Adsorption on Retention of Structure and Surface Area of Metal–Organic Frameworks.* Industrial & Engineering Chemistry Research, 2012. **51**(18): p. 6513-6519.

13. Cavka, J.H., et al., *A new zirconium inorganic building brick forming metal organic frameworks with exceptional stability.* J Am Chem Soc, 2008. **130**(42): p. 13850-1.

14. Garibay, S.J. and S.M. Cohen, *Isoreticular synthesis and modification of frameworks with the UiO-66 topology.* Chem Commun (Camb), 2010. **46**(41): p. 7700-2.

15. Morris, W., et al., *Synthesis, structure, and metalation of two new highly porous zirconium metal-organic frameworks.* Inorg Chem, 2012. **51**(12): p. 6443-5.

16. Wiersum, A.D., et al., *An evaluation of UiO-66 for gas-based applications.* Chem Asian J, 2011. **6**(12): p. 3270-80.

17. Yang, Q., et al., *Understanding the Thermodynamic and Kinetic Behavior of the CO2/CH4Gas Mixture within the Porous Zirconium Terephthalate UiO-66(Zr): A Joint Experimental and Modeling Approach.* The Journal of Physical Chemistry C, 2011. **115**(28): p. 13768-13774.

18. Yang, Q., et al., *Functionalizing porous zirconium terephthalate UiO-66(Zr) for natural gas upgrading: a computational exploration.* Chem Commun (Camb), 2011. **47**(34): p. 9603-5.

19. Zlotea, C., et al., *Effect of NH2 and CF3 functionalization on the hydrogen sorption properties of MOFs.* Dalton Trans, 2011. **40**(18): p. 4879-81.

20. Deng, H., et al., *Multiple functional groups of varying ratios in metal-organic frameworks.* Science, 2010. **327**(5967): p. 846-50.

21. Millward, A.R. and O.M. Yaghi, *Metal-organic frameworks with exceptionally high capacity for storage of carbon dioxide at room temperature.* J Am Chem Soc, 2005. **127**(51): p. 17998-9.

22. Dybtsev, D.N., H. Chun, and K. Kim, *Rigid and flexible: a highly porous metal-organic framework with unusual guest-dependent dynamic behavior.* Angew Chem Int Ed Engl, 2004. **43**(38): p. 5033-6.

23. Uemura, K., et al., *Syntheses, crystal structures, and water adsorption behaviors of jungle-gym-type porous coordination polymers containing nitro moieties.* Journal of Solid State Chemistry, 2009. **182**(10): p. 2852-2857.

24. Zhao, Y., et al., *Enhancing gas adsorption and separation capacity through ligand functionalization of microporous metal-organic framework structures.* Chemistry, 2011. **17**(18): p. 5101-9.

25. Comotti, A., et al., *Nanochannels of two distinct cross-sections in a porous Al-based coordination polymer.* J Am Chem Soc, 2008. **130**(41): p. 13664-72.

26. Paranthaman, S., F.X. Coudert, and A.H. Fuchs, *Water adsorption in hydrophobic MOF channels.* Phys Chem Chem Phys, 2010. **12**(28): p. 8123-9.

27. Henke, S., et al., *Zinc-1,4-benzenedicarboxylate-bipyridine frameworks – linker functionalization impacts network topology during solvothermal synthesis.* Journal of Materials Chemistry, 2012. **22**(3): p. 909.

28. Walton, K.S. and R.Q. Snurr, *Applicability of the BET method for determining surface areas of microporous metal-organic frameworks.* J Am Chem Soc, 2007. **129**(27): p. 8552-6.

29. Do, D.D., *Adsorption Analysis: Equilibria and Kinetics.* 1998.

30. Saha, D., et al., *Adsorption of CO(2), CH(4), N(2)O, and N(2) on MOF-5, MOF-177, and zeolite 5A.* Environ Sci Technol, 2010. **44**(5): p. 1820-6.

31. Chen, Z.X., et al., *Significantly Enhanced CO2/CH4 Separation Selectivity within a 3D Prototype Metal-Organic Framework Functionalized with OH Groups on Pore Surfaces at Room Temperature.* European Journal of Inorganic Chemistry, 2011. **2011**(14): p. 2227-2231.

32. Couck, S., et al., *An amine-functionalized MIL-53 metal-organic framework with large separation power for CO2 and CH4.* J Am Chem Soc, 2009. **131**(18): p. 6326-7.

33. Stavitski, E., et al., *Complexity behind CO2 capture on NH2-MIL-53(Al).* Langmuir, 2011. **27**(7): p. 3970-6.

34. Karra, J.R. and K.S. Walton, *Molecular Simulations and Experimental Studies of CO2, CO, and N2Adsorption in Metal−Organic Frameworks.* The Journal of Physical Chemistry C, 2010. **114**(37): p. 15735-15740.

35. Kim, M., et al., *Postsynthetic ligand exchange as a route to functionalization of 'inert' metal–organic frameworks.* Chemical Science, 2012. **3**(1): p. 126.

CHAPTER 4

MICRO-BED BREAKTHROUGH STUDY ON A SET OF STABLE MOFS

4.1 Introduction

Separation processes are critical to numerous industrial sectors and recently have become of great interest to the energy sector. Two major separations of great importance are natural gas purification and carbon dioxide capture from flue gas.[1, 2] Current methods of achieving flue gas separation are being implemented on pilot scales but have yet to reach goals in energy efficiency.[3] A separation method which may yield energy efficient processes is adsorption, but no single adsorbent material has yet to be developed which can achieve this goal. The desired properties of such an adsorbent are high selectivity and high capacity for the target gas, stability in the process stream, and a low energy requirement for regeneration.

Hybrid organic-inorganic materials, such as Metal-Organic Frameworks (MOFs), are a promising and highly varied class of materials which have been studied for numerous applications.[4-6] Among these applications are bulk separations,[2] catalysis,[7] and gas storage.[8, 9] Various members of the chemically diverse families of MOFs have record-holding properties with regard to gas storage[10] and surface area.[11] One of the challenges to utilizing MOFs in applications is the lack of stability for many of the best-performing materials.[8, 12] Classification and prediction of MOF stability is the focus of

intense research and a few materials have already been shown to be stable under various aggressive conditions. Among the most stable MOFs are the UiO-66 series of materials and a number MIL materials.[13-17]

Breakthrough experiments are a common and highly relevant method for determining the dynamic adsorption properties of a material.[18-20] Studies have been conducted on the breakthrough performance of MOFs.[21-30] Generally, the results of a breakthrough study are used to determine adsorbent properties, such as adsorption rate, selectivity, and the eponymous breakthrough time. These results are dependent on various features of the adsorbent and system on both micro and macro scales; thus experimental data is often used to validate a model which can be applied to different materials and systems.

The goal of this study is to study a set of stable MOFs with representative pore features in order to extrapolate trends to guide future works. This work entails breakthrough studies of five materials at four different gas compositions under dry conditions. The pore properties studied encompass polar and non-polar functionalities and the effect of pore size on the resulting breakthrough curves. In order to match the small scale of synthesis batches, sample sizes are roughly 100mg. The results indicate that, in the dry gas mixtures, both the amine and di-methyl functionalized UiO-66 materials perform well. Zeolite NaY continues to outperform all of the tested MOFs in these dry conditions. Modeling of the breakthrough indicates that the MOFs perform slightly better than predictions from pure-component isotherms, perhaps indicating more study is needed.

4.2 Experimental Methods and Procedures

4.2.1 *Apparatus*

The apparatus consists of an adsorbent bed packed in ¼" tubing, three MFCs, a four channel controller, a quadrupole MS, heat tape with a PID temperature controller, and gasket-sealed fittings. A schematic is provided in Figure 4.1. Gas flows are controlled remotely by switches on the controller, as the entire apparatus is contained within a fume hood. Further details are provided in Appendix A.2.1.

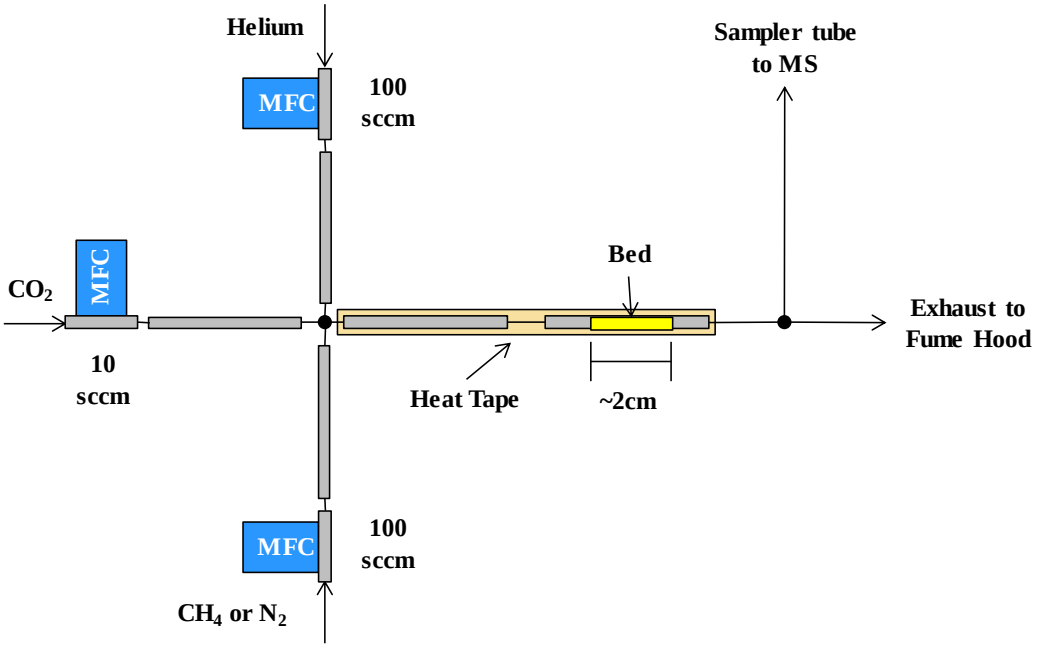

Figure 4.1. Schematic of the instrument used in this study. Flowrate capabilities are presented for MFCs calibrated to N_2.

4.2.2 *Samples*

Standard sample preparation involves packing a bed of powdered adsorbent in a tube formed from two welded VCR® glands. The powder is held in place by a plug of

glass wool at each end, then the bed is gently compacted to prevent sagging. It was noted that an overly compacted bed causes a problematic pressure drop. Once the bed was prepared, the bed section was connected to the apparatus using VCR® gaskets with fritted filters, in order to prevent blowout. No elutriation was noted on these filters afterwards nor had the bed shifted. Sample information is provided in Table 4.1.

Table 4.1. Mass, synthesis method, activation temperature (AT), and surface area for each sample

Sample ID	Mass (mg)	Synthesis	AT (°C)	BET Surface Area (m^2/g)
Zeolite NaY (1)	104.9	Purchased[α]	200	920
Zeolite NaY (2)	99.2	-	200	-
UiO-66	95.3	Reported[31]	200	1230
UiO-66-NH_2 (1)	87.3	Reported[31]	150	1100
UiO-66-NH_2 (2)	88.6	-	150	-
UiO-66-DM (1)	99.5	Reported[32]	200	685
UiO-66-DM (2)	47.6	-	200	775
NH_2-MIL-101(Al)	94.3	Reported[14]	150	1440

α: *HSZ-320NAA*, Tosoh Corp.

Both samples of zeolite NaY and of UiO-66-NH_2 were from the same source batch, while the samples of UiO-66-DM were from different batches. The samples were verified for porosity by N_2 adsorption at 77K and BET surface area was calculated in a relative pressure range of $0.005 < P/P_o < 0.03$.

Sample activation was conducted *in situ.* Temperature control was achieved by wrapping the length of the tubing containing the sample with heat tape and insulation. A thermocouple was placed in contact with the tubing containing the sample and a PID controller was used to maintain temperature. For the duration, helium was passed

through the system at 35 sccm, which was determined to be 25% greater than the rate required to prevent backflow into the system. After 14 hours, temperature was reduced to 25°C and the system was prepared for measurement of the various gas mixtures.

4.2.3 *Measurements*

Standard procedure consists first of priming the turbomolecular vacuum for 15 minutes with the gas mixture to be used in the experiment. This step is necessary as the pump is operating at a faster speed due to the overnight helium purge. Once the experiment gases enter the MS and vacuum system, the vacuum pumping rate decreases, which leads to a decreasing signal from the MS. The priming is used to ensure the first measurement begins at the same state as all subsequent measurements. Once the priming is complete, pure helium is again passed through the bed for 120 minutes in order to reactivate the material from any physisorbed gases. This amount of time was chosen as it is 30 minutes beyond the time when no detectable experiment gases can be measured in the MS.

Experiments were conducted in a similar manner to the priming and purging cycle. The system is initially pure helium flowing at 35 sccm. The MFCs are switched to the experiment flowrates and data is recorded for at least 20 minutes. The cycle was completed by repeating the purge step as previously described. All experiments were conducted twice, consecutively, unless apparent abnormalities indicated further repetitions to be necessary.

Table 4.2. Compositions (%) and flowrates (sccm) of adsorbing species and helium carrier in the various experiments in this study

Experiment		CO_2		N_2		CH_4		He
		%	sccm	%	sccm	%	sccm	sccm
CO_2:N_2	(1)	10	3.5	90	31.5	-	-	0
	(2)	15	5.3	85	29.7	-	-	0
CO_2:CH_4	(1)	50	7.0	-	-	50	7.0	35
	(2)	33	7.0	-	-	67	14.0	35
CO_2	Pure	100	7.0	-	-	-	-	35
CH_4	Pure	-	-	-	-	100	14.0	35

4.2.4 *Dynamic Capacity Calculations*

The primary calculations for this work are based on the time elapsed until 5% of maximum signal is measured at the MS. The obtained data (C/C_o) is normalized to a 0-to-100 scale and the time for $C/C_o = 5$ is obtained by interpolation. As the calibration and experimental curve are very nearly parallel, this approximation is reasonable for determining dynamic capacity.

4.2.5 *Simulations*

A model was built to verify the experimental breakthrough times. First, a multi-component Langmuir isotherm was calculated from Ideal Adsorbed Solution Theory (IAST).[33] Then, the mass and energy balances for the bed were numerically solved with the automatic method for NDSolve in Mathematica. The mass balance for each component is modeled by a convection-diffusion-adsorption equation. The gas velocity and overall mass balance were assumed to be at steady-state and were determined from a linear pressure drop through the bed. Upstream pressure was measured at the MFC for each sample at 35 sccm and the outlet pressure was assumed to be 1 bar. The energy balance was modeled by an equation with convective, conductive, and dispersive terms as

well as a source term based on the heat of adsorption. The effect of temperature on adsorption was modeled via temperature-dependent adsorption affinity parameters for the two gases in the multi-component Langmuir isotherm. In order to model the step change for gas concentration at the inlet, error functions were fit to obtain a match between the calibration data and a variation of the model without an adsorption term. The equations and parameters are provided in detail in Eqs. A.4-A.20 and Tables A.1-A.3 (Appendix A).

Quantitative agreement was not obtained as it is not the primary focus of this work and attempting to match the anomalies of the instrument and subsequent required vacuum corrections would be prohibitive. Also, these discrepancies are most noticeable at the tail of the breakthrough curve, which is not an essential segment of data for this study.

The value of such a model is the ability to determine if unmeasured properties of the bed, such as mass transfer rates and heat dissipation, are controlling the results. The change in gas composition at the bed inlet was modelled by an error function which was matched to the calibration curve for each experimental composition. The model parameters were adjusted to fit the properties and breakthrough time of the zeolite NaY standard. The model was adapted to the MOF samples by replacing the adsorption properties and sample properties while retaining the other parameters.

4.3 Results and Discussion

Four MOFs as well as a commonly used zeolite material were studied. All gas mixtures are dry and were chosen to encompass a range of relevant concentrations for

observing material property trends. The materials chosen are: (1) UiO-66, a well-studied and robust material which can be used as a reference for functionalized UiO-66 materials, (2) UiO-66-NH_2, a material with enhanced adsorption of polar molecules in comparison to UiO-66, (3) UiO-66-DM, a di-methyl functionalized material with good CO_2 uptake and selectivity as well as partial hydrophobic character, (4) NH_2-MIL-101(Al), a stable MOF with large pores, amino functionalities, and open-metal sites, and (5) Zeolite NaY, a well-studied reference material. These pore features were chosen to discern their relative effects on breakthrough time in various CO_2/N_2 and CO_2/CH_4 gas mixtures.

4.3.1 *Dynamic Capacity*

The time required for 5% breakthrough was used to calculate the dynamic capacity for each material and gas composition. For comparison, Ideal Adsorbed Solution Theory (IAST) was applied at the equilibrium concentrations of each gas to predict mixture adsorption and the pure-component isotherms were used for single-component gas adsorption from a helium carrier stream. The dynamic capacities for CO_2 from CO_2/N_2 mixtures and pure CO_2 in a helium carrier stream compared with estimated capacities are shown in Figure 4.2. As the flowrate of N_2 is significantly higher than CO_2, the bed is essentially saturated with N_2 prior to CO_2 adsorption.

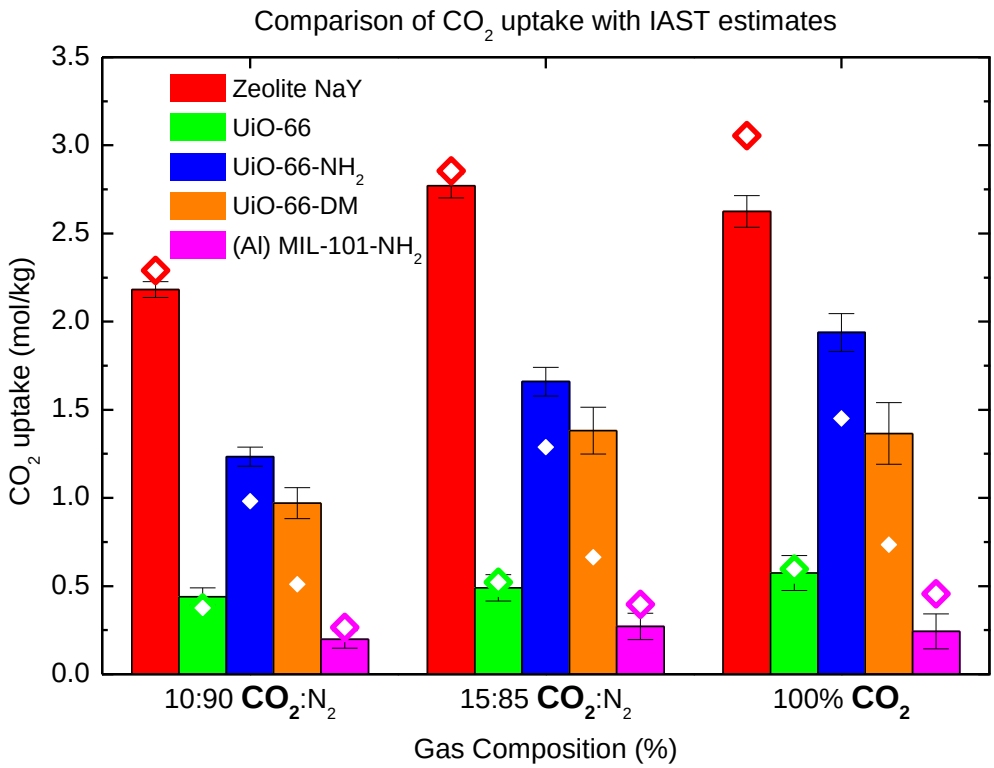

Figure 4.2. Dynamic capacity with IAST estimates and estimated errors for CO_2 from CO_2:N_2 mixtures and for CO_2 in helium carrier. Diamonds are estimated uptake values at the bed conditions based on IAST. Circles are calculated uptakes from pure-component isotherms. Error bars are calculated from sampling rate, mass of adsorbent, and flowrate of gas.

As can be seen in Figure 4.2, the dynamic capacities calculated for CO_2 are in agreement with IAST predictions. The exception is UiO-66-DM, which outperforms predictions by a notable margin. This discrepancy may be attributed to missing linker defects as it has been shown that the adsorption properties of UiO-66 materials can vary while maintaining crystal structure and stability.[34, 35] As has been observed in other members of the UiO-66 series of materials, determination of sample quality via BET surface area and PXRD patterns is unreliable. In fact, the missing-linker defects

commonly found in UiO-66 lead to higher BET surface areas but lower CO_2 adsorption at low pressures.

What can be discerned from these results is that, in the dry conditions tested, zeolite NaY still remains a significantly better option for adsorptive separation of CO_2 from N_2. Among the MOFs tested, UiO-66-NH_2 possesses the longest, weight-normalized breakthrough time for CO_2 and UiO-66-DM is a close second. This is an interesting result in that the non-polar functionalities in UiO-66-DM produce a material that performs similarly to UiO-66-NH_2 at the low partial pressures in these experiments, a results consistent with previous works.[32, 36] Since UiO-66-DM shows a water adsorption isotherm without an apparent step, a feature indicative of pore filling, this material may retain some CO_2 adsorption capacity in the presence of water vapor.

The same calculations were applied to determine dynamic capacities for CO_2 from CO_2:CH_4 mixtures and for pure CH_4 in a helium carrier. The results are presented in Figure 4.3. The measured breakthrough for the CO_2:CH_4 mixtures can be separated into different situations. First, both gas fronts reach the bed simultaneously for the equimolar mixture, with results similar to IAST predictions. Second, methane saturates the bed in the 33%:67% CO_2:CH_4 mixture and shows the effects of adsorbed methane on CO_2 adsorption. A third composition was measured, 67%:33% CO_2:CH_4, but the methane breakthrough curves were too diffuse due to the low flowrate and the 5% breakthrough time was too uncertain to obtain reliable results.

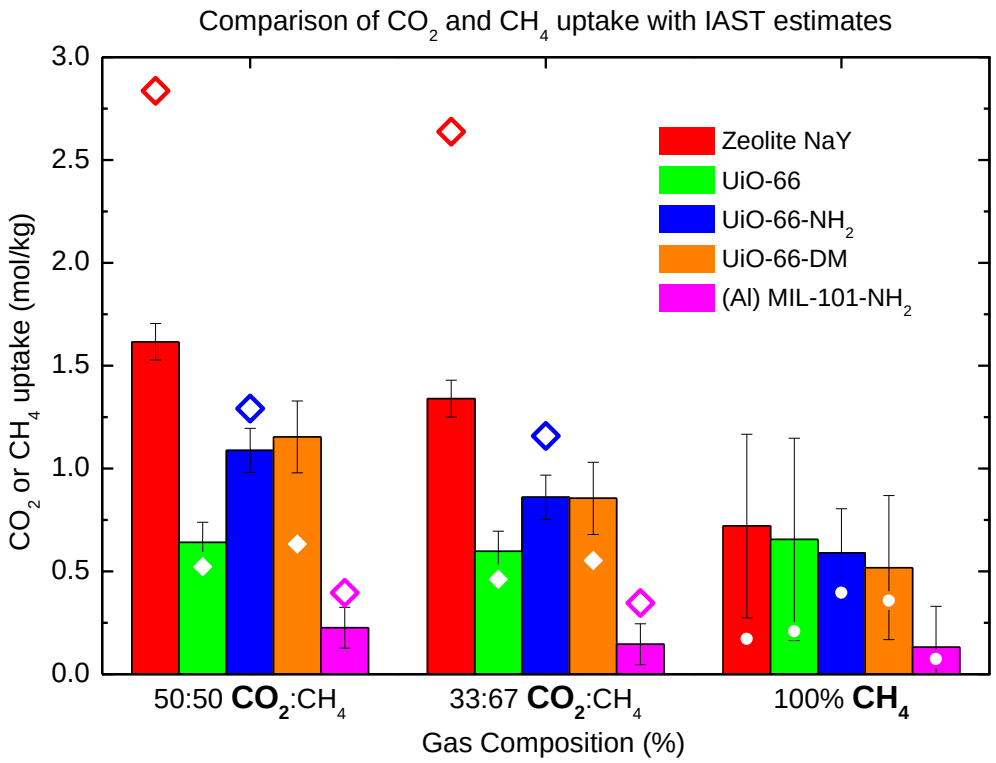

Figure 4.3. Dynamic capacity with IAST estimates and estimated errors for CO_2 from CO_2:CH_4 mixtures and for CH_4 in helium carrier. Diamonds are estimated uptake values at the bed conditions based on IAST. Circles are calculated uptakes from pure-component isotherms. Error bars are calculated from sampling rate, mass of adsorbent, and flowrate of gas.

For CO_2 dynamic capacity, zeolite NaY and UiO-66-NH_2 do not perform as well as expected from IAST predictions but the resulting calculated selectivities for zeolite NaY are in good agreement with previously published results.[37] With regard to the four MOFs tested, the results clearly show UiO-66-NH_2 and UiO-66-DM outperforming unfunctionalized UiO-66 and large pore NH_2-MIL-101(Al). The CH_4 capacities for all five materials are close to expectations and the trend indicates that the adsorption is more well predicted by pore size than pore functionality.

The CO_2 dynamic capacity of UiO-66-NH_2 and UiO-66-DM is nearly identical, a result which does not exactly fit the conventional thinking of "like-adsorbs-like." When compared to the unfunctionalized parent material, the expectation would be for a small, polar functional group to enhance selectivity for CO_2 over CH_4, whereas the non-polar methyl functional groups would reduce selectivity, but the opposite is observed. The result measured here agrees with results found elsewhere that methyl functionalities can significantly enhance CO_2 selectivity over other gases when the pore structure is properly shaped.[36] The methyl groups enhance the interactions of a CO_2 molecule at corner adsorption sites by providing a partial positive charge for electrostatic interactions with the oxygen atoms of CO_2. In situations where such corner adsorption sites are not accessible to CO_2, the methyl groups would likely not provide any significant benefit or even prove to be detrimental to selectivity for CO_2 due to the increased dispersive interactions with all gas molecules.

Finally, the dynamic capacities were calculated in the same manner as previously used for N_2 from CO_2:N_2 mixtures and for CH_4 from CO_2:CH_4 mixtures are presented in Figure 4.4. As the breakthrough time for N_2 is very fast, statistically significant dynamic capacity could not be used for selectivity calculations.

As can be seen in the plots, the bed size and instrument sensitivity were not capable of accurately discerning the dynamic capacity of N_2, thus no trends can be revealed. The resulting CH_4 dynamic capacities are well above IAST predictions, as reasonable result for a dynamic adsorption experiment. When the capacities were used for selectivity estimates, the results for the zeolite standard are similar to published values.[37] This indicates the measurements are more likely accurate than IAST

predictions under dynamic conditions. The trends indicate that a material possessing small pore size is a more dominant factor for these non-polar adsorbates than pore functionality.

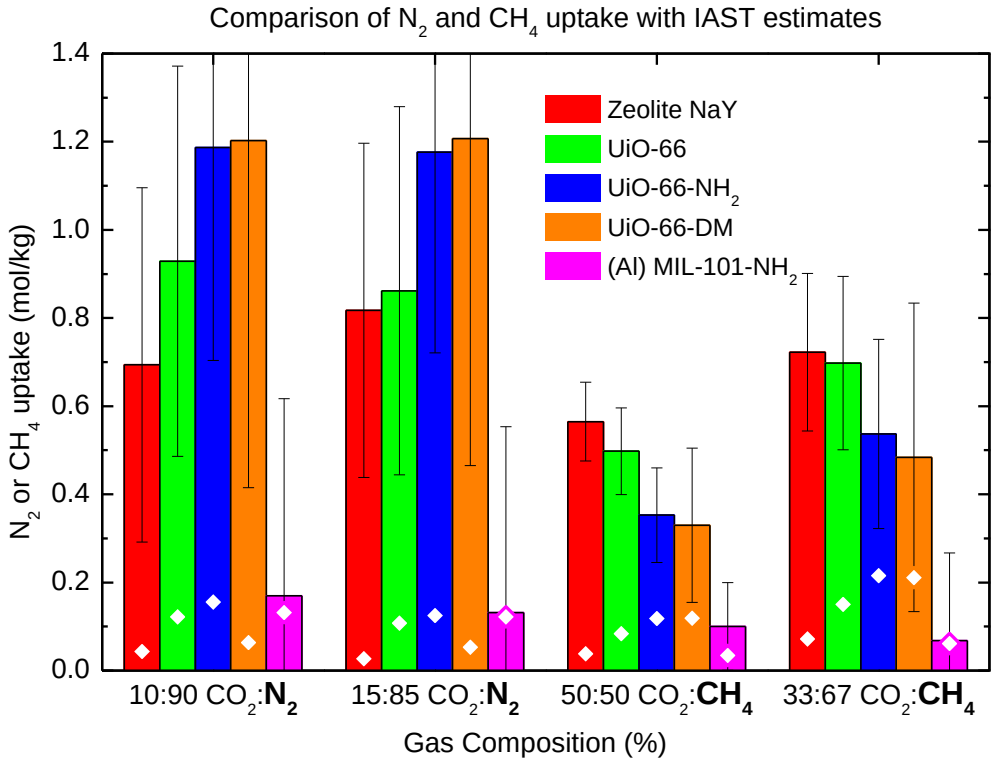

Figure 4.4. Dynamic capacity with IAST estimates and estimated errors for CH_4 from CO_2:CH_4 mixtures and for N_2 from CO_2:N_2 mixtures. Diamonds are estimated uptake values at the bed conditions based on IAST. Error bars are calculated from rate of measurement, mass of adsorbent bed, and flowrate of gas.

4.3.2 *Selectivity*

Selectivity for each sample and gas composition was calculated according to Eq. 4.1. The results of the calculations are shown in Table 4.3. Due to uncertainty with the rapid breakthrough time of N_2 in the CO_2:N_2 experiments, selectivity values cannot be

calculated from the measurements. For the CO_2:CH_4 mixtures, IAST selectivity predictions exceed calculated values for each sample. This is expected as dynamic selectivity will be less than predictions at equilibrium due to diffusion limitations. Additionally, CO_2 does not behave ideally in the adsorbed phase, thus IAST calculations are expected to be slightly inaccurate for mixtures with CO_2.[38]

$$S_{1,2} = \frac{x_1/y_1}{x_2/y_2} \tag{4.1}$$

Table 4.3. Selectivity ($S_{1,2}$) calculated from dynamic capacity for CO_2 (1) over CH_4 (2) compared with IAST predictions

$S_{1,2}$	CO_2:CH_4	Zeolite NaY	UiO-66	UiO-66-NH_2	UiO-66-DM	NH_2-MIL-101(Al)
IAST	50:50	74.6	6.2	10.9	5.3	11.5
	33:67	74.3	6.2	10.9	5.3	11.5
Expt.	50:50	2.9 (3.7)[37]	1.3	3.1	3.5	2.3
	33:67	3.8 (3.7)[37]	1.7	3.3	3.6	4.3

UiO-66-DM shows the highest selectivity and is within error of the IAST value. This sample had shown better uptake of CO_2 and CH_4 than previous reports, therefore this unexpected result may not be erroneous but instead warrant further study. Each of the samples were predicted to have selectivity relatively invariant of the mixture concentrations tested here, but showed a higher CO_2 selectivity as its composition fraction decreased. This can be attributed to the diffusion rate of the two gases, where CH_4 will break through the bed before significant adsorption occurs, leading the denominator in Eq. 4.1 to be smaller.

4.3.3 *Simulations*

A breakthrough model was built as previously described. The bed parameters were matched to the known properties of zeolite NaY, which was used as a standard and are given in Table A.21 through Table A.23 (Appendix A). Mass transfer and heat dissipation were determined to be fast and a minor factor for the breakthrough times and curve shapes. The model predicts significant sharpening for some samples, but only slight sharpening is observed in the experiments. A possible reason for a lack of observed sharpening is inherent to the instrument and compounded by the corrections applied to the data. The model could not match both breakthrough times and curve shapes.

All of the simulated breakthrough curves with corresponding experimental and calibration data can be found in Figure A.19. through Figure A.23. (Appendix A). In Figure 4.5, the results of the 15:85 CO_2:N_2 breakthrough simulations are shown with corresponding calibrations and experimental data.

When this model was translated to the MOF samples, the predicted breakthrough times are slightly earlier than experimental values. Perhaps the reason for this discrepancy is that an isotherm model which was fit to data over a wide pressure range does not predict enough gas uptake at the low partial pressures of this experiment. Alternatively, the UiO-66 series of MOFs may have a stronger adsorption affinity at these low partial pressures that wasn't directly observed in pure-component measurements and the subsequently fit isotherms.

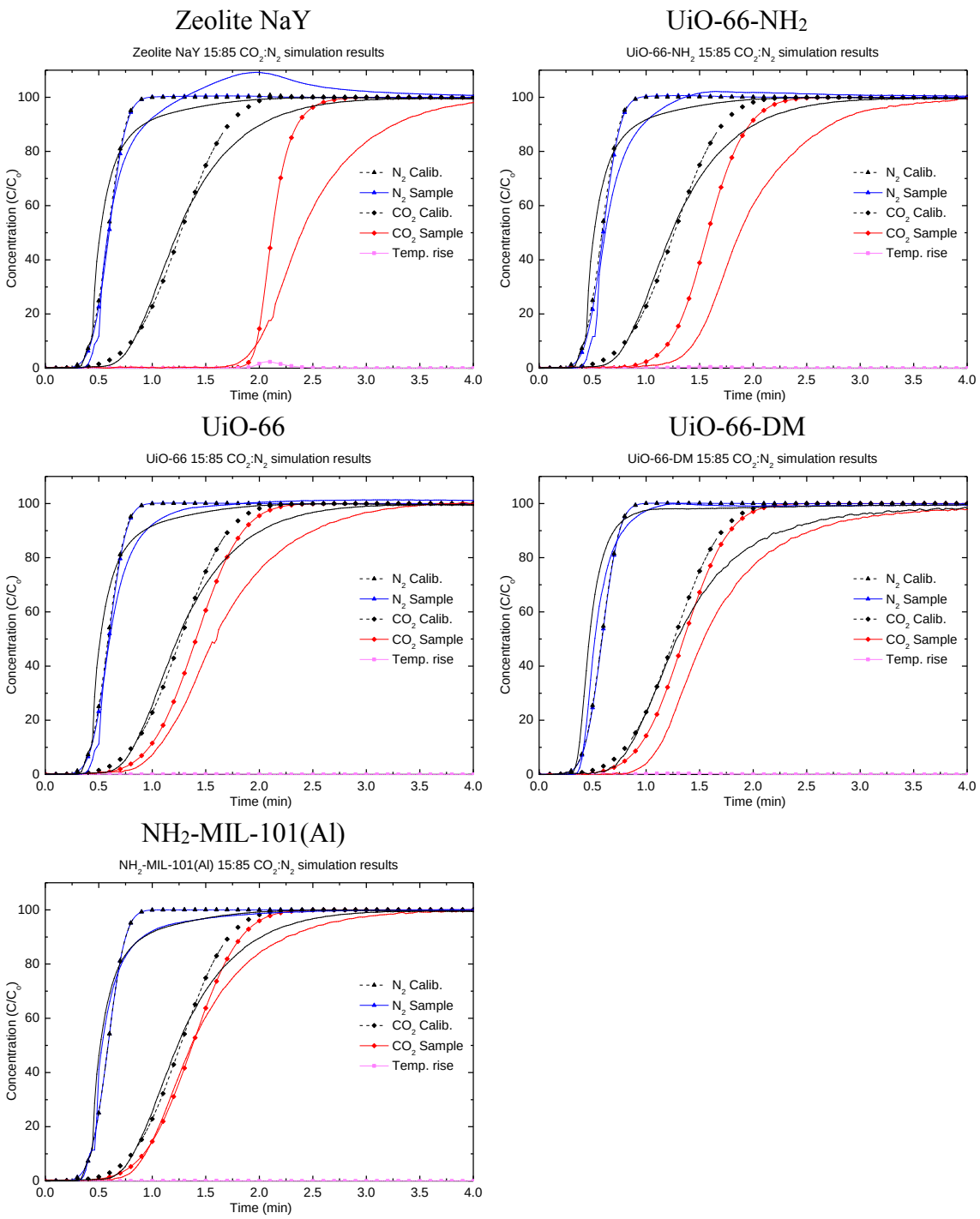

Figure 4.5. Lines with symbols are simulation results, lines without symbols are experimental results. Calibration from experiment and simulation for each gas is in black and is immediately prior to the corresponding adsorption result. Temperature rise (K) uses the same axis values.

4.4 Conclusions and Recommendations

A micro-scale breakthrough experiment on a series of representative MOFs with dry CO_2:CH_4 and CO_2:N_2 mixtures was conducted. The results indicate that, among the stable MOFs tested here, UiO-66-NH_2 performs the best for gas separation. UiO-66-DM, a partially hydrophobic material, performs nearly as well and may be a good candidate for further study under humid conditions. Although NH_2-MIL-101(Al) possesses open-metal sites and amine functionalities, the large pore size and low density of adsorption sites significantly reduce its separation capability via reduced adsorption capacity and selectivity.

The results were used to calculate dynamic selectivities, which were significantly lower than the predicted values from IAST calculations but were in agreement with reported values for zeolite NaY. This indicates that values and trends from IAST predictions are not directly translatable to dynamic experiments. The results were also compared to a simple breakthrough simulation, which matched qualitatively. The simulation maintained good agreement across all samples, but predicted shorter breakthrough times than was experimentally observed for the two best performing MOF samples.

This type of experiment is promising, particularly due to the small sample size. Addition of a humidification system and a thermocouple in contact with the bed will improve the relevance of the results to real-world applications. Also, analysis of desorption data can provide more information about the equally important regeneration step of adsorption cycles.

4.5 References

1. Sumida, K., et al., *Carbon Dioxide Capture in Metal-Organic Frameworks.* Chemical Reviews, 2012. **112**(2): p. 724-781.

2. Li, J.R., J. Sculley, and H.C. Zhou, *Metal-organic frameworks for separations.* Chemical reviews, 2012. **112**(2): p. 869-932.

3. Boot-Handford, M.E., et al., *Carbon capture and storage update.* Energy & Environmental Science, 2014. **7**(1): p. 130-189.

4. Ferey, G., *Hybrid porous solids: past, present, future.* Chemical Society reviews, 2008. **37**(1): p. 191-214.

5. Czaja, A.U., N. Trukhan, and U. Muller, *Industrial applications of metal-organic frameworks.* Chemical Society Reviews, 2009. **38**(5): p. 1284-93.

6. Meek, S.T., J.A. Greathouse, and M.D. Allendorf, *Metal-organic frameworks: a rapidly growing class of versatile nanoporous materials.* Advanced materials, 2011. **23**(2): p. 249-67.

7. Lee, J., et al., *Metal-organic framework materials as catalysts.* Chemical Society reviews, 2009. **38**(5): p. 1450-9.

8. Ding, L. and A.O. Yazaydin, *Hydrogen and methane storage in ultrahigh surface area Metal–Organic Frameworks.* Microporous and Mesoporous Materials, 2013. **182**: p. 185-190.

9. Sculley, J., D. Yuan, and H.-C. Zhou, *The current status of hydrogen storage in metal–organic frameworks—updated.* Energy & Environmental Science, 2011. **4**(8): p. 2721.

10. Peng, Y., et al., *Methane storage in metal-organic frameworks: current records, surprise findings, and challenges.* Journal of the American Chemical Society, 2013. **135**(32): p. 11887-94.

11. Farha, O.K., et al., *Metal-organic framework materials with ultrahigh surface areas: is the sky the limit?* Journal of the American Chemical Society, 2012. **134**(36): p. 15016-21.

12. Kaye, S.S., et al., *Impact of preparation and handling on the hydrogen storage properties of Zn4O(1,4-benzenedicarboxylate)3 (MOF-5).* Journal of the American Chemical Society, 2007. **129**(46): p. 14176-7.

13. Cavka, J.H., et al., *A new zirconium inorganic building brick forming metal organic frameworks with exceptional stability.* Journal of the American Chemical Society, 2008. **130**(42): p. 13850-1.

14. Serra-Crespo, P., et al., *Synthesis and Characterization of an Amino Functionalized MIL-101(Al): Separation and Catalytic Properties.* Chemistry of Materials, 2011. **23**(10): p. 2565-2572.

15. Qian, X.K., et al., *Structure stability of metal-organic framework MIL-53 (Al) in aqueous solutions.* International Journal of Hydrogen Energy, 2013. **38**(36): p. 16710-16715.

16. DeCoste, J.B., et al., *Stability and degradation mechanisms of metal–organic frameworks containing the Zr6O4(OH)4 secondary building unit.* Journal of Materials Chemistry A, 2013. **1**(18): p. 5642.

17. Schoenecker, P.M., et al., *Effect of Water Adsorption on Retention of Structure and Surface Area of Metal-Organic Frameworks.* Industrial & Engineering Chemistry Research, 2012. **51**(18): p. 6513-6519.

18. Bollini, P., et al., *Dynamics of CO2 Adsorption on Amine Adsorbents. 1. Impact of Heat Effects.* Industrial & Engineering Chemistry Research, 2012. **51**(46): p. 15145-15152.

19. Bollini, P., et al., *Dynamics of CO2 Adsorption on Amine Adsorbents. 2. Insights Into Adsorbent Design.* Industrial & Engineering Chemistry Research, 2012. **51**(46): p. 15153-15162.

20. Krishna, R., *Adsorptive separation of CO2/CH4/CO gas mixtures at high pressures.* Microporous and Mesoporous Materials, 2012. **156**: p. 217-223.

21. Casas, N., et al., *MOF and UiO-67/MCM-41 adsorbents for pre-combustion CO2 capture by PSA: Breakthrough experiments and process design.* Separation and Purification Technology, 2013. **112**: p. 34-48.

22. Hamon, L., et al., *Co-adsorption and separation of CO2-CH4 mixtures in the highly flexible MIL-53(Cr) MOF.* Journal of the American Chemical Society, 2009. **131**(47): p. 17490-9.

23. Hamon, L., et al., *Separation of CO2-CH4 mixtures in the mesoporous MIL-100(Cr) MOF: experimental and modelling approaches.* Dalton transactions, 2012. **41**(14): p. 4052-9.

24. Grant Glover, T., et al., *MOF-74 building unit has a direct impact on toxic gas adsorption.* Chemical Engineering Science, 2011. **66**(2): p. 163-170.

25. Peralta, D., et al., *Comparison of the behavior of metal-organic frameworks and zeolites for hydrocarbon separations.* Journal of the American Chemical Society, 2012. **134**(19): p. 8115-26.

26. Bastin, L., et al., *A Microporous Metal-Organic Framework for Separation of CO2/N2 and CO2/CH4 by Fixed-Bed Adsorption.* Journal of Physical Chemistry C, 2008. **112**(5): p. 1575-1581.

27. Herm, Z.R., E.D. Bloch, and J.R. Long, *Hydrocarbon Separations in Metal–Organic Frameworks.* Chemistry of Materials, 2014. **26**(1): p. 323-338.

28. Pirngruber, G.D., et al., *A method for screening the potential of MOFs as CO2 adsorbents in pressure swing adsorption processes.* ChemSusChem, 2012. **5**(4): p. 762-76.

29. Hamon, L., E. Jolimaitre, and G.D. Pirngruber, *CO2 and CH4 Separation by Adsorption Using Cu-BTC Metal-Organic Framework.* Industrial & Engineering Chemistry Research, 2010. **49**(16): p. 7497-7503.

30. Peterson, G.W., et al., *Engineering UiO-66-NH2 for Toxic Gas Removal.* Industrial & Engineering Chemistry Research, 2014. **53**(2): p. 701-707.

31. Cmarik, G.E., et al., *Tuning the adsorption properties of UiO-66 via ligand functionalization.* Langmuir, 2012. **28**(44): p. 15606-13.

32. Jasuja, H. and K.S. Walton, *Experimental Study of CO2, CH4, and Water Vapor Adsorption on a Dimethyl-Functionalized UiO-66 Framework.* Journal of Physical Chemistry C, 2013. **117**(14): p. 7062-7068.

33. Myers, A.L. and J.M. Prausnitz, *Thermodynamics of Mixed-Gas Adsorption.* Aiche Journal, 1965. **11**(1): p. 121-+.

34. Wu, H., et al., *Unusual and highly tunable missing-linker defects in zirconium metal-organic framework UiO-66 and their important effects on gas adsorption.* Journal of the American Chemical Society, 2013. **135**(28): p. 10525-32.

35. Valenzano, L., et al., *Disclosing the Complex Structure of UiO-66 Metal Organic Framework: A Synergic Combination of Experiment and Theory.* Chemistry of Materials, 2011. **23**(7): p. 1700-1718.

36. Burtch, N.C., et al., *Molecular-level Insight into Unusual Low Pressure CO2 Affinity in Pillared Metal-Organic Frameworks.* Journal of the American Chemical Society, 2013. **135**(19): p. 7172-7180.

37. Wiersum, A.D., et al., *An adsorbent performance indicator as a first step evaluation of novel sorbents for gas separations: application to metal-organic frameworks.* Langmuir, 2013. **29**(10): p. 3301-9.

38. Cessford, N.F., N.A. Seaton, and T. Duren, *Evaluation of Ideal Adsorbed Solution Theory as a Tool for the Design of Metal-Organic Framework Materials.* Industrial & Engineering Chemistry Research, 2012. **51**(13): p. 4911-4921.

CHAPTER 5

DESIGN OF OPTIMAL MOFS FOR CARBON CAPTURE

5.1 Introduction

Energy efficient separation of carbon dioxide from flue gas and natural gas is a major research and engineering challenge facing today's society.[1-8] Carbon dioxide capture from flue gas is the focus of intense research due to its long-term potential to disrupt environmental and economic activities via global warming.[9] Additionally, low quality natural gas reservoirs could become economically viable with better gas separation systems,[10] thus providing fuel for power systems with inherently lower carbon dioxide emissions than coal. Ultimately, the advancement of carbon dioxide separation technology can reduce the severity of the major anthropogenic contributor to global warming and improve the feasibility of a long-term transition to clean energy sources.

Economically viable carbon dioxide capture from large point sources, particularly coal fired power plants, is a major challenge facing researchers and engineers.[1, 2, 11] The key factors that define this type of system are the low concentration of CO_2, large volumetric flowrate, and presence of several contaminants, most notably water vapor.[12] The current method to perform this separation is based on an absorption and stripping process with aqueous amine solutions, a mature technology often used in natural gas sweetening.[13-15] The energy intensive process would increase the cost of electricity by 80% which necessitates improved technology.[16] An alternative separation method with the potential for a smaller energy penalty is adsorption.

Adsorption technology is a well-established and rapidly growing field for both engineers and material scientists.[3] Adsorption development consists of two closely linked components, process optimization and material design. On the process side, vacuum and/or temperature swing adsorption cycles would be best suited for retrofitting to existing power plants.[17] Currently, the adsorption cycle is optimized to best suit the selected material, the most important of which are activated carbons, silicas, and zeolites. In order to capture carbon dioxide with a smaller energy penalty, materials with optimally tuned adsorbent properties are needed. A major challenge facing optimal adsorbent design is retention of performance and selectivity in the presence of water vapor. Metal-Organic Frameworks (MOFs), a relatively new class of materials, show great promise as tunable adsorbents for carbon dioxide capture.[1]

The goal of this perspective is to provide a summary and outlook on the design of MOFs as optimal carbon dioxide adsorbents. Particular attention will be given to the conditions for vacuum swing adsorption as it may be the most energy efficient method. Other methods for separation of humid flue gas are well covered by previous works[18, 19] or better suited to other materials.[17] This work will first briefly review the adsorption mechanism, the relevant gas molecules, and the properties of flue gas. Next, a review of current adsorbents and the important factors for developing an optimal adsorbent will be covered. These factors are adsorbent utilization, cost, stability, and optimal isotherm shape. By considering the Toth equation, the pore features which produce an optimal isotherm will be described. Combining these factors, a number of promising MOF materials will be discussed for their potential. Finally, an outlook on the optimization of MOFs for carbon capture will be provided.

5.2 Background: Adsorption

Adsorption is the process of fluid molecules reversibly depositing on or reacting with a solid surface.[20-22] The adsorption process is energetically favorable, which results in higher concentrations of the molecules of the fluid near the solid surface. Gas adsorption can be classified into two primary modes: chemical and physical. Chemical adsorption (chemisorption) is characterized by the formation of chemical bonds between the adsorbate molecule and surface functionalities on the adsorbent. Physical adsorption (physisorption) is characterized by electrostatic and dispersive interactions between the adsorbate molecule and the adsorbent surface.

Chemical adsorbents capture gas molecules primarily by reversible reactions, such as the reaction between acidic carbon dioxide molecules and basic amines or basic minerals. Capture of carbon dioxide with chemisorbents is typically highly selective and highly exothermic with high total uptake. The downside is that these materials often require significant energy to regenerate and lose capacity upon recycling. Supported-amine sorbents are viable materials for post-combustion capture and air capture, while mineral sorbents are usually considered for pre-combustion or chemical looping systems.[2, 6]

Physical adsorbents capture gas molecules based on favorable electrostatic and dispersive forces at the pore surface. Higher specific surface area typically correlates to higher total adsorbed amounts due to more available adsorption sites per mass of adsorbent, assuming similar adsorbent density and pore surface interactions. Stronger adsorption sites can be generated by a combination of polar functional groups, electrostatic charges, and pore shape, which leads to greater adsorption at low pressures.

Zeolites, and activated carbons are currently the most important physisorbents for gas separations with MOFs recently becoming available on a commercial scale.[23]

Selective adsorption is possible due to differing interaction potentials between the pore surface and different gases. High selectivity and high uptake are the most desired properties of a physisorbent, but are often found to vary inversely to each other due to physical limitations. The major methods for improving physisorbents are increase the interaction potentials via surface functionalization or increase the specific surface areas in order to provide more adsorption sites. Alternatively, systems can operate in a kinetic regime where differences in the diffusion rates of each gas into the pores allow for dynamic separation, a situation often encountered with molecular sieves. Kinetic separations are difficult to successfully apply to carbon capture due to limited material utilization at high flowrates.

The major adsorbing components in flue gas are water vapor, N_2, and CO_2, whereas in natural gas the major components are CH_4, N_2, and CO_2. The most relevant properties of these and other gases are listed in Table 5.1. Physisorbed molecules are well-known to have approximately liquid phase properties,[24] thus at temperatures near and above the critical temperature, molecules act more ideal in the adsorbed phase. This allows for fairly accurate predictions for equilibrium mixture adsorption via Ideal Adsorbed Solution Theory (IAST),[25] a computationally easy method. IAST is not particularly accurate for dynamic adsorption and predictions begin to deviate with more non-ideal adsorbates. Kinetic diameter describes the approximate pore size through which gas molecules can readily diffuse, an essential value for molecular sieves. The

other values describe how much pore space an adsorbed molecule occupies as well as the relative strength of dispersive and polar interactions.

Some of these molecules can interact further with adsorption sites to irreversibly adsorb via chemical reactions, particularly SO_x and NO_x, but this has been previously reviewed.[6] SO_x, NO_x, and CO are currently scrubbed from flue gas by either wet or dry methods which affect downstream water content.[12] The direct impact of these contaminants on CO_2 adsorption has been reported in several works.[26-29] A general ranking for gas molecule adsorption strength at coordinatively-unsaturated sites (CUS) was predicted to be $NH_3>H_2O>H_2S>SO_2>CO\sim CO_2\sim NO_x> N_2>O_2$ with occasional exceptions.[29, 30]

Carbon dioxide is a linear molecule with no dipole moment but a significant quadrupole moment, alternating partial positive and negative charges, and unsaturated bonds. The alternating partial charges have been found to lead to either attractive or repulsive interactions with pore functionalities depending on the accessible orientations[32] and can be exploited by periodic pore functionalities for improved adsorption, as suggested by Kitagawa and Matsuda.[33] The strongest physical adsorption interactions have been found to be between the free orbitals of the oxygen atoms and exposed metal ions.[34] CO_2 can form carbonate and bicarbonate species with exposed metal ions, especially in the presence of water; a process which is not reversible under mild regeneration conditions.

Table 5.1. Gas molecule properties for important components in adsorptive separations.[31]

Gas	Kinetic diameter (Å)	Dipole Moment (10^{-19} esu^{-1} cm^{-1})	Quadrupole moment (10^{-27} esu^{-1} cm^{-1})	Polarizability (10^{-25} cm^{-3})	Configuration	Critical Temperature (K)
CO_2	3.30[31]	0	43.0	29.1	Linear	304
N_2	3.64[31]	0	15.2	17.4	Linear	126
H_2O	2.64[31]	18.5	-	14.5	Bent	647
CH_4	3.76[31]	0	-	25.9	Tetrahedral	191
O_2	3.47	0	3.9	15.8	Linear	155
CO	3.69	1.10	25.0	19.5	Linear	133
NO_2	N/A$^{\alpha}$	3.16	-	30.2	Bent	431
NO	3.49	1.59	-	17.0	Linear	180
SO_2	4.11	16.3	-	37.2	Bent	431
H_2S	3.62	9.78	-	37.8	Bent	373

α: Not applicable due to chemical equilibrium with N_2O_4.

Water is the major competitive adsorbate in flue gas separations. It a small molecule with a strong dipole moment and interacts strongly with exposed metal ions, typically displacing other adsorbates. Water molecules can form clusters via hydrogen bonds, leading to pore condensation and exclusion of other adsorbates in many situations. Hydrophilic adsorbents are generally those which have Type 1 or Type 2 isotherms for water vapor and the pore surfaces have exposed cations or polar functionalities which can form hydrogen bonds with a water molecule. Adsorbents with pore surfaces devoid of those types of sites are generally hydrophobic and typically show "s-shaped" Type 5 isotherms.

Methane and nitrogen adsorb weakly, adsorbed phase interactions are nearly ideal, and mixture selectivity is well described by IAST.[25] Due to larger kinetic

diameters, either molecule can be excluded from molecular sieves during CO_2 separations.

For CO_2 capture from flue gas, it is generally assumed that there are SO_x and NO_x pretreatment steps, which increase the water content of the stream, and pressure is supplied only by the furnace blowers. Another pretreatment step which could beneficially impact adsorption capture is direct water cooling. Hasan et al. stated[35] "the advantage is that this reduces the moisture content to 5.5%, which is the composition of H_2O in a saturated flue gas at 35 °C, irrespective of the initial moisture content." Simultaneously reducing the total quantity of water vapor and the temperature can greatly enhance the overall efficiency of a packed bed for any kind of adsorbent. Table 5.2 provides the ranges of operating parameters of most interest to the various adsorption cycles currently in use. The composition and conditions for flue gas separation are listed in Table 5.3.

Table 5.2. Operating Temperatures and Pressures for proposed carbon capture adsorption cycles

Method	TSA	PSA	VSA	VPSA
Adsorption Pressure Range (atm)	1.0-1.1	>5	1.0-1.2	>2
Partial Pressure CO_2 (atm)	0.15-0.20	>0.5	0.15-0.20	>0.3
Desorption Pressure Range (atm)	1.0-1.1	1.0-1.1	<0.05	<0.05
Adsorption Temperature (°C)	45[a]-80[b]	35[c]-80[b]	35[c]-80[b]	35[c]-80[b]
Desorption Temperature (°C)	110 [a]-175[d]	40-55[e]	40-55[e]	40-55[e]

a: Plant scale test[36]
b: After flue gas treatment[12]
c: After direct water cooling[35]
d: Max temperature for supported amine sorbent[17]
e: Assumes adiabatic temperature change of up to 20°C

Table 5.3. Typical flue gas composition[12]

Component	Coal[a]	Coal[b]
N_2	80%	80%
CO_2	14.5%	14.5%
H_2O	5-14%	5.5% (saturation)
SO_x	<70 ppm	<70 ppm
NO_x	<100 ppm	<100 ppm
Pressure (bar)	1	1
CO_2 Partial Pressure (bar)	0.15	0.15
Temperature (°C)	40-80	35
a: After NO_x, SO_x removal, varies with dry or wet methods. b: After NO_x, SO_x removal and direct water cooling.[35]		

As can be seen in Table 5.3, the pressure and temperature ranges are markedly different for the various choices of adsorption cycles. When the system pressure and/or temperature swings, the equilibrium between adsorbed and gas phases shifts to compensate. This leads to the aptly named cycles: pressure swing adsorption (PSA) and temperature swing adsorption (TSA). Vacuum swing adsorption (VSA) is a common variation of PSA. Also, hybrid variations of these cycles exist. Control of the pressure and temperature swings allows for controlled capture and release of target gas molecules. The goal of an implemented adsorption cycle is to capture 90% of the CO_2 from flue gas[37] and generate a product stream at 95% purity for pipeline transport.[38]

For the properties of flue gas, TSA and VSA are often considered the best choices, as compression of the large flowrates required for PSA would be uneconomical. TSA can utilize waste heat for operation leading to lower energy costs but requires a hot, diluting purge gas to drive the desorption process.[39, 40] VSA is competitive due to high recovery and the high purity of the extract product achievable at large scales as well as doubling as a dehydration process.[41] The main drawbacks to standard VSA systems are

high energy cost of mechanical vacuum pumps, poor thermal control in packed beds, and complex predictive modeling.[42] The major challenge remains sufficient adsorption and desorption of CO_2 from the hot, dilute, large volumetric flow in the presence of water vapor. The detrimental impact of water vapor on PSA/VSA performance has only been studied experimentally in a few instances, with the results indicating a reduced bed capacity and higher pressures during evacuation.[43-46] Optimized adsorbents for humid VSA systems will be the primary focus for the remainder of this work as the simplicity and high product purity are more easily achieved at large scales.[41]

5.3 Factors for Adsorbent Design

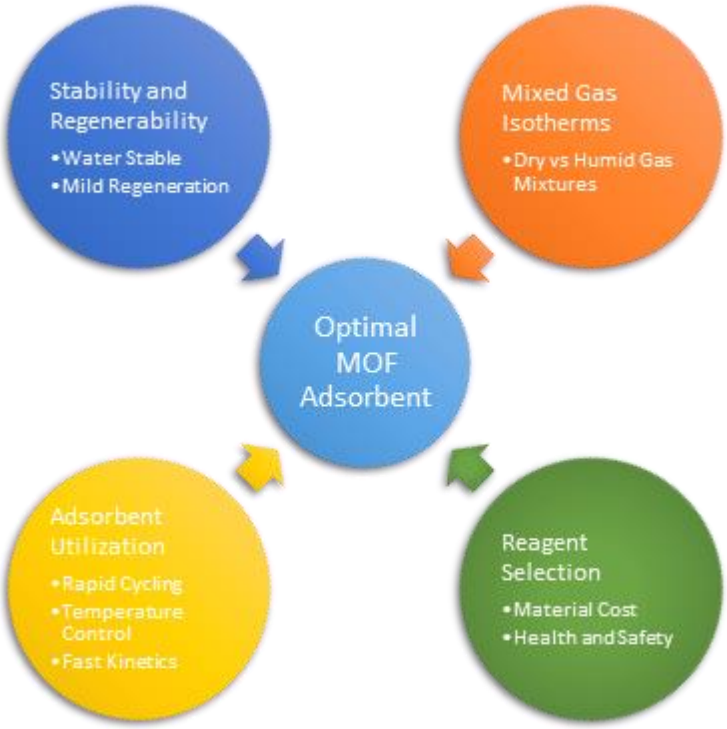

Figure 5.1. Outline of factors for optimal adsorbent design.

5.3.1 *Adsorbent Utilization and Adsorption Rate*

Two important aspects of adsorbent optimization are utilization and adsorption rate. Pelletized sorbents in packed beds operating in VSA and/or TSA cycles are the industry standard for adsorptive separation systems due to simplicity and reliability. Design of a packed bed involves optimization of pressure drop as a function of feed pressure, flowrate, and particle size. Particle size is inversely related to adsorption rate, a

standard mass transport problem. In order to maintain fast adsorption without excessive pressure drops in the bed, engineered sorbents need to be considered.

Engineered adsorbents, such as hollow fiber sorbents[47] or monolithic supports,[48] can allow for better thermal control as well as enable effective rapid adsorption cycling due to thinner diffusion lengths and lower pressure drops.[49] Rezaei and Webley proposed an optimal adsorbent pore geometry for fast-cycle VSA systems to have 45% mesopores and as many adsorbate-sized micropores as possible.[50] This arrangement would maximize mass transfer rates for the short timescales of rapid PSA (RPSA) cycles. RPSA cycles would reduce the required amount of adsorbent by increasing the throughput of a given bed when compared to standard VSA cycles which require significant periods of time for equilibration.

Improved thermal control allows for better adsorbent utilization in structured adsorbents[51] and ultimately reduced operating cost.[52] A review by Rezaei and Webley covers the most important benefits and drawbacks of structured adsorbents over packed beds.[53] MOFs are especially suited for supported adsorbents because crystals can be grown with high density directly on various support materials.[54] Since the crystals are grown directly on the material, attrition and flaking problems may be reduced in comparison to applying adsorbent as a coating. Additionally, rapid adsorption cycles can be more fully utilized using structured adsorbents.[55]

5.3.2 *Stability and Regenerability*

Coordination chemistry is essential to understanding MOF stability and possible structures. One of the more apt pseudonyms for MOFs is Porous Coordination Polymers (PCPs). The review by Cook et al. provides an excellent foundation for understanding

coordination chemistry in MOFs.[56] Some of the key concepts are ligand exchange rates, bond energies, connectivity, and coordination modes.[57] Ligand exchange rates indicate the kinetic stability of metal-ligand bonds in the presence of other molecules, especially water.[58] This shows that Al^{+3} and Cr^{+3} are among the most stable choices outside of noble metals. Bond energy comparisons can indicate whether the metal-ligand bonds and/or the metal SBU will be thermodynamically stable to substitution reactions over relatively long time periods, such as is the case for ZIF stability to water. Higher connectivity and/or coordination numbers for an SBU are also correlated to higher stability due to steric effects.[59]

Thermodynamic stability is an important consideration for long term stability if the material is immersed in a fluid for extended periods of time or at high temperature. Low et al. tested the stability of several representative MOFs on exposure to steam at various temperatures and concentrations, showing that even highly stable MOFs are susceptible to hydrolysis.[60] In this same study, a simple comparison between the energy of the MOF and decomposition products has shown most MOFs to be thermodynamically unstable. Schoenecker et al. tested the equilibrium adsorption of water for several representative MOFs and showed a loss of porosity and structure in materials previously noted to be stable.[59] In certain instances, a MOF can be stable to two separate components but degrade in the mixture, such as was shown with water and air for (Mg)MOF-74.[60-63] It has been shown that post-synthetic modification of the SBU can significantly improve stability, as was shown with Ni-substituted MOF-5[64] and (Mg)MOF-74.[65] Further study shows only 10% metal substitution is necessary to enhance material stability.[66]

Due to the need to reuse adsorbent in order to economically separate CO_2, many studies have attempted to develop a simple prediction method for MOF stability. Among the results is an indication that either thermodynamic or kinetic factors can be dominant. Jasuja et al. characterized the water-induced degradation of the Zn-based DMOF-1 series and noted that certain functional groups prevent water attack, perhaps through steric protection, a kinetic mechanism.[67] Zinc-ligand bonds are very labile, explaining the consistent water-induced degradation problems encountered in zinc-carboxylate MOFs. ZIFs are more thermodynamically stable due to the fact that imidazoles are more strongly bound and exchange less readily. Complications arise when attempting to explain the trends for other metals due to multiple valence states, *in situ* redox reactions, and multiple favorable configurations.[68] Except for Cr^{+3} based MOFs, ligand exchange has been shown in a wide variety of MOFs, including those considered to be highly stable.[69, 70]

As MOF research has grown, the number of unique properties that have become easily accessible has greatly increased. Among these properties are framework flexibility and gate-opening. Although pure-component properties predict high selectivity, the measured values are much lower as the pores expand, as is evident in the case of the MIL-53 family of materials.[71, 72] Additionally, regeneration of flexible materials is inhibited by kinetic barriers which can prevent practical usage, such as in the case of MMOF-1.[73] MIL-53, like many other flexible framework materials, is highly selective with a small working capacity in the small pore form but selectivity is reduced almost by half when it transitions to the large pore form. It should be noted that the organic linkers and coordination bonds found in MOFs can rotate and flex to a significant degree, altering the pore sizes slightly, even if the framework is considered to be rigid.

5.3.3 *Cost and Safety*

Two major concerns to the design of optimal adsorption systems remain, material cost and material safety. Current estimates place MOF synthesis at three orders of magnitude more expensive than zeolites, but this is to be expected with new materials and synthesis methods. Significant strides are being made towards optimization and cost reduction of MOF synthesis along with subsequent commercialization.[23] Overall, the performance of MOFs must justify their cost, therefore, the criteria is that the optimal MOF for humid gas separations must remain stable for a long period of time and perform better than the lower-cost layered bed alternative.

Little is known about the health effects of MOFs, in part due to the vast number of known structures and combinations of organic and inorganic parts. Some MOFs are being pursued as drug delivery materials[74] and others are "edible",[75] so it can be inferred that if the ligands and metals have no toxic effects then the material should be safe upon degradation.[76] As the degradation rates and pathways of MOFs vary as wildly as their stability, no set of general rules can be determined. Additonally, it can be expected that non-degraded particles will have the same dangers as other nanoparticles and dust particulates, therefore similar precautions should be taken as adsorbents suffer attrition and breakage.

5.3.4 *Optimal Isotherm*

Currently, optimization of adsorption cycles utilizing existing adsorbents is the focus for system design. If the reverse situation is considered, optimization of the adsorbent for existing cycles, then tunable adsorbent properties are an absolute necessity. An optimal adsorbent is one with correctly tuned properties, even if the adsorbent isn't

record-breaking for any individual property.[40, 77] The adsorbent properties which improve performance for both PSA/VSA and TSA are: (1) high selectivity for CO_2 over other components, (2) large working capacity, (3) fast adsorption and desorption kinetics, (4) long-term stability, and (5) low sensitivity to contaminants, such as water vapor. For PSA/VSA systems, a linear isotherm shape between adsorption and desorption pressures as well as a low heat of adsorption are preferred. For TSA systems, a reasonably high heat of adsorption and more rectangular isotherm are preferred. Several reviews have covered the works on humid TSA systems, particularly supported amine adsorbents.[2, 19]

VSA experiments run under dry conditions on zeolite 13X show the importance of achievable vacuum on power consumption.[78] While dry VSA systems are well studied, humid gas separations using VSA processes are not as extensively studied. A series of lab-scale reports by the Webley research group provide a guide for proposing optimal properties.[79] These studies, which use zeolite 13X,[43] activated carbon,[44] and layered zeolite 13X beds[45, 46, 80] show the importance of limiting strong water adsorption at low pressures. The activated carbon bed weakly adsorbs water and shows the most rapid evacuation rate, but poor CO_2 selectivity limits the overall performance. The layered beds show the best recovery and purity, but a layered bed by definition limits the amount of active adsorbent in a packed bed and compounds an already complex optimization problem. Alternatively, separate dehydration is expected to add a flat cost of \$10.22 per ton CO_2 recovered, increasing best case costs by roughly 50%.[77] Therefore, a single adsorbent which can perform as well as the layered bed would be optimal.

MOFs are a class of crystalline materials made from the coordination of organic molecules to metal atoms or clusters to form porous networks. The combinations of organic linkers and inorganic secondary building units (SBUs) in various geometries leads to a vast number of structures.[81] The unique chemical and structural features found in MOFs provide for new approaches to solving the problem of carbon dioxide capture.[82-86] Also, the crystalline nature of MOFs enables detailed study of the adsorption mechanisms via simulations.[87]

MOFs can be designed to possess certain structural features which influence the target properties for humid VSA separations. The factors which relate to the total capacity and initial slope of an isotherm are (1) surface area and pore volume, and (2) zero loading heat of adsorption. The factors which relate to the overall shape of an isotherm are (1) the homogeneity of adsorption sites, (2) the density of adsorption sites, and (3) the flexibility of the framework. These effects on the shape can be described using the parameters of the Toth isotherm or the Langmuir-Freundlich isotherm for pure-component adsorption given in Eqs. 5.1 and 5.2 and Figure 5.2.[88]

$$q = q_{sat} * \frac{b\mathrm{P}}{[1 + (b\mathrm{P})^t]^{1/t}} \tag{5.1}$$

$$q = q_{sat} * \frac{(b\mathrm{P})^t}{1 + (b\mathrm{P})^t} \tag{5.2}$$

where P is pressure, q is amount of gas adsorbed at pressure P, q_{sat} is the saturation loading, b is adsorption affinity, and t is a fitting parameter describing the homogeneity of the adsorption sites or distribution of adsorption site energies.

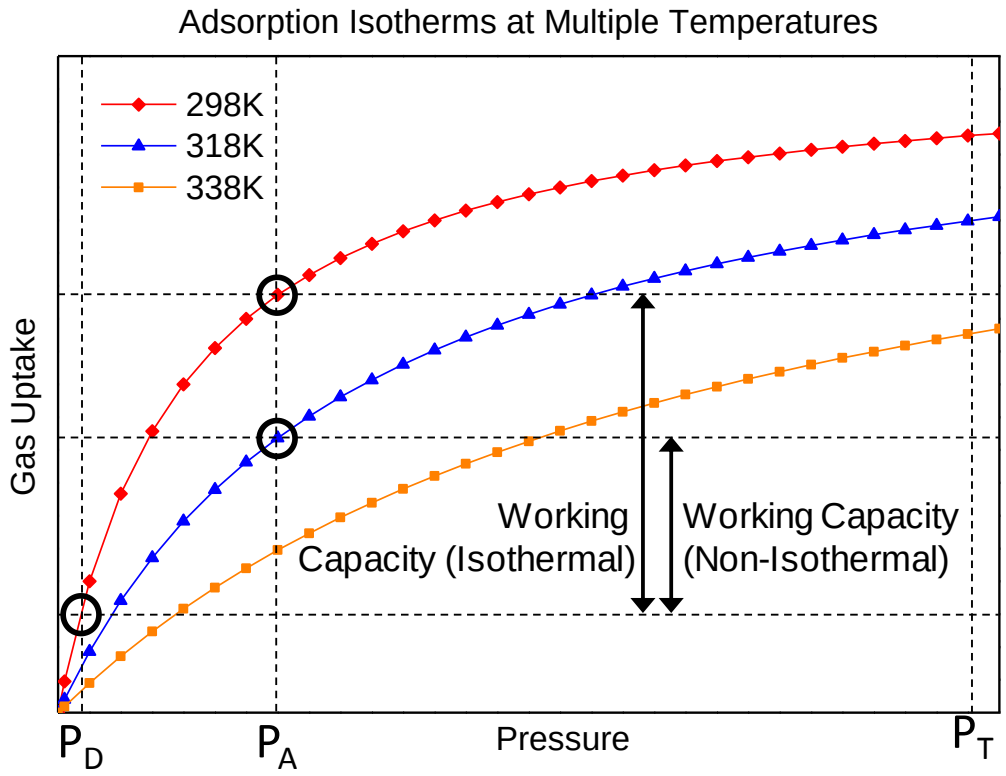

Figure 5.2. Representative isotherms for adsorption cycles at multiple temperatures. Adsorption (P_A), desorption (P_D), and total system (P_T) pressures as well as guidelines provided to emphasize the effect of temperature swings on working capacity.

Adsorbent properties affect the fitting parameters in the Toth equation in complex and often conflicting ways. For VSA systems, the optimal shape would be an isotherm with a high value for q_{sat}, a moderate value for b, and a t value close to unity. In the relevant low pressure regime, this hypothetical isotherm would be optimally steep and

linear, which is preferable for maximizing adsorbent utilization while minimizing the impact of temperature swings. Another way to view this would be as an optimally positioned "knee" in the isotherm. The knee is the range of pressure below which the majority of excess adsorption occurs. Since VSA processes operate in the regime before the knee, understanding the properties that best improve this region is essential.

Below the knee, the parameter q_{sat} is primarily affected by the density of adsorption sites, which can be related to heat of adsorption and surface area on a volumetric basis. Increasing either of these material properties leads to a higher q_{sat} value. The parameter b is affected by the strength of adsorption sites and increases with increasing heat of adsorption. The parameter t describes the heterogeneity of interactions between adsorbate molecules and adsorption sites, and is important for sub-critical and near-critical gas adsorption, such as CO_2 at room temperature. As t approaches unity, the distribution of interaction strengths becomes more uniform, a characteristic typically found at high temperatures or for poorly interacting species such as N_2 or He. For isothermal adsorption, the Henry's constant, the product of q_{sat} and b, provides a good comparison for VSA performance. An estimate for the effect of these parameters on working capacity is given in Figure 5.3.

Varying the parameters of an isotherm for a hypothetical adsorbent operating in a non-isothermal PSA system can show the effect of parameters relative to eachother. Figure 5.3 shows that the parameter b, if it could be decoupled from Q, has the greatest effect on working capacity. Also, in all cases, the working capacity increases as t approaches unity. It also shows nearly equal working capacity can be found from the

three cases which can be considered more realistic: high Q and b with moderate q_{sat}, low Q and b with high q_{sat}, and high b with low q_{sat} and Q.

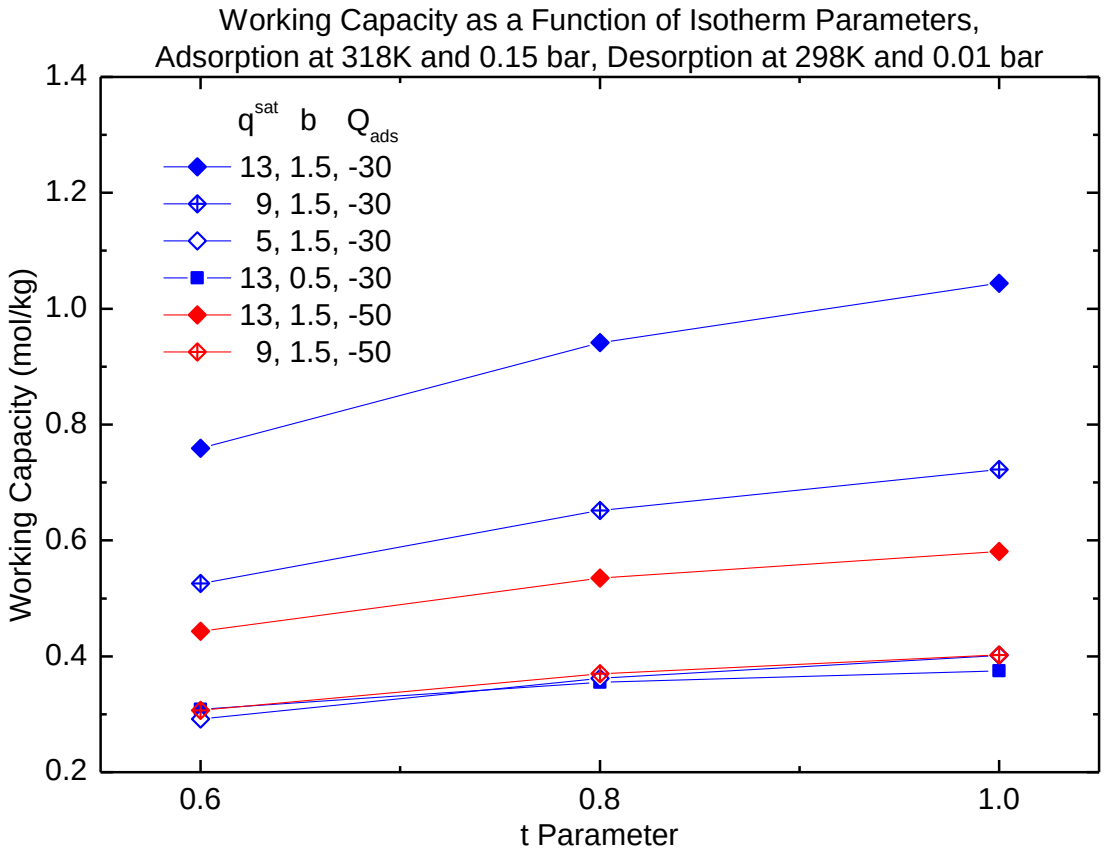

Figure 5.3. Estimated working capacities for various isotherm parameters. Parameter values chosen to span a range of realistic values.

Isothermal operation is one ideal limiting case for an adsorption system; the other being adiabatic operation. For non-isothermal operation, the Toth parameters are dependent on temperature; thus the targets for an optimal adsorbent change slightly. The most important equation describes the temperature dependence of the adsorption affinity given in Eq. 5.3.

$$b = b_{\infty} exp\left[\frac{\mathrm{Q}}{\mathrm{R_g T}}\right] \tag{5.3}$$

where T is temperature, Q is heat of adsorption, R_g is the ideal gas constant, and b_∞ is adsorption affinity at infinite temperature.

In Eq. 5.3, heat of adsorption (Q) is the important value for an adsorbent-adsorbate pair. Q is typically a decreasing function of gas loading, as stronger sites are occupied first. Higher values of Q lead to greater temperature sensitivity as the parameter b would decrease more rapidly with a rise in temperature. For VSA processes operating adiabatically, an optimal adsorbent must have a moderate heat of adsorption. An optimal heat of adsorption for CO_2 was calculated to be approximately 31 kJ/mol.[89] Considering a conventional adsorbent, one where all gases have equal access to adsorption sites, the difference in Q for each gas directly correlates to selectivity, a greater difference results in better selectivity. For some adsorbents, competitive gas adsorption is inhibited due to pore restrictions or unique structural properties, minimizing competition at certain sites, such as in the case of molecular sieves. This restriction reduces the need for large differences in the heat of adsorption for each adsorbate to yield selective separation.

The parameters q_{sat} and t can be fit to temperature dependent equations, but the dependence is typically negligible. Examples where they may be significant are such as when structural changes occur with changing temperature. Materials with flexible pendant groups, significant negative thermal expansion, and pore flexibility could show pore size transitions and thus changes in qsat. Some materials have shown improved

adsorption above a material-specific temperature, particularly when long hydrogen-bonding chains occupy large pore spaces, such as polyethyleneimine in silica[90] or in MIL-101.[91] The parameter *t* approaches unity as temperature rises, which can be thought of as the difference between adsorption site strengths becoming less pronounced and the pore surface becoming more energetically homogeneous to adsorbates.

Combining these factors, an optimal adsorbent will have a high density of adsorption sites, moderate heat of adsorption, a nearly homogeneous profile of adsorption energies, and a lack of adsorption sites for water. Considering this in terms of known physical properties, water-sensitive exposed metal sites and ultra-high gravimetric surface area materials cannot be considered optimal. The optimal adsorbent needs to be able to provide an adsorption potential which can uniquely and strongly interact with CO_2 but not water. For conventional adsorbents, these properties have been difficult to obtain, but the unique properties found in MOFs provide several viable alternative routes to develop an optimal adsorbent.

5.4 Conventional Optimization Methods

Currently, the major adsorbents for carbon dioxide separation include zeolites, activated carbons, carbonate minerals, and silica-supported amines.[2, 14, 92, 93] There exist drawbacks to each class which prevent immediate implementation in post-combustion systems.[19] The best features of these well characterized adsorbents can be imitated in certain MOFs due to the wide variety of chemical building blocks available. With the large library of known MOF features and the rich field of organic chemistry, the drawbacks of other adsorbents can potentially be overcome.

Increased surface area and greater density of strong adsorption sites have been the two major parameters of focus for improving carbon dioxide uptake and selectivity. These two parameters can be reliably controlled in activated carbons and zeolites and have been the key conventional comparisons within a material class. The correlation between CO_2 uptake and either surface area or density of adsorption sites is strong,[94] but these same factors are not indicative of good performance in an adsorption system on their own. Many adsorbent screenings for adsorption systems have been conducted to determine the primary performance factors.[95-98] The general conclusion for flue gas separation is that maximizing working capacity leads to the lowest energy cost, but the limited extent of water and stability data reduces the applicability of these results.[98] Also, the presence of water vapor greatly impacts most adsorbents by competitively adsorbing on the strong CO_2 binding sites.[99]

Applying these same methods to MOFs has yielded remarkable materials. The goal of maximizing surface area has been pushed nearly to theoretical limits in MOFs.[100, 101] These high surface area materials have been shown to perform poorly for low pressure applications where high excess adsorption on a volumetric basis is required. The other optimization goal of increased density of polar and ionic sites has also been a major focus in MOF research. Two well-known MOFs with exceptional performance, Mg-MOF-74 and HKUST-1, have a high density of CUS within the pores.[102] The CO_2 uptake is greater in Mg-MOF-74 than zeolite 13X although the density of CUS is less, as shown in Table 5.4. Neither of these benchmark MOFs is capable of overcoming the challenge of CO_2 capture from flue gas due to the same problem experienced in zeolites, preferential adsorption of water over CO_2. Additionally, as with many MOFs, these two

materials have been shown to degrade irreversibly in the presence of excess water vapor[60, 62] and an oxygenated atmosphere.[59] Therefore, other methods to design and select an optimal CO_2 adsorbent must be found for complex multicomponent gas separations such as humid flue gas.[12]

Table 5.4. Comparison of exposed cation site density and CO_2 uptake

Material	Density of exposed cations (nm^{-3})	CO_2 uptake at 0.15 bar, 298K (mol/kg)
Zeolite 13X[103]	5.5	4.77
(Mg)MOF-74[94]	4.6	6.13
CuBTC[94]	2.6	0.86
Fe-BTT[94]	1.8	1.20

5.5 New Optimization Strategies

5.5.1 *Size-Matched Pores*

Several general optimization strategies have been proposed.[85, 86] MOFs have the potential to enable "designed" pore spaces which provide new avenues to solving the challenges posed by flue gas.[104] Makal et al. noted that pores of widths equal to an integer number of adsorbate molecules show better performance.[105] Li et al. presented a strong foundation for classifying the major factors available to MOFs which influence selective adsorption in their review.[31] The list of factors includes size-matched pores, pore size/shape adjustments to match adsorbed species, and cooperative interactions. To

expand upon previous works, specific successes and further optimization targets will be discussed.

Perhaps the most promising optimization approach is to develop materials with size-matched pores for carbon dioxide, similar to molecular sieves and commensurate adsorbents. Size matching has been shown to be an effective method for improving selectivity.[106] Pore sizes matched to multiple molecules of CO_2 have also been shown to be effective.[107] Molecular sieves exhibit strong adsorption of carbon dioxide at low pressures due to overlap of adsorptive potentials from the closely spaced pore walls[22] as well as high selectivity due to size exclusion of larger molecules. The drawback of conventional molecular sieves is the near inflexibility of the pores which leads to slow diffusion rates. Also, rigid pores can more easily exhibit pore blockage due to adsorbed contaminants. MOFs can potentially overcome this drawback due to more flexible coordination bonds, rotation of organic linkers, and shifting of interpenetrated frameworks. Framework breathing is a similar behavior but leads to unfavorable hysteretic desorption and has been shown to be detrimental to selectivity.[71, 72]

Three well-known properties of MOFs are flexibility, bond rotation, and interpenetration. These can be used to create a material with the adsorption of a molecular sieve without severely restricting molecular diffusion rates. The coordination bonds found in MOFs are not as strong as the graphitic bonds of carbon molecular sieves or Si-O bonds of zeolites, which allows certain MOF frameworks to expand when exposed to external forces.[108] The rotation of planar aromatic rings commonly found in the organic linkers of MOFs allows for slight changes in the pore window sizes, a major factor in the diffusion properties of ZIF-8[109] and others.[110-112] Interpenetration is found

when two independent frameworks are interwoven and one framework can shift relative to the other. These modes of flexibility reduce the activation energy for molecules to pass through the pore windows of the framework and increases diffusion rates.

An example of this optimization method can be found in the SIFSIX series of materials where the size of the SiF_6^{-2} ion is of similar length to a single CO_2 molecule.[113, 114] Interpenetration of SIFSIX-2-Cu-i leads to a material with enough flexibility to readily admit molecules throughout the crystal structure yet with pore dimensions nearly equal to the size of a single CO_2 molecule. The performance of this material is very good despite the conventional factors predicting mediocre performance. In comparison to other MOFs, this material possesses relatively low BET surface area (735 m^2/g), no open-metal sites, non-polar organic linkers, and numerous fluorine atoms.[32] Instead, the size-matched pores leads to close proximity to the pore walls and strong adsorption of CO_2. Also, CO_2 is preferentially adsorbed over water due to the lack of hydrophilic sites in the pores.[114] Future development should seek to maintain the hydrophobic properties while increasing the CO_2 interactions in the size-matched pores with a goal of a higher Henry's constant for CO_2 uptake.

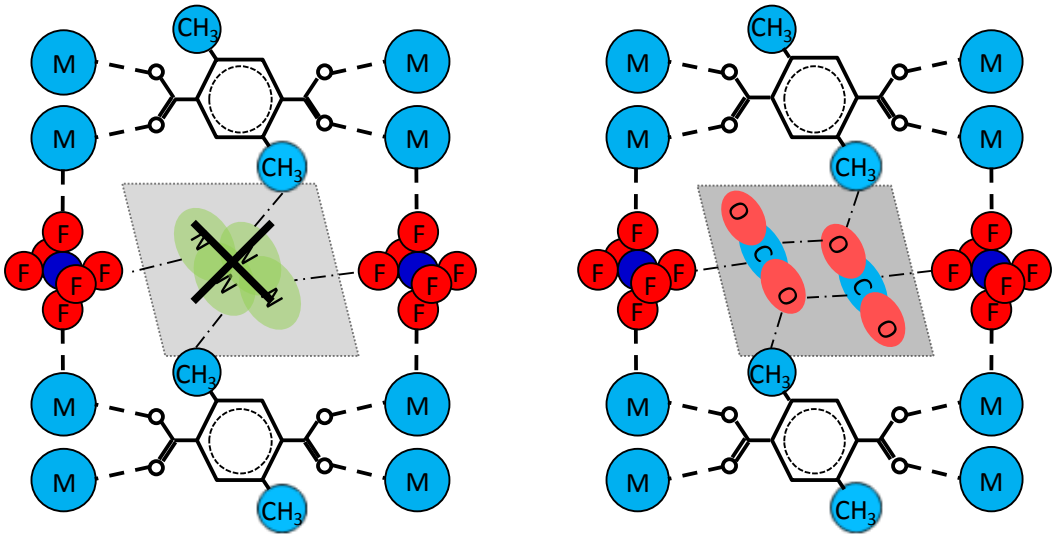

Figure 5.4. Hypothetical adsorption space with schematic optimal interactions. The average adsorption length for CO_2 is shorter than for N_2, allowing for multiple molecules of CO_2 to adsorb in the pore space.

5.5.2 *Single-Molecule Traps*

Another optimization method is based on reticular synthesis,[115, 116] which is the systematic approach to synthesizing targeted frameworks from known SBUs and analogous organic linkers.[57, 117] Isoreticular materials were first formed with the Zn_4O SBU and numerous benzene dicarboxylate analogs. The concept was subsequently extended to other metal clusters. The $Cu_2(COO)_4$ paddlewheel SBU has been synthesized with numerous linkers in a wide range of structures, is moderately water stable,[118] and possesses open-metal sites, which makes it a good candidate for carbon dioxide capture studies. In most cases, the open-metal sites are spaced far apart leading to only one oxygen of a CO_2 molecule interacting with the strong adsorption site, but ligand design can lead to precise spacing and multiple interactions.[117, 119] Similar molecule-length spacing is found in zeolites leading to very strong adsorption sites,

although these sites cannot be directly produced in a controlled manner.[120] For a humid system, a longer ligand can be used in order to allow water to occupy the open-metal sites and CO_2 to adsorb between the bound water molecules. Among other SBUs, those related to Cr_3O^{+7} and Mn_4Cl^{+7} are additional candidates as there have been several studies indicating good stability.[121, 122]

An example of this process is the synthesis of 'single-molecule traps'.[123-125] A designed linker connects two copper paddlewheels in a co-axial arrangement with a gap between two metal atoms tuned for the length of CO_2. Both oxygens of a CO_2 molecule interact with the open-metal sites, which leads to a strong and highly selective adsorption site. Currently, the material synthesized possesses a low framework density and thus the density of adsorption sites is low. Flue gas applications would require a higher total uptake of CO_2. Also, due to the large, non-selective voids between the traps, overall selectivity is low. Further improvements could focus on applying this technique to interpenetrated materials in order to increase the density of active adsorption sites. Also, more stable SBUs such as Cr_3O^{+7} could be utilized to make these traps.

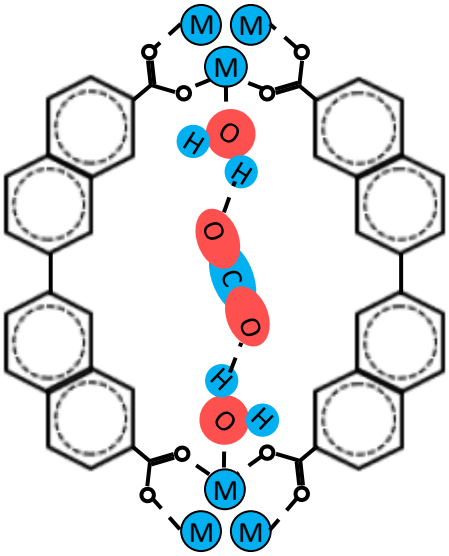

Figure 5.5. Hypothetical example of cooperative water adsorption in a single-molecule trap.

5.5.3 *Cooperative Water-CO_2 Interactions*

Several other methods for improving CO_2 adsorption from flue gas exist which have been studied. One of these methods is to synthesize MOFs with metals which interact less strongly with water. An example of the effect of different metal CUSs can be found in the Mg, Ni, and Co members of the MOF-74 family. The performance of the Mg-based material has been shown to be highly susceptible to water,[59, 62, 126] whereas published results of the Ni and Co-based materials indicate good stability and acceptable CO_2 uptake in humidified streams.[61, 127-129]

Another method involves partially-hydrophilic, mesoporous MOFs showing unaffected or even improved uptake when pre-loaded with water. (Cr)MIL-101 shows negligible loss of CO_2 capacity in the presence of water,[130] whereas an enhanced CO_2 uptake was found for (Fe)MIL-100 when pre-loaded with water.[131] Although water has a major impact on CO_2 uptake by occupying the CUS, unexpected interactions have been

observed and thus more study is needed on highly water stable MOFs with CUS. This "oversolubility" phenomenon was further explored by Ho et al. and attributed the improvement to enhanced pore surface interactions with CO_2 in the presence of solvent.[132] It should be noted that large-scale estimates of implementing MOFs in capture systems has lead to the conclusion that some metals are simply not feasible due to limited world-wide supplies.[133]

5.5.4 *Post-Synthetic Modification*

Another method to improve CO_2 adsorption in humid systems is post-synthetic modification (PSM). Anchoring of alkyldiamines to the CUS of MOFs has been used to produce highly selective materials.[134-136] The major benefits are water-tolerant adsorption of CO_2[137] and unique adsorption properties not found in other adsorbents.[136] Since this modification replaces one strong binding site with another and reduces porosity, CO_2 isotherms are generally shifted to more rectangular shapes with lower total capacity while selectivity over N_2 increases. A more rectangular isotherm is favorable for CO_2 capture from air.[134, 135] Comparisons to amine-functionalized silica are evident, and the performance of those materials is considered the benchmark to exceed with PSM in MOFs. Similar performance in humid streams[138] and similar problems with oxidizing atmospheres[139] are to be expected. Additional PSMs include partial metal substitution,[69, 140, 141] ligand exchange,[70, 142] ammonium treatment,[143, 144] and polyamine immobilization in mesopores[91] which can lead to properties not obtained via direct synthesis methods.

PPN-6 and related porous aromatic frameworks (PAFs) are formed entirely of strong covalent bonds, imparting great stability relative to MOFs. Recently, several techniques to modify the aromatic rings in PPN-6 were used to incorporate highly

selective functionalities into a lightweight framework at high density.[144-147] The high stability, high density of adsorption sites, low framework mass, and high surface area means these materials have great potential, although the difficult, multi-step synthesis methods may pose scale-up challenges.

The first method involves chloromethylation of the aromatic rings with subsequent amine substitution. The second method involves sulphonation and subsequent acid-base reaction with ammonia or metal salt. Such processes are only possible on the most stable of materials due to the harsh reaction conditions. (Cr)MIL-101 is the presently the only MOF tested to withstand similar harsh conditions for these types of PSM.[148] Simulations with other functionalities were performed, indicating several alkylamine modifications would yield improved performance over standard MEA solution for flue gas capture in a TSA cycle.[149] Simulations of an ether modified PAF material predict a physisorbent with excellent adsorption properties.[150] Optimization of synthesis and PSM for large-scale synthesis of these stable materials would produce highly promising adsorbents.

5.5.5 *Targeted Synthesis*

As all of these proposed optimization strategies target certain structures, the feasibility of targeted synthesis must be considered. Targeted synthesis has been and remains one of the major goals in designing MOFs for adsorption applications, with an enormous number of SBUs reported.[56, 151, 152] Only a few of these SBUs were known and studied before MOFs, for example, the Zn_4O SBU is found as basic zinc acetate. This is an example of successful targeted synthesis where utilizing similar conditions to form basic zinc acetate enabled the synthesis of the famous MOF-5 material.[153] Other clusters

have been transitioned in a similar manner, such as enabling the structure solution to MIL-100 and MIL-101.[121, 154] Organic and coordination chemistry have been successfully used on specific occasions to design targeted materials.[100, 101, 116, 155-157] Although the concept of tailor-made materials is promising, these are exceptional cases as the general situation is far more unpredictable.[158, 159] The majority of MOFs, including several record-breaking materials, have been discovered by non-targeted methods.

5.5.6 *Additional Methods*

Although a number of methods have been proposed here to overcome the problem of loss of adsorbent performance in humid gas separations, there are undoubtedly more methods yet to pursue. In order to identify these materials among the thousands of available MOF structures, selection criteria must be determined. First, stability criteria and material production costs allow for a reduction in the total number of MOFs under consideration. Next, determination of features which lead to pore filling in the presence of water vapor allow for a further reduction of materials to be excluded. Finally, identifying pore features which produce to multiple interactions with adsorbed CO_2 allows for better adsorbate selectivity and uptake. This incremental method may identify additional adsorbent optimizations and ultimately lead to materials and processes which can to efficiently capture carbon dioxide in humid systems.

5.6 Conclusions and Perspective

In conclusion, the optimization of adsorbents for carbon dioxide capture from flue gas remains one of the most difficult challenges facing engineers and material scientists today. The challenges range from researching new materials to their implementation and

use. The subjects covered here target as many of the relevant points of the entire problem as possible. How the molecules interact with adsorbent surfaces, the challenging properties of flue gas, and how current engineering methods attempt to solve the problem of selective CO_2 removal are discussed. The foundational thinking for adsorbent material design is discussed followed by how MOFs can overcome the drawbacks that have been observed with currently available materials. Considerations for the optimal properties are suggested, specifically an optimal CO_2 adsorbent would have low to moderate heat of adsorption, a homogeneous distribution of equivalent adsorption sites, and pore surfaces which inhibit competitive adsorption from water and N_2. The over-arching requirements of cost and stability are discussed and it is noted that these constraints significantly reduce the number of candidate MOFs.

With these considerations, a number of MOF structures and methods are discussed with potential for providing a water-tolerant CO_2 adsorbent for flue gas separations. The major optimization methods described are size-matched pores, single-molecule traps, cooperative water-CO_2 interactions, and post-synthetic modifications. To handle the large volumetric flow rates of flue gas, novel adsorption systems must be engineered with an emphasis toward heat management and rapid cycles in order to achieve better utilization of adsorbent material.

MOFs continue to be an exciting field of research and connect adsorption engineering with organic, inorganic, and synthetic chemistry. This connection has led to thousands of reported materials, with unique properties and potential for CO_2 capture from humid systems. The challenge of carbon capture is one which requires engineering

and material design solutions, a unique position to which chemical engineers are well suited.

5.7 References

1. Sumida, K., et al., *Carbon dioxide capture in metal-organic frameworks.* Chem Rev, 2012. **112**(2): p. 724-81.

2. Choi, S., J.H. Drese, and C.W. Jones, *Adsorbent materials for carbon dioxide capture from large anthropogenic point sources.* ChemSusChem, 2009. **2**(9): p. 796-854.

3. Tagliabue, M., et al., *Natural gas treating by selective adsorption: Material science and chemical engineering interplay.* Chemical Engineering Journal, 2009. **155**(3): p. 553-566.

4. Wang, Q.A., et al., *CO2 capture by solid adsorbents and their applications: current status and new trends.* Energy & Environmental Science, 2011. **4**(1): p. 42-55.

5. Jones, C.W., *CO(2) capture from dilute gases as a component of modern global carbon management.* Annu Rev Chem Biomol Eng, 2011. **2**: p. 31-52.

6. Spigarelli, B.P. and S.K. Kawatra, *Opportunities and challenges in carbon dioxide capture.* Journal of CO2 Utilization, 2013. **1**: p. 69-87.

7. Bhown, A.S. and B.C. Freeman, *Analysis and status of post-combustion carbon dioxide capture technologies.* Environ Sci Technol, 2011. **45**(20): p. 8624-32.

8. Kenarsari, S.D., et al., *Review of recent advances in carbon dioxide separation and capture.* RSC Advances, 2013. **3**: p. 22739.

9. *Collins, M., R. Knutti, J. Arblaster, J.-L. Dufresne, T. Fichefet, P. Friedlingstein, X. Gao, W.J. Gutowski, T. Johns, G. Krinner, M. Shongwe, C. Tebaldi, A.J. Weaver and M. Wehner, 2013: Long-term Climate Change: Projections, Commitments and Irreversibility. In: Climate Change 2013: The Physical Science Basis. Contribution of Working Group I to the Fifth Assessment Report of the Intergovernmental Panel on Climate Change [Stocker, T.F., D. Qin, G.-K. Plattner, M. Tignor, S.K. Allen, J. Boschung, A. Nauels, Y. Xia, V. Bex and P.M. Midgley (eds.)]. Cambridge University Press, Cambridge, United Kingdom and New York, NY, USA.*

10. *Natural Gas Processing: The Crucial Link Between Natural Gas Production and Its Transportation to Market*, U.S. Energy Information Administration, Office of Oil and Gas.

11. Hedin, N., L. Chen, and A. Laaksonen, *Sorbents for CO(2) capture from flue gas--aspects from materials and theoretical chemistry.* Nanoscale, 2010. **2**(10): p. 1819-41.

12. Drage, T.C., et al., *Materials challenges for the development of solid sorbents for post-combustion carbon capture.* Journal of Materials Chemistry, 2012. **22**(7): p. 2815-2823.

13. Rochelle, G.T., *Amine scrubbing for CO2 capture.* Science, 2009. **325**(5948): p. 1652-4.

14. Yu, C.H., C.H. Huang, and C.S. Tan, *A Review of CO2 Capture by Absorption and Adsorption.* Aerosol and Air Quality Research, 2012. **12**(5): p. 745-769.

15. Feron, P.H.M., *Exploring the potential for improvement of the energy performance of coal fired power plants with post-combustion capture of carbon dioxide.* International Journal of Greenhouse Gas Control, 2010. **4**: p. 152-160.

16. *DOE/NETL Advanced Carbon Dioxide Capture R&D Program: Technology Update, May 2013 ed.; National Energy Technology Laboratory, 2013; p 65, http://www.netl.doe.gov/research/coal/carbon-capture/capture-handbook (accessed January 15, 2014).*

17. Pirngruber, G.D., et al., *A theoretical analysis of the energy consumption of post-combustion CO2 capture processes by temperature swing adsorption using solid sorbents.* International Journal of Greenhouse Gas Control, 2013. **14**: p. 74-83.

18. Sjostrom, S. and H. Krutka, *Evaluation of solid sorbents as a retrofit technology for CO2 capture.* Fuel, 2010. **89**: p. 1298-1306.

19. Sayari, A., Y. Belmabkhout, and R. Serna-Guerrero, *Flue gas treatment via CO2 adsorption.* Chemical Engineering Journal, 2011. **171**(3): p. 760-774.

20. Yang, R.T., *Gas separation by adsorption processes*. Series on chemical engineering1997, Singapore ; River Edge, N.J.: World Scientific. x, 352 p.

21. Férey, G., et al., *Why hybrid porous solids capture greenhouse gases?* Chem Soc Rev, 2011. **40**(2): p. 550-62.

22. Broom, D.P. and K.M. Thomas, *Gas adsorption by nanoporous materials: Future applications and experimental challenges.* Mrs Bulletin, 2013. **38**(5): p. 412-421.

23. Czaja, A.U., N. Trukhan, and U. Muller, *Industrial applications of metal-organic frameworks.* Chem Soc Rev, 2009. **38**(5): p. 1284-93.

24. Myers, A.L., *Thermodynamics of adsorption in porous materials.* Aiche Journal, 2002. **48**(1): p. 145-160.

25. Myers, A.L. and J.M. Prausnitz, *Thermodynamics of Mixed-Gas Adsorption.* Aiche Journal, 1965. **11**(1): p. 121-+.

26. Ding, L. and A.Ö. Yazaydin, *How Well Do Metal–Organic Frameworks Tolerate Flue Gas Impurities?* The Journal of Physical Chemistry C, 2012. **116**(43): p. 22987-22991.

27. Yu, J., Y. Ma, and P.B. Balbuena, *Evaluation of the impact of H2O, O2, and SO2 on postcombustion CO2 capture in metal-organic frameworks.* Langmuir, 2012. **28**(21): p. 8064-71.

28. Ding, L. and A.O. Yazaydin, *The effect of SO2 on CO2 capture in zeolitic imidazolate frameworks.* Phys Chem Chem Phys, 2013. **15**(28): p. 11856-61.

29. Supronowicz, B., A. Mavrandonakis, and T. Heine, *Interaction of Small Gases with the Unsaturated Metal Centers of the HKUST-1 Metal Organic Framework.* The Journal of Physical Chemistry C, 2013. **117**: p. 14570-14578.

30. Canepa, P., et al., *High-throughput screening of small-molecule adsorption in MOF.* Journal of Materials Chemistry A, 2013. **1**: p. 13597.

31. Li, J.R., R.J. Kuppler, and H.C. Zhou, *Selective gas adsorption and separation in metal-organic frameworks.* Chem Soc Rev, 2009. **38**(5): p. 1477-504.

32. Burtch, N.C., et al., *Molecular-level insight into unusual low pressure CO2 affinity in pillared metal-organic frameworks.* J Am Chem Soc, 2013. **135**(19): p. 7172-80.

33. Kitagawa, S. and R. Matsuda, *Chemistry of coordination space of porous coordination polymers.* Coordination Chemistry Reviews, 2007. **251**(21-24): p. 2490-2509.

34. Yazaydin, A.O., et al., *Screening of metal-organic frameworks for carbon dioxide capture from flue gas using a combined experimental and modeling approach.* J Am Chem Soc, 2009. **131**(51): p. 18198-9.

35. Hasan, M.M.F., et al., *Modeling, Simulation, and Optimization of Postcombustion CO2Capture for Variable Feed Concentration and Flow Rate. 2. Pressure Swing Adsorption and Vacuum Swing Adsorption Processes.* Industrial & Engineering Chemistry Research, 2012. **51**(48): p. 15665-15682.

36. Mumford, K.A., et al., *Post-combustion Capture of CO2: Results from the Solvent Absorption Capture Plant at Hazelwood Power Station Using Potassium Carbonate Solvent.* Energy & Fuels, 2012. **26**(1): p. 138-146.

37. *U.S. Environmental Protection Agency. Report of the Interagency Task Force on Carbon Capture and Storage. August 2010. http://www.epa.gov/climatechange/Downloads/ccs/CCS-Task-Force-Report-2010.pdf. Accessed January 15, 2014.*

38. *American Petroleum Institute. Summary of Carbon Dioxide Enhanced Oil Recovery (CO2EOR) Injection Well Technology. Meyer, James P. http://api.org/~/media/Files/EHS/climate-change/Summary-carbon-dioxide-enhanced-oil-recovery-well-tech.pdf. Accessed January 15, 2014.*

39. Mason, J.A., et al., *Evaluating metal–organic frameworks for post-combustion carbon dioxide capture via temperature swing adsorption.* Energy & Environmental Science, 2011. **4**(8): p. 3030.

40. Merel, J., M. Clausse, and F. Meunier, *Experimental Investigation on CO 2 Post− Combustion Capture by Indirect Thermal Swing Adsorption Using 13X and 5A Zeolites.* Industrial & Engineering Chemistry Research, 2008. **47**: p. 209-215.

41. Tlili, N., G. Grévillot, and C. Vallières, *Carbon dioxide capture and recovery by means of TSA and/or VSA.* International Journal of Greenhouse Gas Control, 2009. **3**(5): p. 519-527.

42. Grande, C.A., *Advances in Pressure Swing Adsorption for Gas Separation.* ISRN Chemical Engineering, 2012. **2012**: p. 1-13.

43. Li, G., et al., *Capture of CO2 from high humidity flue gas by vacuum swing adsorption with zeolite 13X.* Adsorption-Journal of the International Adsorption Society, 2008. **14**(2-3): p. 415-422.

44. Xu, D., et al., *Effect of water vapor from power station flue gas on CO2 capture by vacuum swing adsorption with activated carbon.* Journal of Fuel Chemistry and Technology, 2011. **39**(3): p. 169-174.

45. Li, G., et al., *Competition of CO2/H2O in adsorption based CO2 capture.* Energy Procedia, 2009. **1**(1): p. 1123-1130.

46. Xu, D., et al., *CO2 Capture by Vacuum Swing Adsorption Using F200 and Sorbead WS as Protective Pre-layers.* Chinese Journal of Chemical Engineering, 2012. **20**(5): p. 849-855.

47. Lively, R.P., et al., *Hollow Fiber Adsorbents for CO2Removal from Flue Gas.* Industrial & Engineering Chemistry Research, 2009. **48**(15): p. 7314-7324.

48. Rezaei, F. and P. Webley, *Structured adsorbents in gas separation processes.* Separation and Purification Technology, 2010. **70**(3): p. 243-256.

49. Rezaei, F., et al., *Comparison of Traditional and Structured Adsorbents for CO 2 Separation by Vacuum-Swing Adsorption.* Industrial & Engineering Chemistry Research, 2010. **49**: p. 4832-4841.

50. Rezaei, F. and P.A. Webley, *Optimal design of engineered gas adsorbents: Pore-scale level.* Chemical Engineering Science, 2012. **69**(1): p. 270-278.

51. Rezaei, F. and M. Grahn, *Thermal Management of Structured Adsorbents in CO2Capture Processes.* Industrial & Engineering Chemistry Research, 2012. **51**(10): p. 4025-4034.

52. Cavenati, S., C.a. Grande, and A.E. Rodrigues, *Removal of Carbon Dioxide from Natural Gas by Vacuum Pressure Swing Adsorption.* Energy & Fuels, 2006. **20**: p. 2648-2659.

53. Rezaei, F. and P. Webley, *Optimum structured adsorbents for gas separation processes.* Chemical Engineering Science, 2009. **64**(24): p. 5182-5191.

54. Stock, N. and S. Biswas, *Synthesis of metal-organic frameworks (MOFs): routes to various MOF topologies, morphologies, and composites.* Chem Rev, 2012. **112**(2): p. 933-69.

55. Hedin, N., et al., *Adsorbents for the post-combustion capture of CO2 using rapid temperature swing or vacuum swing adsorption.* Applied Energy, 2013. **104**: p. 418-433.

56. Cook, T.R., Y.R. Zheng, and P.J. Stang, *Metal-organic frameworks and self-assembled supramolecular coordination complexes: comparing and contrasting the design, synthesis, and functionality of metal-organic materials.* Chem Rev, 2013. **113**(1): p. 734-77.

57. Jhung, S.H., N.A. Khan, and Z. Hasan, *Analogous porous metal–organic frameworks: synthesis, stability and application in adsorption.* CrystEngComm, 2012. **14**(21): p. 7099.

58. Helm, L. and A.E. Merbach, *Water exchange on metal ions: experiments and simulations.* Coordination Chemistry Reviews, 1999. **187**: p. 151-181.

59. Schoenecker, P.M., et al., *Effect of Water Adsorption on Retention of Structure and Surface Area of Metal–Organic Frameworks.* Industrial & Engineering Chemistry Research, 2012. **51**(18): p. 6513-6519.

60. Low, J.J., et al., *Virtual high throughput screening confirmed experimentally: porous coordination polymer hydration.* J Am Chem Soc, 2009. **131**(43): p. 15834-42.

61. Liu, J., et al., *Stability effects on CO2 adsorption for the DOBDC series of metal-organic frameworks.* Langmuir, 2011. **27**(18): p. 11451-6.

62. Remy, T., et al., *Selective Dynamic CO2Separations on Mg-MOF-74 at Low Pressures: A Detailed Comparison with 13X.* The Journal of Physical Chemistry C, 2013. **117**(18): p. 9301-9310.

63. DeCoste, J.B., et al., *The effect of water adsorption on the structure of the carboxylate containing metal–organic frameworks Cu-BTC, Mg-MOF-74, and UiO-66.* Journal of Materials Chemistry A, 2013. **1**: p. 11922.

64. Li, H., et al., *Enhanced hydrostability in Ni-doped MOF-5.* Inorg Chem, 2012. **51**(17): p. 9200-7.

65. Kahr, J., R.E. Morris, and P.a. Wright, *Post-synthetic incorporation of nickel into CPO-27(Mg) to give materials with enhanced permanent porosity.* CrystEngComm, 2013. **15**: p. 9779.

66. Song, X., M. Oh, and M.S. Lah, *Hybrid bimetallic metal-organic frameworks: modulation of the framework stability and ultralarge CO2 uptake capacity.* Inorganic chemistry, 2013. **52**: p. 10869-76.

67. Jasuja, H., et al., *Kinetic water stability of an isostructural family of zinc-based pillared metal-organic frameworks.* Langmuir, 2013. **29**(2): p. 633-42.

68. Bellarosa, L., S. Calero, and N. Lopez, *Early stages in the degradation of metal-organic frameworks in liquid water from first-principles molecular dynamics.* Phys Chem Chem Phys, 2012. **14**(20): p. 7240-5.

69. Kim, M., et al., *Postsynthetic ligand and cation exchange in robust metal-organic frameworks.* J Am Chem Soc, 2012. **134**(43): p. 18082-8.

70. Karagiaridi, O., et al., *Opening ZIF-8: a catalytically active zeolitic imidazolate framework of sodalite topology with unsubstituted linkers.* J Am Chem Soc, 2012. **134**(45): p. 18790-6.

71. Hamon, L., et al., *Co-adsorption and separation of CO2-CH4 mixtures in the highly flexible MIL-53(Cr) MOF.* J Am Chem Soc, 2009. **131**(47): p. 17490-9.

72. Finsy, V., et al., *Separation of CO2/CH4 mixtures with the MIL-53(Al) metal–organic framework.* Microporous and Mesoporous Materials, 2009. **120**(3): p. 221-227.

73. Sircar, S., et al., *Effect of time, temperature, and kinetics on the hysteretic adsorption-desorption of H2, Ar, and N2 in the metal-organic framework Zn2(bpdc)2(bpee).* Langmuir, 2011. **27**(23): p. 14169-79.

74. Horcajada, P., et al., *Porous metal-organic-framework nanoscale carriers as a potential platform for drug delivery and imaging.* Nature materials, 2010. **9**: p. 172-8.

75. Forgan, R.S., et al., *Nanoporous carbohydrate metal-organic frameworks.* Journal of the American Chemical Society, 2012. **134**: p. 406-17.

76. Baati, T., et al., *In depth analysis of the in vivo toxicity of nanoparticles of porous iron(iii) metal–organic frameworks.* Chemical Science, 2013. **4**: p. 1597.

77. Hasan, M.M.F., E.L. First, and C.a. Floudas, *Cost-effective CO2 capture based on in silico screening of zeolites and process optimization.* Physical chemistry chemical physics : PCCP, 2013. **15**: p. 17601-18.

78. Xiao, P., et al., *Capture of CO2 from flue gas streams with zeolite 13X by vacuum-pressure swing adsorption.* Adsorption, 2008. **14**(4-5): p. 575-582.

79. Chaffee, A.L., et al., *CO2 capture by adsorption: Materials and process development.* International Journal of Greenhouse Gas Control, 2007. **1**: p. 11-18.

80. Zhang, J., et al., *Effect of flue gas impurities on CO2 capture performance from flue gas at coal-fired power stations by vacuum swing adsorption.* Energy Procedia, 2009. **1**: p. 1115-1122.

81. Long, J.R. and O.M. Yaghi, *The pervasive chemistry of metal-organic frameworks.* Chem Soc Rev, 2009. **38**(5): p. 1213-4.

82. Keskin, S., T.M. van Heest, and D.S. Sholl, *Can metal-organic framework materials play a useful role in large-scale carbon dioxide separations?* ChemSusChem, 2010. **3**(8): p. 879-91.

83. Li, J.R., et al., *Carbon dioxide capture-related gas adsorption and separation in metal-organic frameworks.* Coordination Chemistry Reviews, 2011. **255**(15-16): p. 1791-1823.

84. Bae, Y.S. and R.Q. Snurr, *Development and evaluation of porous materials for carbon dioxide separation and capture.* Angew Chem Int Ed Engl, 2011. **50**(49): p. 11586-96.

85. Liu, J., et al., *Progress in adsorption-based CO2 capture by metal-organic frameworks.* Chem Soc Rev, 2012. **41**(6): p. 2308-22.

86. Liu, Y.Y., Z.Y.U. Wang, and H.C. Zhou, *Recent advances in carbon dioxide capture with metal-organic frameworks.* Greenhouse Gases-Science and Technology, 2012. **2**(4): p. 239-259.

87. Xiang, Z.H., et al., *Multiscale simulation and modelling of adsorptive processes for energy gas storage and carbon dioxide capture in porous coordination frameworks.* Energy & Environmental Science, 2010. **3**(10): p. 1469-1487.

88. Duong, D.D., *Adsorption analysis : equilibria and kinetics*. Series on chemical engineering1998, London: Imperial College Press. xxi, 892 p.

89. Simmons, J.M., et al., *Carbon capture in metal–organic frameworks—a comparative study.* Energy & Environmental Science, 2011. **4**(6): p. 2177.

90. Bacsik, Z., et al., *Temperature-induced uptake of CO2 and formation of carbamates in mesocaged silica modified with n-propylamines.* Langmuir, 2010. **26**(12): p. 10013-24.

91. Lin, Y., et al., *Polyethyleneimine incorporated metal-organic frameworks adsorbent for highly selective CO2 capture.* Sci Rep, 2013. **3**: p. 1859.

92. Hao, G.P., W.C. Li, and A.H. Lu, *Novel porous solids for carbon dioxide capture.* Journal of Materials Chemistry, 2011. **21**(18): p. 6447-6451.

93. Samanta, A., et al., *Post-Combustion CO2Capture Using Solid Sorbents: A Review.* Industrial & Engineering Chemistry Research, 2012. **51**(4): p. 1438-1463.

94. Zhang, Z., et al., *MOFs for CO2 capture and separation from flue gas mixtures: the effect of multifunctional sites on their adsorption capacity and selectivity.* Chem Commun (Camb), 2013. **49**(7): p. 653-61.

95. Wiersum, A.D., et al., *An adsorbent performance indicator as a first step evaluation of novel sorbents for gas separations: application to metal-organic frameworks.* Langmuir, 2013. **29**(10): p. 3301-9.

96. Lin, L.C., et al., *In silico screening of carbon-capture materials.* Nat Mater, 2012. **11**(7): p. 633-41.

97. Krishna, R. and J.M. van Baten, *In silico screening of metal-organic frameworks in separation applications.* Phys Chem Chem Phys, 2011. **13**(22): p. 10593-616.

98. Pirngruber, G.D., et al., *A method for screening the potential of MOFs as CO2 adsorbents in pressure swing adsorption processes.* ChemSusChem, 2012. **5**(4): p. 762-76.

99. Wang, Y. and M.D. LeVan, *Adsorption Equilibrium of Carbon Dioxide and Water Vapor on Zeolites 5A and 13X and Silica Gel: Pure Components.* Journal of Chemical & Engineering Data, 2009. **54**: p. 2839-2844.

100. Farha, O.K., et al., *Metal-organic framework materials with ultrahigh surface areas: is the sky the limit?* J Am Chem Soc, 2012. **134**(36): p. 15016-21.

101. Yuan, D., et al., *An isoreticular series of metal-organic frameworks with dendritic hexacarboxylate ligands and exceptionally high gas-uptake capacity.* Angew Chem Int Ed Engl, 2010. **49**(31): p. 5357-61.

102. Britt, D., et al., *Highly efficient separation of carbon dioxide by a metal-organic framework replete with open metal sites.* Proc Natl Acad Sci U S A, 2009. **106**(49): p. 20637-40.

103. Dirar, Q.H. and K.F. Loughlin, *Intrinsic adsorption properties of CO2 on 5A and 13X zeolite.* Adsorption, 2013. **19**(6): p. 1149-1163.

104. Martin, R.L. and M. Haranczyk, *Optimization-Based Design of Metal–Organic Framework Materials.* Journal of Chemical Theory and Computation, 2013. **9**(6): p. 2816-2825.

105. Makal, T.A., et al., *Methane storage in advanced porous materials.* Chem Soc Rev, 2012. **41**(23): p. 7761-79.

106. Wu, H., et al., *Commensurate adsorption of hydrocarbons and alcohols in microporous metal organic frameworks.* Chem Rev, 2012. **112**(2): p. 836-68.

107. Xiang, S., et al., *Microporous metal-organic framework with potential for carbon dioxide capture at ambient conditions.* Nat Commun, 2012. **3**: p. 954.

108. Serre, C., et al., *Very large breathing effect in the first nanoporous chromium(III)-based solids: MIL-53 or Cr-III(OH)center dot{O2C-C6H4-CO2}center dot{HO2C-C6H4-CO2H}(x)center dot H2Oy.* Journal of the American Chemical Society, 2002. **124**(45): p. 13519-13526.

109. Haldoupis, E., et al., *Quantifying large effects of framework flexibility on diffusion in MOFs: CH4 and CO2 in ZIF-8.* Chemphyschem, 2012. **13**(15): p. 3449-52.

110. Watanabe, T., et al., *Computational identification of a metal organic framework for high selectivity membrane-based CO2/CH4 separations: Cu(hfipbb)(H2hfipbb)0.5.* Phys Chem Chem Phys, 2009. **11**(48): p. 11389-94.

111. Zhang, J.P. and X.M. Chen, *Exceptional framework flexibility and sorption behavior of a multifunctional porous cuprous triazolate framework.* J Am Chem Soc, 2008. **130**(18): p. 6010-7.

112. Horike, S., S. Shimomura, and S. Kitagawa, *Soft porous crystals.* Nat Chem, 2009. **1**(9): p. 695-704.

113. Nugent, P., et al., *Porous materials with optimal adsorption thermodynamics and kinetics for CO2 separation.* Nature, 2013. **495**(7439): p. 80-4.

114. Pham, T., et al., *Theoretical Investigations of CO2and H2Sorption in an Interpenetrated Square-Pillared Metal–Organic Material.* The Journal of Physical Chemistry C, 2013. **117**(19): p. 9970-9982.

115. Eddaoudi, M., et al., *Systematic design of pore size and functionality in isoreticular MOFs and their application in methane storage.* Science, 2002. **295**(5554): p. 469-72.

116. Zhao, D., et al., *Tuning the topology and functionality of metal-organic frameworks by ligand design.* Acc Chem Res, 2011. **44**(2): p. 123-33.

117. Bunck, D.N. and W.R. Dichtel, *Mixed linker strategies for organic framework functionalization.* Chemistry, 2013. **19**(3): p. 818-27.

118. Gul, E.N.F., et al., *Effects of varying water adsorption on a Cu3(BTC)2 metal-organic framework (MOF) as studied by 1H and 13C solid-state NMR spectroscopy.* Phys Chem Chem Phys, 2011. **13**(17): p. 7783-8.

119. Poloni, R., B. Smit, and J.B. Neaton, *Ligand-assisted enhancement of CO2 capture in metal-organic frameworks.* J Am Chem Soc, 2012. **134**(15): p. 6714-9.

120. Grajciar, L., et al., *Controlling the Adsorption Enthalpy of CO(2) in Zeolites by Framework Topology and Composition.* ChemSusChem, 2012. **5**: p. 2011-22.

121. Férey, G., et al., *A chromium terephthalate-based solid with unusually large pore volumes and surface area.* Science, 2005. **309**(5743): p. 2040-2.

122. Demessence, A., et al., *Strong CO2 binding in a water-stable, triazolate-bridged metal-organic framework functionalized with ethylenediamine.* J Am Chem Soc, 2009. **131**(25): p. 8784-6.

123. Li, J.R., et al., *Porous materials with pre-designed single-molecule traps for CO(2) selective adsorption.* Nat Commun, 2013. **4**: p. 1538.

124. Wriedt, M., et al., *Low-energy selective capture of carbon dioxide by a pre-designed elastic single-molecule trap.* Angew Chem Int Ed Engl, 2012. **51**(39): p. 9804-8.

125. Wriedt, M., et al., *Unprecedented activation and CO2 capture properties of an elastic single-molecule trap.* Chemical communications (Cambridge, England), 2013. **49**: p. 9612-4.

126. Yu, J. and P.B. Balbuena, *Water Effects on Postcombustion CO2Capture in Mg-MOF-74.* The Journal of Physical Chemistry C, 2013. **117**(7): p. 3383-3388.

127. Kizzie, A.C., A.G. Wong-Foy, and A.J. Matzger, *Effect of humidity on the performance of microporous coordination polymers as adsorbents for CO2 capture.* Langmuir, 2011. **27**(10): p. 6368-73.

128. Liu, J., et al., *CO2/H2O adsorption equilibrium and rates on metal-organic frameworks: HKUST-1 and Ni/DOBDC.* Langmuir, 2010. **26**(17): p. 14301-7.

129. Liu, J., et al., *Selective CO2 Capture from Flue Gas Using Metal–Organic Frameworks—A Fixed Bed Study.* The Journal of Physical Chemistry C, 2012. **116**(17): p. 9575-9581.

130. Liu, Q., et al., *Adsorption of Carbon Dioxide by MIL-101(Cr): Regeneration Conditions and Influence of Flue Gas Contaminants.* Scientific reports, 2013. **3**: p. 2916.

131. Soubeyrand-Lenoir, E., et al., *How water fosters a remarkable 5-fold increase in low-pressure CO2 uptake within mesoporous MIL-100(Fe).* J Am Chem Soc, 2012. **134**(24): p. 10174-81.

132. Ho, L.N., et al., *Gas Uptake in Solvents Confined in Mesopores: Adsorption versus Enhanced Solubility.* Journal of Physical Chemistry Letters, 2013. **4**(14): p. 2274-2278.

133. Sathre, R. and E. Masanet, *Prospective life-cycle modeling of a carbon capture and storage system using metal–organic frameworks for CO2 capture.* RSC Advances, 2013. **3**(15): p. 4964.

134. Choi, S., et al., *Modification of the Mg/DOBDC MOF with Amines to Enhance CO2 Adsorption from Ultradilute Gases.* Journal of Physical Chemistry Letters, 2012. **3**(9): p. 1136-1141.

135. McDonald, T.M., et al., *Capture of carbon dioxide from air and flue gas in the alkylamine-appended metal-organic framework mmen-Mg2(dobpdc).* J Am Chem Soc, 2012. **134**(16): p. 7056-65.

136. Planas, N., et al., *The mechanism of carbon dioxide adsorption in an alkylamine-functionalized metal-organic framework.* J Am Chem Soc, 2013. **135**(20): p. 7402-5.

137. Cao, Y., et al., *Capture of carbon dioxide from flue gas on TEPA-grafted metal-organic framework Mg2(dobdc).* Journal of Environmental Sciences, 2013. **25**: p. 2081-2087.

138. Chew, T.L., A.L. Ahmad, and S. Bhatia, *Ordered mesoporous silica (OMS) as an adsorbent and membrane for separation of carbon dioxide (CO2).* Adv Colloid Interface Sci, 2010. **153**(1-2): p. 43-57.

139. Bollini, P., et al., *Oxidative Degradation of Aminosilica Adsorbents Relevant to Postcombustion CO2Capture.* Energy & Fuels, 2011. **25**(5): p. 2416-2425.

140. Lau, C.H., R. Babarao, and M.R. Hill, *A route to drastic increase of CO2 uptake in Zr metal organic framework UiO-66.* Chem Commun (Camb), 2013. **49**(35): p. 3634-6.

141. Vuong, G.T., M.H. Pham, and T.O. Do, *Synthesis and engineering porosity of a mixed metal Fe2Ni MIL-88B metal-organic framework.* Dalton Trans, 2013. **42**(2): p. 550-7.

142. Kim, M., et al., *Postsynthetic ligand exchange as a route to functionalization of 'inert' metal–organic frameworks.* Chemical Science, 2012. **3**(1): p. 126.

143. Yan, X., et al., *Extremely enhanced CO2 uptake by HKUST-1 metal–organic framework via a simple chemical treatment.* Microporous and Mesoporous Materials, 2014. **183**: p. 69-73.

144. Lu, W., et al., *Building multiple adsorption sites in porous polymer networks for carbon capture applications.* Energy & Environmental Science, 2013. **6**: p. 3559.

145. Lu, W., et al., *Polyamine-tethered porous polymer networks for carbon dioxide capture from flue gas.* Angewandte Chemie (International ed. in English), 2012. **51**: p. 7480-4.

146. Lu, W.G., et al., *Carbon Dioxide Capture from Air Using Amine-Grafted Porous Polymer Networks.* Journal of Physical Chemistry C, 2013. **117**(8): p. 4057-4061.

147. Goesten, M.G., et al., *Chloromethylation as a functionalisation pathway for metal–organic frameworks.* CrystEngComm, 2012. **14**(12): p. 4109.

148. Bernt, S., et al., *Direct covalent post-synthetic chemical modification of Cr-MIL-101 using nitrating acid.* Chemical communications (Cambridge, England), 2011. **47**: p. 2838-40.

149. Sculley, J.P., et al., *High-throughput analytical model to evaluate materials for temperature swing adsorption processes.* Advanced materials (Deerfield Beach, Fla.), 2013. **25**: p. 3957-61.

150. Babarao, R., S. Dai, and D.E. Jiang, *Functionalizing porous aromatic frameworks with polar organic groups for high-capacity and selective CO2 separation: a molecular simulation study.* Langmuir, 2011. **27**(7): p. 3451-60.

151. Tranchemontagne, D.J., et al., *Secondary building units, nets and bonding in the chemistry of metal-organic frameworks.* Chem Soc Rev, 2009. **38**(5): p. 1257-83.

152. Férey, G., *Hybrid porous solids: past, present, future.* Chem Soc Rev, 2008. **37**(1): p. 191-214.

153. Yaghi, O.M., et al., *Reticular synthesis and the design of new materials.* Nature, 2003. **423**(6941): p. 705-14.

154. Férey, G., et al., *A Hybrid Solid with Giant Pores Prepared by a Combination of Targeted Chemistry, Simulation, and Powder Diffraction.* Angewandte Chemie, 2004. **116**(46): p. 6456-6461.

155. Furukawa, H., et al., *Isoreticular expansion of metal-organic frameworks with triangular and square building units and the lowest calculated density for porous crystals.* Inorg Chem, 2011. **50**(18): p. 9147-52.

156. Zhao, D., et al., *Stabilization of metal-organic frameworks with high surface areas by the incorporation of mesocavities with microwindows.* J Am Chem Soc, 2009. **131**(26): p. 9186-8.

157. Song, L., et al., *Mesoporous metal–organic frameworks: design and applications.* Energy & Environmental Science, 2012. **5**(6): p. 7508.

158. Jansen, M. and J.C. Schon, *"Design" in chemical synthesis--an illusion?* Angew Chem Int Ed Engl, 2006. **45**(21): p. 3406-12.

159. Goesten, M.G., F. Kapteijn, and J. Gascon, *Fascinating chemistry or frustrating unpredictability: observations in crystal engineering of metal–organic frameworks.* CrystEngComm, 2013. **15**: p. 9249.

CHAPTER 6

CONCLUSIONS

6.1 Summary, Conclusions, and Recommendations

6.1.1 *Chapter 3 – Tuning the Adsorption Properties of UiO-66 via Ligand Substitution*

The effect of functionalization on the adsorption properties of MOFs was studied in a series of isostructural materials. In order to conduct a study relevant to general applications, this work was limited to a series of materials known to be stable in ambient air. The UiO-66 series of MOFs is ideally suited as the materials are highly stable and can be synthesized with a number of functionalized linkers to yield isostructural materials.

Results indicate that all gases tested show improved adsorption in UiO-66-NH_2, but CO_2 is most enhanced resulting in higher selectivity as predicted by IAST. Unfunctionalized UiO-66 possesses good CO_2:CH_4 selectivity, thus the selectivity and uptake enhancement induced by addition of an amino functionality to the pores is not as great for UiO-66 as is observed in other isoreticular series of materials. This indicates that the entire family of UiO-66 possesses a common pore feature which provides strong adsorption interactions. Addition of functional groups provides additional interactions which lead to smaller selectivity enhancements relative to other materials where the functional group is the sole source of strong interactions. These adsorption sites common to the UiO-66 series are attributed to the $Zr_6O_4(OH)_4$ cluster where hydroxyls are exposed to the pore space, provide strong interactions, and their presence is independent of the organic linker.

The amino, nitro, and dimethoxy functionalized materials all show nearly overlapping isotherms for CO_2 at low pressures (<1 bar). This indicates that an additional polar functional group will improve low pressure adsorption in UiO-66 regardless of size or polarity. This is attributed to the position of the functional group within the pore space and proximity to the hydroxyls of the metal cluster, where the polar group provides a second strong point of interaction for the CO_2 molecule.

Since CH_4 and N_2 have no dipole moment, adsorption enhancement is governed almost entirely due to dispersive and dispersive-dipole interactions. For these two gases, the strongest enhancement is found with the smallest, most polar functional group found in UiO-66-NH_2. The other functionalized materials show lower uptake due to the additional framework mass of the bulkier functional groups, which offsets the increased interactions.

All three polar groups lead to enhanced water adsorption and ultimately pore filling at low relative humidity (RH). The unfunctionalized UiO-66 material shows a step isotherm where pore filling occurs above 20% RH. The naphthyl functionalized material shows no step, indicating an inhibition of pore filling. Pore filling is undesirable as it may cause nearly complete exclusion of other gas adsorbates and thus an adsorption system would require significant dehydration, which adds cost and reduces efficiency.

UiO-66-2,5-$(OMe)_2$ shows higher water vapor uptake than the materials with smaller functionalities. Previously, this was attributed to a packing efficiency in the pore space induced by the methoxy functional groups but not provided by amino or nitro groups. Another explanation is that the methoxy material, which is synthesized with an acetic acid modulator, has stabilized missing linker defects which lead to more pore

volume for water adsorption. The pore volume increase was not observed via cryogenic N_2 measurements as it was assumed to be obscured by external particle effects caused by aggregation.

Conclusions drawn from this work indicate that UiO-66 is not a perfectly ideal material for studying the effect of functional groups without other factors of influence. This material and its isostructural family are interesting due to the multiple points of interaction for CO_2 at adsorption sites in proximity to the metal cluster. The best enhancement for CO_2 adsorption is found with the small, polar amino functionality, but this and other polar functionalities also lead to significantly stronger water vapor adsorption and pore filling at low relative humidity. For humid adsorption applications, the parent material and the naphthyl functionalized material may produce interesting results.

Recommendations for continued research into the effects of functional groups on adsorption properties include humid gas adsorption, mixture adsorption, and breakthrough studies. Among other stable series of MOFs, MIL-53 and various ZIF materials, are good candidates for study. Due to the cost of the linkers, metals, and solvents, it is recommended that future work also focus on how to improve adsorbent utilization and explore methods of cost reduction.

6.1.2 *Chapter 4 – Micro-Bed Breakthrough Study an a Set of Stable MOFs*

A series of stable MOFs with representative pore features were studied for mixture adsorption properties. A breakthrough study was conducted using a set of industrially relevant mixtures and the materials were selected to be representative of certain pore features. UiO-66 and UiO-66-NH_2 were selected for the small pores and

good adsorption at low pressures and to compare the effect of the additional polar amino functionality. UiO-66-2,5-Dimethyl was selected due to its interesting combination of good adsorption at low pressures and partial hydrophobicity. NH_2-MIL-101(Al) was selected for its combination of stability, large pores, amino functional groups, lightweight and low cost aluminum metal centers, and open-metal sites. Finally, zeolite NaY, a well-studied material, was selected as a standard.

These five materials were tested in a breakthrough apparatus with 5 dry gas mixtures and two pure component streams. Two mixtures of N_2 and CO_2 are representative of dry flue gas while the other three span a range of CH_4 and CO_2 compositions. The pure component experiments are CO_2 and CH_4 in a Helium carrier stream. The sample sizes are on the scale of a single synthesis batch, a potentially critical factor for studying expensive or synthetically challenging materials. Dynamic capacity is calculated at the time of 5% of inlet concentration breakthrough. Simulations are qualitatively matched to the results in order to verify the results are consistent. A number of unexpected challenges inherent to the instrument are overcome by applying corrections in an automated and self-consistent manner with custom code. The corrected plots are used to observe trends between samples and compare with simulations.

The results of this study provide a good indication of the trends between these materials. As is expected in a dry gas stream, zeolite NaY outperforms each of the MOFs tested by roughly doubling the breakthrough time of the best MOF, UiO-66-NH_2. UiO-66-NH_2 and UiO-66-DM perform similarly for breakthrough time, but batch-to-batch variations appear to have a significant role in the results which is not predicted from BET or pXRD measurements. UiO-66-NH_2 slightly outperforms and UiO-66-DM

significantly outperforms predictions based on isotherms obtained from literature. A re-evaluation of UiO-66-DM by single component equilibrium isotherm measurement shows that this batch has much better CO_2 adsorption performance than published results. Also, IAST is shown to provide a poor estimate for breakthrough times and dynamic capacities.

This work indicates that UiO-66-DM may be a good candidate for further study due to the combination of partial hydrophobicity and performance approaching UiO-66-NH_2. Both of these materials significantly outperform UiO-66. The two pore features for NH_2-MIL-101(Al) which are associated with high performance in other materials, are shown to have minimal impact on breakthrough time, primarily due to the large pore size and low density of these features.

Recommendations for continued research include study of humid breakthrough in order to approach more realistic conditions. Additionally, analysis of desorption data would provide information on the equally important regeneration stage of adsorption cycles.

6.1.3 *Chapter 5 – Design of Optimal MOFs for Carbon Capture*

Although the goal of producing a single material which can successfully capture carbon dioxide from humid flue gas in an energy efficient manner has yet to be reached, significant progress has been made on many facets of the problem. Numerous approaches are under consideration, so a narrow focus on the design of MOFs and what target pore features currently show great potential for success is the subject of this work. After outlining the problem and framing what options are realistic, a set of pore features

are schematically proposed. These features are based on connections between results from various published works as well as previous works in this dissertation.

The framed problem is capturing carbon dioxide from humid flue gas for carbon capture and storage purposes. Other adsorbents already exist which can effectively and efficiently do this separation if the gas stream is completely dry or if temperature swing adsorption cycles are viable. Dehumidification of flue gas is too expensive and no TSA cycle currently exists to reach purity requirements. Therefore an adsorbent which is water tolerant and optimal for PSA cycles is the target.

The proposed route to utilizing MOFs for successful and energy efficient carbon capture from large point sources begins with stability. Stability is summarized as a reversible reaction and considered to be either kinetically or thermodynamically controlled. Other works which have targeted portions of this are used as a basis for proposing what materials are most stable. These materials are based on metal centers with very slow ligand exchange rates, such as Cr^{+3} or Al^{+3}, and have high framework connectivity, which prevents collapse from displacement of single ligands.

The next factor is cost and safety of the materials. MOFs are currently at least three orders of magnitude more expensive than zeolites, currently the best class of materials for carbon capture. Additionally, many MOFs use hazardous metals and solvents, require high purity reagents, and generate significant waste. Third, MOFs in a powder form are likely to be an inhalation and dust hazard. In order to overcome these problems, reagent selection needs to be a primary factor and further importance needs to be placed on the proper handling of these materials. Fortunately, evidence suggests that

many MOFs are structurally robust can be pelletized without binder to form strong pellets.

The third factor is adsorbent utilization. For material properties, regenerability and rapid kinetics are essential, while for macro-scale adsorbent design, temperature control and rapid cycle optimization would yield improvements. MOFs provide a route to minimizing kinetic limitations, due to linker rotation and bending, and a moderate heat of adsorption while maintaining performance. Additionally, MOF synthesis enables new route to engineered sorbent design and implementation.

Finally, the most important factor is adsorbent performance in mixed, humid gas streams. One of the key phenomena in adsorption is pore filling at low relative humidity, which can be avoided by preventing strong water adsorption and subsequent clustering. The challenge is developing an adsorbent which can inhibit pore filling while maintaining effective CO_2 affinity. With the wide variety of known structures and synthesis methods, it is possible to make certain MOFs with specific pore features such as hydrophobic channels with size-matched adsorption sites for CO_2. Alternatively, taking the ability to tailor organic linkers to create specific pore shapes can allow for designed cooperative adsorption sites for H_2O and CO_2. Finally, post-synthetic modification can enable pore structures unattainable by direct synthesis methods and in other material classes.

6.2 Overall Conclusions

The overarching theme of this work is the observation and understanding of modifying the pore features of MOFs for adsorption applications. The primary target was development of a stable MOF synthesized with commercially available reagents which

shows good performance for CO_2 adsorption under flue gas conditions. Although such a uniquely challenging material was not discovered, the results and underlying work reveal a number of trends which help advance the understanding of adsorption in MOFs. Additionally, a unique niche where MOFs may solve the problem of carbon capture from large point source was identified and the pore features which can possibly produce a viable CCS adsorbent were proposed.

6.3 Recommendations for Future Work

One of the major challenges facing adsorbent characterization remains determination of mixture separation performance. Two major targets exist that became apparent during the course of this work. First, humid gas adsorption requires unique tools and equipment for proper measurement. Second, there is a need to use breakthrough measurements to both characterize the adsorptive separation potential of a material, but also the desorption and thermal characteristics.

Humid gas breakthrough adsorption requires additional care for accurate measurement of both CO_2 and water, particularly the long time required for water saturation. As the available number of viable MOF materials continues to grow without significant information on the CO_2 adsorption performance under humid conditions, a new instrument is needed. A breakthrough instrument which can measure water-CO_2 co-adsorption on small samples would be ideal. This would allow for study on numerous samples which have yet to be scaled up or are difficult to synthesize. By broadening the available spectrum of MOFs, more pore features can be tested and more accurate observations can be made.

Cyclic adsorption operations require information about the adsorption, desorption, and thermal behavior. The latter two require additional care during instrument design and sample preparation, especially when working with small samples. The optimal goal would be to measure desorption under reduced pressure and adiabatic conditions in order to best approximate real PSA operations.

APPENDIX A

RAW DATA

A.1 Chapter 3: Tuning the Adsorption Properties of UiO-66 via Ligand Functionalization

Table A.1. BET surface areas

Material Name	BET surface area (m^2/g)
UiO-66	1120, 1089
UiO-66-1,4-Naphthyl	766, 747
UiO-66-NH_2	1187, 1059
UiO-66-NO_2	765, 819
UiO-66-2,5-$(OMe)_2$	899, 837

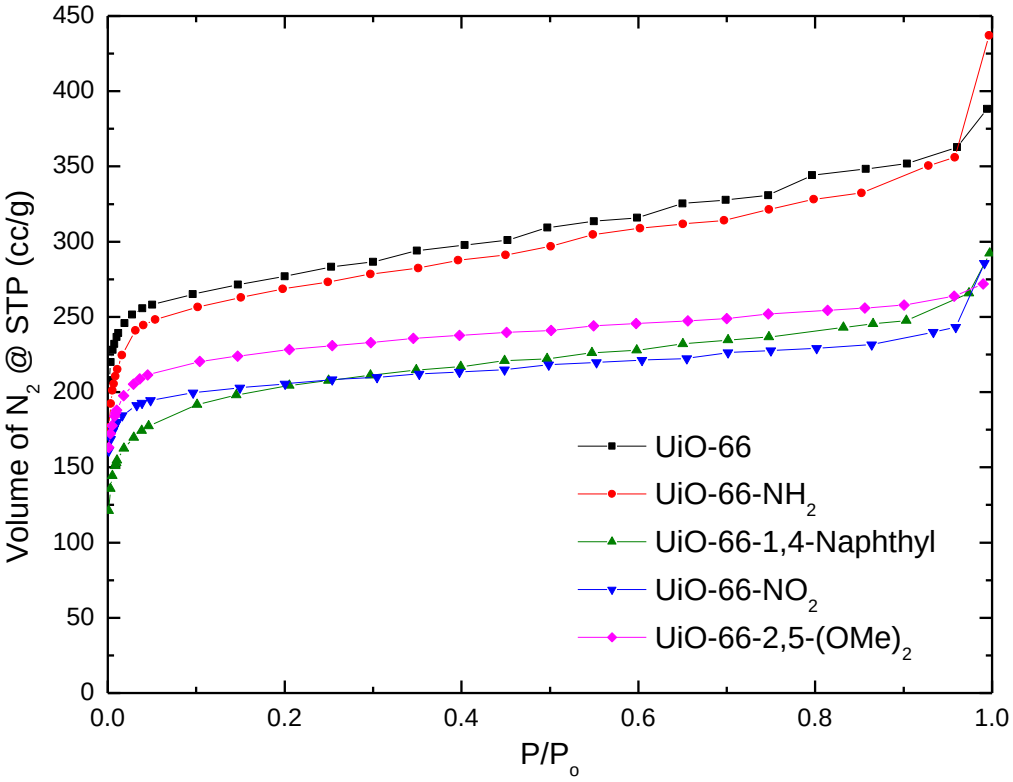

Figure A.1. Nitrogen adsorption isotherms at 77K.

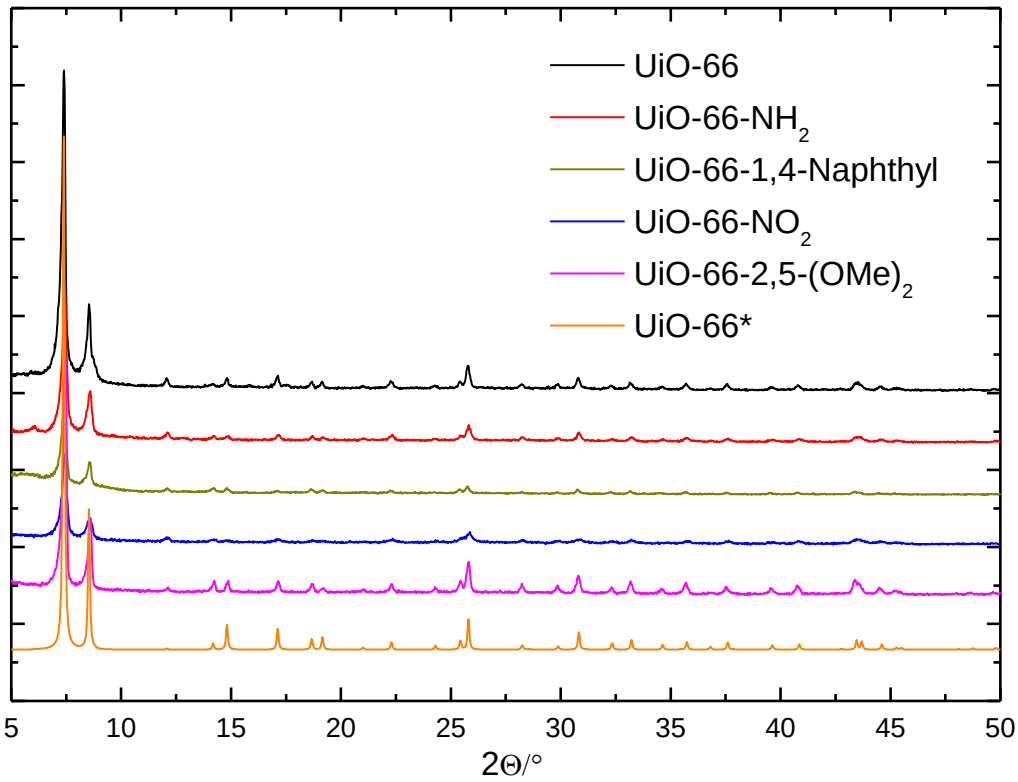

Figure A.2. Powder XRD patterns. Reference PXRD pattern (UiO-66*) provided for comparison.

Table A.2. Organic ligands and synthesis procedures used for each material

Material	UiO-66	UiO-66-NO_2	UiO-66-NH_2	UiO-66-1,4-Naph	UiO-66-2,5-$(OMe)_2$
Image	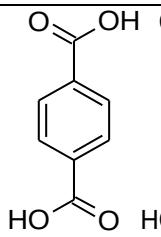	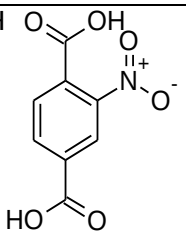	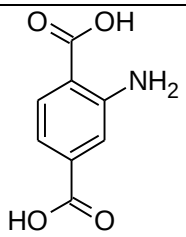	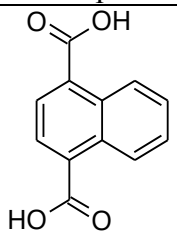	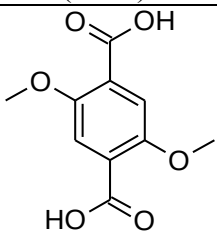
Chemical Name	Terephtha-lic Acid	2-Nitro-Terephthalic Acid	2-Amino-Terephthalic Acid	1,4-Naphthalene Dicarboxylic Acid	2,5-Dimethoxy-Terephthalic Acid
Organic Linker	0.35 mmol	0.35 mmol	0.35 mmol	0.35 mmol	0.35 mmol
$ZrCl_4$	0.35 mmol	0.35 mmol	0.368 mmol	0.35 mmol	0.35 mmol
DMF	4 mL	4 mL	4 mL	4 mL	4 mL
Acetic Acid	0 mL	0 mL	0 mL	0 mL	0.6 mL
Temperature	120 °C	120 °C	120 °C	120 °C	110 °C
Time	24 hr	24 hr	24 hr	24 hr	48 hr

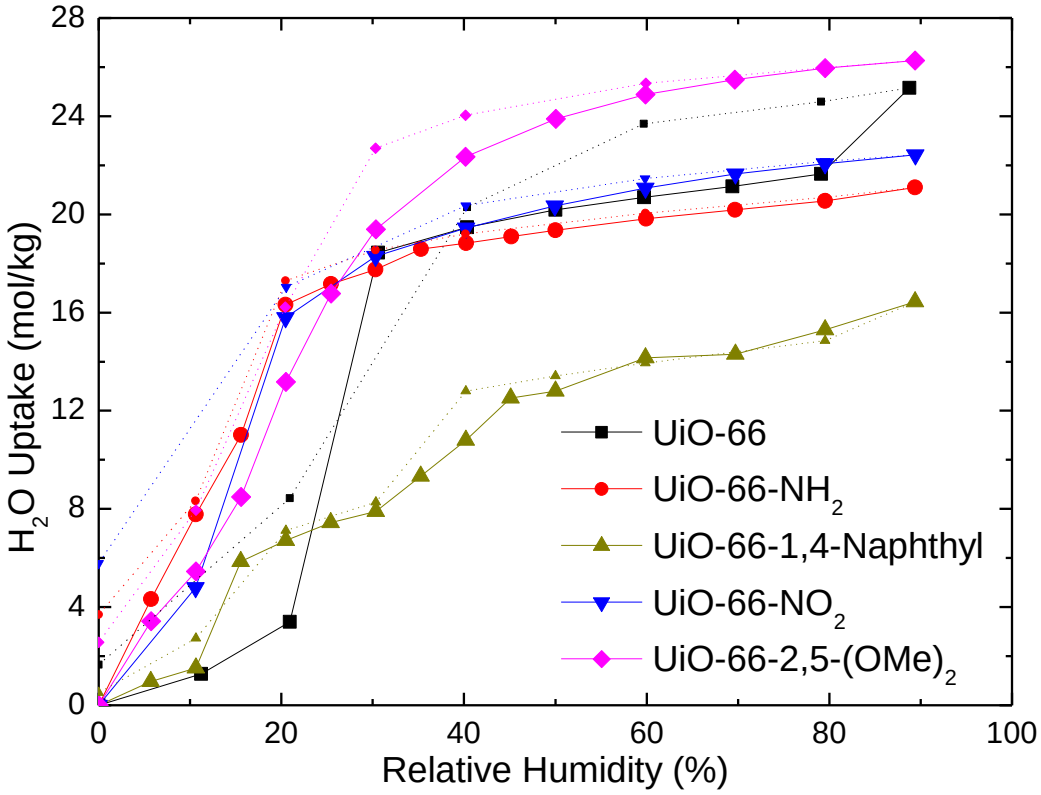

Figure A.3. Water Vapor adsorption and desorption isotherms at 298K

Table A.3. CO_2 High Pressure Adsorption Isotherms at 298K

UiO-66		UiO-66-NH_2		UiO-66-1,4-Naph		UiO-66-NO_2		UiO-66-2,5-$(OMe)_2$	
Pressure Bar	CO_2 Capacity Mol/kg	Pressure Bar	CO_2 Capacity Mol/kg	Pressure Bar	CO_2 Capacity Mol/kg	Pressure Bar	CO_2 Capacity Mol/kg	Pressure Bar	CO_2 Capacity Mol/kg
0.000	0.000	0.000	0.000	0.000	0.000	0.000	0.000	0.000	0.000
0.024	0.119	0.013	0.118	0.025	0.098	0.014	0.132	0.013	0.117
0.208	0.598	0.198	1.168	0.225	0.560	0.199	1.058	0.198	1.056
0.408	0.985	0.401	1.820	0.413	0.864	0.400	1.628	0.401	1.638
0.602	1.285	0.599	2.279	0.600	1.109	0.599	2.022	0.601	2.044
0.804	1.550	0.798	2.654	0.808	1.343	0.801	2.328	0.800	2.365
1.008	1.786	1.000	2.973	1.003	1.537	0.999	2.573	1.002	2.631
1.197	1.980	1.198	3.245	1.207	1.718	1.198	2.777	1.200	2.862
1.410	2.180	1.398	3.489	1.396	1.871	1.399	2.951	1.401	3.060
1.609	2.353	1.600	3.710	1.604	2.022	1.599	3.104	1.600	3.232
1.803	2.510	1.798	3.907	1.806	2.156	1.798	3.237	1.800	3.388
2.007	2.667	1.997	4.090	2.003	2.275	1.999	3.358	1.999	3.534
4.998	4.242	4.997	5.829	4.997	3.498	4.997	4.377	4.997	4.822
9.994	5.707	9.995	7.284	9.992	4.735	9.991	5.096	9.999	5.869
14.993	6.532	14.990	8.026	14.988	5.622	14.988	5.473	14.992	6.438
19.986	7.033	19.989	8.406	19.998	6.320	19.985	5.723	20.003	6.737

Table A.4. CH_4 High Pressure Adsorption Isotherms at 298K

UiO-66		UiO-66-NH_2		UiO-66-1,4-Naph		UiO-66-NO_2		UiO-66-2,5-$(OMe)_2$	
Pressure Bar	CH_4 Capacity Mol/kg	Pressure Bar	CH_4 Capacity Mol/kg	Pressure Bar	CH_4 Capacity Mol/kg	Pressure Bar	CH_4 Capacity Mol/kg	Pressure Bar	CH_4 Capacity Mol/kg
0.000	0.000	0.000	0.000	0.000	0.000	0.000	0.000	0.000	0.000
0.212	0.128	0.012	0.011	0.022	0.016	0.014	0.010	0.019	0.026
0.413	0.232	0.201	0.167	0.207	0.112	0.199	0.176	0.198	0.142
0.606	0.326	0.401	0.311	0.405	0.206	0.400	0.325	0.409	0.268
0.802	0.411	0.601	0.440	0.605	0.292	0.600	0.455	0.603	0.390
1.001	0.493	0.800	0.557	0.805	0.371	0.800	0.571	0.806	0.506
1.506	0.679	0.999	0.665	1.010	0.449	0.999	0.676	1.003	0.600
2.003	0.845	1.498	0.904	1.508	0.608	1.498	0.901	1.504	0.801
4.997	1.592	1.998	1.113	2.006	0.751	1.999	1.091	2.005	0.976
9.995	2.407	4.997	2.024	4.999	1.357	4.995	1.846	4.998	1.685
14.995	2.968	9.994	2.940	9.993	1.989	9.995	2.525	9.995	2.426
19.991	3.399	14.994	3.566	14.999	2.385	15.004	2.940	14.995	2.910
		19.997	4.005	19.994	2.678	20.002	3.270	19.995	3.275

Table A.5. N_2 Adsorption Isotherms at 298K

UiO-66		UiO-66-NH_2		UiO-66-1,4-Naph		UiO-66-NO_2		UiO-66-2,5-$(OMe)_2$	
Pressure Bar	N_2 Capacity Mol/kg	Pressure Bar	N_2 Capacity Mol/kg	Pressure Bar	N_2 Capacity Mol/kg	Pressure Bar	N_2 Capacity Mol/kg	Pressure Bar	N_2 Capacity Mol/kg
0.000	0.000	0.000	0.000	0.000	0.000	0.000	0.000	0.000	0.000
0.013	0.004	0.012	0.016	0.013	0.005	0.013	0.004	0.014	0.012
0.199	0.042	0.198	0.060	0.199	0.025	0.200	0.034	0.198	0.056
0.399	0.071	0.400	0.103	0.400	0.060	0.399	0.064	0.400	0.088
0.598	0.101	0.598	0.144	0.597	0.077	0.598	0.093	0.597	0.115
0.799	0.128	0.800	0.184	0.799	0.098	0.799	0.122	0.799	0.153
0.999	0.155	1.000	0.223	0.998	0.121	1.000	0.150	1.000	0.195
1.498	0.216	1.197	0.260	1.197	0.140	1.500	0.214	1.197	0.225
1.997	0.274	1.398	0.296	1.398	0.163	1.997	0.274	1.398	0.258
4.996	0.567	1.598	0.331	1.598	0.182	4.997	0.567	1.598	0.288
9.996	0.924	1.797	0.366	1.797	0.200	9.995	0.878	1.797	0.314
14.996	1.201	1.998	0.399	1.997	0.220	14.996	1.090	1.997	0.341
19.994	1.419	2.999	0.553	2.999	0.312	19.991	1.246	3.000	0.468

Table A.6. CO_2 Isotherms and Toth model fitting parameters UiO-66

	UiO-66					
	298K		308K		318K	
	P (bar)	n(mol CO_2/kg)	P (bar)	n(mol CO_2/kg)	P (bar)	n(mol CO_2/kg)
	0.000	0.000	0.000	0.000	0.000	0.000
	0.022	0.106	0.414	0.757	0.408	0.609
	0.204	0.563	0.608	1.000	0.609	0.818
	0.402	0.942	0.812	1.224	0.809	1.005
	0.611	1.264	1.005	1.413	1.009	1.171
	0.806	1.521	1.202	1.589	1.205	1.330
	1.004	1.750	1.401	1.753	1.408	1.474
	1.211	1.966	1.604	1.912	1.607	1.611
	1.406	2.151	1.806	2.057	1.807	1.742
	1.608	2.328	2.003	2.189	2.007	1.857
	1.805	2.491	3.004	2.761	3.007	2.367
	2.006	2.644				
	3.002	3.281				
	value	std dev	value	std dev	value	std dev
q_i^{sat}	18.080	1.749	18.032	0.959	16.576	2.381
b	0.284	0.014	0.200	0.006	0.158	0.014
t	0.426	0.019	0.431	0.010	0.450	0.027
R^2	99.9960%		99.9990%		99.9940%	

Table A.7. CO_2 Isotherms and Toth model fitting parameters UiO-66-NH_2

UiO-66-NH_2						
298K		308K		318K		
P (bar)	n(mol CO_2/kg)	P (bar)	n(mol CO_2/kg)	P (bar)	n(mol CO_2/kg)	
0.000	0.000	0.000	0.000	0.000	0.000	
0.027	0.304	0.055	0.466	0.105	0.559	
0.054	0.523	0.104	0.711	0.202	0.867	
0.103	0.848	0.202	1.102	0.301	1.127	
0.202	1.330	0.301	1.409	0.402	1.349	
0.302	1.693	0.402	1.669	0.597	1.703	
0.402	1.983	0.597	2.069	0.798	2.002	
0.597	2.427	0.798	2.398	0.998	2.253	
0.798	2.790	0.998	2.673	1.197	2.474	
0.998	3.085	1.197	2.913	1.398	2.680	
1.197	3.339	1.397	3.125	1.598	2.855	
1.397	3.558	1.598	3.320	1.797	3.025	
1.598	3.755	1.797	3.492	1.997	3.177	
1.797	3.933	1.997	3.651	2.998	3.753	
1.997	4.094	2.998	4.277			
2.998	4.729					
298K		308K		318K		
value	std dev	value	std dev	value	std dev	
q_i^{sat}	11.605	0.318	14.907	0.368	13.599	0.819
b	1.675	0.022	1.261	0.010	0.823	0.014
t	0.443	0.009	0.379	0.005	0.409	0.014
R^2	99.9970%		99.9990%		99.9950%	

Table A.8. CO_2 Isotherms and Toth model fitting parameters UiO-66-1,4-Naphthyl

UiO-66-1,4-Naphthyl						
	298K		308K		318K	
	P (bar)	n(mol CO_2/kg)	P (bar)	n(mol CO_2/kg)	P (bar)	n(mol CO_2/kg)
	0.000	0.000	0.000	0.000	0.000	0.000
	0.023	0.090	0.060	0.142	0.059	0.112
	0.063	0.207	0.110	0.231	0.111	0.185
	0.088	0.274	0.211	0.399	0.216	0.317
	0.225	0.560	0.319	0.549	0.315	0.425
	0.413	0.864	0.411	0.663	0.414	0.523
	0.600	1.109	0.603	0.869	0.602	0.691
	0.808	1.343	0.806	1.058	0.805	0.847
	1.003	1.537	1.002	1.221	1.003	0.992
	1.207	1.718	1.205	1.372	1.201	1.119
	1.396	1.871	1.405	1.507	1.402	1.235
	1.604	2.022	1.607	1.637	1.597	1.337
	1.806	2.156	1.801	1.752	1.803	1.440
	2.003	2.275	2.005	1.865	2.007	1.549
	4.997	3.498	3.006	2.341	3.010	1.962
	298K		308K		318K	
	value	std dev	value	std dev	value	std dev
q_i^{sat}	11.597	0.351	14.602	0.652	15.132	1.498
b	0.404	0.004	0.235	0.006	0.168	0.011
t	0.456	0.008	0.420	0.008	0.413	0.016
R^2	99.9980%		99.9990%		99.9970%	

Table A.9. CO_2 Isotherms and Toth model fitting parameters UiO-66-NO_2

UiO-66-NO_2						
298K		308K		318K		
P (bar)	n(mol CO_2/kg)	P (bar)	n(mol CO_2/kg)	P (bar)	n(mol CO_2/kg)	
0.000	0.000	0.000	0.000	0.000	0.000	
0.023	0.132	0.023	0.091	0.024	0.070	
0.053	0.260	0.054	0.194	0.054	0.139	
0.104	0.444	0.104	0.329	0.106	0.252	
0.198	0.710	0.202	0.549	0.201	0.421	
0.302	0.941	0.298	0.726	0.298	0.568	
0.401	1.126	0.398	0.884	0.399	0.700	
0.597	1.422	0.598	1.145	0.598	0.922	
0.797	1.663	0.798	1.359	0.797	1.111	
0.999	1.865	0.999	1.542	0.998	1.274	
1.197	2.034	1.196	1.700	1.197	1.423	
1.398	2.183	1.397	1.842	1.397	1.552	
1.597	2.318	1.598	1.971	1.598	1.665	
1.797	2.439	1.797	2.077	1.797	1.774	
1.997	2.551	1.997	2.190	1.997	1.863	
2.998	3.004	2.998	2.602	2.998	2.256	
	298K		308K		318K	
	value	std dev	value	std dev	value	std dev
q_i^{sat}	7.733	0.188	6.954	0.102	6.325	0.157
b	1.009	0.009	0.696	0.004	0.509	0.006
t	0.485	0.008	0.527	0.005	0.564	0.009
R^2	99.9980%		99.9980%		99.9980%	

Table A.10. CO_2 Isotherms and Toth model fitting parameters UiO-66-2,5-$(OMe)_2$

UiO-66-2,5-$(OMe)_2$						
298K		308K		318K		
P (bar)	n(mol CO_2/kg)	P (bar)	n(mol CO_2/kg)	P (bar)	n(mol CO_2/kg)	
0.000	0.000	0.000	0.000	0.000	0.000	
0.013	0.131	0.203	0.840	0.198	0.624	
0.198	1.071	0.398	1.310	0.399	1.031	
0.400	1.652	0.598	1.670	0.598	1.342	
0.599	2.064	0.798	1.962	0.797	1.600	
0.799	2.387	1.000	2.209	1.000	1.822	
0.998	2.651	1.197	2.417	1.197	2.012	
1.197	2.876	1.399	2.605	1.396	2.182	
1.399	3.074	1.599	2.771	1.599	2.336	
1.597	3.245	1.796	2.919	1.798	2.475	
1.797	3.399	1.999	3.058	1.997	2.601	
1.999	3.540	2.998	3.602	2.999	3.111	
2.999	4.081					
298K		308K		318K		
value	std dev	value	std dev	value	std dev	
q_i^{sat}	8.973	0.241	9.638	0.199	8.298	0.442
b	1.388	0.020	0.907	0.006	0.638	0.011
t	0.504	0.012	0.487	0.007	0.543	0.021
R^2	99.9970%		99.9990%		99.9910%	

Table A.11. CH_4 Isotherms and Langmuir model fitting parameters UiO-66

UiO-66						
	298K		308K		318K	
	P (bar)	n(mol CH_4/kg)	P (bar)	n(mol CH_4/kg)	P (bar)	n(mol CH_4/kg)
	0.000	0.000	0.000	0.000	0.000	0.000
	0.021	0.019	0.211	0.113	0.411	0.162
	0.211	0.134	0.409	0.194	0.610	0.226
	0.410	0.233	0.606	0.273	0.813	0.286
	0.607	0.330	0.798	0.344	1.010	0.344
	0.810	0.419	1.009	0.417	1.210	0.396
	1.008	0.502	1.207	0.481	1.409	0.448
	1.205	0.580	1.408	0.543	1.608	0.497
	1.403	0.655	1.606	0.601	1.806	0.543
	1.607	0.727	1.807	0.658	2.005	0.591
	1.804	0.793	2.006	0.713	3.002	0.808
	2.004	0.861	3.004	0.960		
	2.999	1.146				
	298K		308K		318K	
	value	std dev	value	std dev	value	std dev
q_i^{sat}	3.173	0.098	2.727	0.121	2.527	0.145
b	0.187	0.008	0.178	0.011	0.154	0.011
R^2	99.961%		99.898%		99.847%	

Table A.12. CH_4 Isotherms and Langmuir model fitting parameters UiO-66-NH_2

	UiO-66-NH_2					
	298K		308K		318K	
	P (bar)	n(mol CH_4/kg)	P (bar)	n(mol CH_4/kg)	P (bar)	n(mol CH_4/kg)
	0.000	0.000	0.000	0.000	0.000	0.000
	0.024	0.032	0.107	0.116	0.106	0.084
	0.049	0.071	0.198	0.184	0.198	0.138
	0.106	0.134	0.298	0.256	0.299	0.194
	0.203	0.234	0.398	0.322	0.398	0.248
	0.298	0.323	0.598	0.440	0.597	0.345
	0.399	0.413	0.798	0.549	0.798	0.435
	0.597	0.559	0.999	0.649	0.999	0.518
	0.798	0.696	1.197	0.741	1.198	0.595
	0.998	0.817	1.398	0.826	1.397	0.668
	1.199	0.929	1.598	0.906	1.598	0.735
	1.397	1.031	1.797	0.982	1.797	0.798
	1.599	1.127	1.997	1.054	1.997	0.861
	1.797	1.216	2.998	1.363	2.999	1.141
	1.998	1.302				
	3.000	1.662				
	298K		308K		318K	
	value	std dev	value	std dev	value	std dev
q_i^{sat}	3.207	0.104	2.809	0.119	2.679	0.115
b	0.346	0.018	0.304	0.020	0.241	0.015
R^2	99.886%		99.823%		99.876%	

Table A.13. CH_4 Isotherms and Langmuir model fitting parameters UiO-66-1,4-Naphthyl

UiO-66-1,4-Naphthyl						
	298K		308K		318K	
	P (bar)	n(mol CH_4/kg)	P (bar)	n(mol CH_4/kg)	P (bar)	n(mol CH_4/kg)
	0.000	0.000	0.000	0.000	0.000	0.000
	0.014	0.012	0.014	0.012	0.201	0.074
	0.199	0.134	0.198	0.093	0.401	0.136
	0.399	0.240	0.401	0.174	0.598	0.198
	0.598	0.329	0.599	0.249	0.800	0.255
	0.798	0.421	0.800	0.321	0.999	0.310
	0.999	0.499	1.000	0.386	1.198	0.361
	1.198	0.576	1.198	0.449	1.399	0.410
	1.398	0.640	1.398	0.506	1.599	0.457
	1.598	0.696	1.599	0.561	1.797	0.501
	1.798	0.759	1.798	0.611	1.997	0.543
	1.998	0.856	1.999	0.671	2.997	0.734
	3.000	1.063	2.998	0.882		
	298K		308K		318K	
	value	std dev	value	std dev	value	std dev
q_i^{sat}	2.419	0.027	2.438	0.051	2.313	0.040
b	0.248	0.004	0.188	0.005	0.154	0.003
R^2	99.864%		99.982%		99.988%	

Table A.14. CH_4 Isotherms and Langmuir model fitting parameters UiO-66-NO_2

	UiO-66-NO_2					
	298K		308K		318K	
	P (bar)	n(mol CH_4/kg)	P (bar)	n(mol CH_4/kg)	P (bar)	n(mol CH_4/kg)
	0.000	0.000	0.000	0.000	0.000	0.000
	0.016	0.017	0.403	0.207	0.600	0.235
	0.204	0.149	0.597	0.287	0.800	0.297
	0.403	0.269	0.801	0.365	0.999	0.355
	0.604	0.373	1.002	0.436	1.199	0.409
	0.803	0.468	1.202	0.499	1.399	0.459
	1.002	0.549	1.401	0.558	1.599	0.507
	1.200	0.624	1.600	0.613	1.797	0.551
	1.402	0.695	1.798	0.665	1.999	0.598
	1.601	0.759	2.001	0.716	2.998	0.790
	1.800	0.820	2.998	0.931		
	2.000	0.877				
	2.998	1.118				
	298K		308K		318K	
	value	std dev	value	std dev	value	std dev
q_i^{sat}	2.257	0.050	2.131	0.048	2.029	0.059
b	0.321	0.011	0.255	0.008	0.211	0.009
R^2	99.954%		99.961%		99.953%	

Table A.15. CH_4 Isotherms and Langmuir model fitting parameters UiO-66-2,5-(OMe)$_2$

UiO-66-2,5-(OMe)$_2$						
	298K		308K		318K	
	P (bar)	n(mol CH_4/kg)	P (bar)	n(mol CH_4/kg)	P (bar)	n(mol CH_4/kg)
	0.000	0.000	0.000	0.000	0.000	0.000
	0.054	0.034	0.055	0.029	0.055	0.024
	0.107	0.064	0.107	0.052	0.107	0.042
	0.199	0.112	0.198	0.089	0.198	0.072
	0.299	0.163	0.301	0.129	0.300	0.103
	0.400	0.208	0.399	0.165	0.400	0.133
	0.600	0.291	0.600	0.233	0.598	0.187
	0.799	0.363	0.799	0.293	0.798	0.237
	0.998	0.429	0.999	0.348	0.998	0.283
	1.200	0.489	1.198	0.399	1.197	0.325
	1.398	0.544	1.399	0.446	1.398	0.365
	1.598	0.595	1.598	0.490	1.599	0.403
	1.797	0.644	1.798	0.534	1.798	0.441
	1.998	0.689	1.998	0.573	1.998	0.479
	2.998	0.880	2.998	0.746	2.998	0.631
	298K		308K		318K	
	value	std dev	value	std dev	value	std dev
q_i^{sat}	1.781	0.037	1.667	0.043	1.576	0.055
b	0.319	0.010	0.265	0.010	0.219	0.011
R^2	99.957%		99.950%		99.933%	

Table A.16. N_2 Isotherms and Langmuir model fitting parameters UiO-66

	UiO-66					
	298K		308K		318K	
	P (bar)	n(mol N_2/kg)	P (bar)	n(mol N_2/kg)	P (bar)	n(mol N_2/kg)
	0.000	0.000	0.000	0.000	0.000	0.000
	0.013	0.002	0.013	0.005	0.013	0.007
	0.200	0.028	0.199	0.028	0.198	0.027
	0.400	0.055	0.399	0.051	0.398	0.047
	0.599	0.082	0.599	0.075	0.598	0.067
	0.798	0.107	0.798	0.097	0.800	0.087
	0.998	0.133	0.999	0.119	0.999	0.104
	1.197	0.157	1.197	0.140	1.197	0.120
	1.398	0.182	1.398	0.159	1.398	0.136
	1.598	0.205	1.598	0.178	1.598	0.151
	1.797	0.230	1.797	0.198	1.797	0.168
	1.998	0.252	1.998	0.216	1.997	0.185
	2.998	0.356	2.999	0.305	2.998	0.270
	298K		308K		318K	
	value	std dev	value	std dev	value	std dev
q_i^{sat}	2.187	0.046	1.407	0.072	1.358	0.236
b	0.065	0.002	0.092	0.006	0.081	0.016
R^2	99.997%		99.965%		99.675%	

Table A.17. N_2 Isotherms and Langmuir model fitting parameters UiO-66-NH_2

	UiO-66-NH_2					
	298K		308K		318K	
	P (bar)	n(mol N_2/kg)	P (bar)	n(mol N_2/kg)	P (bar)	n(mol N_2/kg)
	0.000	0.000	0.000	0.000	0.000	0.000
	0.400	0.104	0.399	0.081	0.400	0.070
	0.598	0.145	0.598	0.114	0.598	0.098
	0.800	0.185	0.798	0.148	0.798	0.126
	1.000	0.224	0.998	0.181	0.998	0.154
	1.197	0.261	1.197	0.212	1.197	0.180
	1.398	0.297	1.398	0.243	1.398	0.205
	1.598	0.333	1.598	0.272	1.598	0.231
	1.797	0.368	1.797	0.302	1.797	0.255
	1.998	0.401	1.997	0.331	1.997	0.279
	2.999	0.556	2.998	0.463	2.998	0.396
	298K		308K		318K	
	value	std dev	value	std dev	value	std dev
q_i^{sat}	2.072	0.112	2.060	0.090	1.839	0.130
b	0.121	0.008	0.096	0.005	0.091	0.008
R^2	99.934%		99.971%		99.933%	

Table A.18. N_2 Isotherms and Langmuir model fitting parameters UiO-66-1,4-Naphthyl

	UiO-66-1,4-Naphthyl					
	298K		308K		318K	
	P (bar)	n(mol N_2/kg)	P (bar)	n(mol N_2/kg)	P (bar)	n(mol N_2/kg)
	0.000	0.000	0.000	0.000	0.000	0.000
	0.013	0.005	0.013	0.003	0.200	0.020
	0.199	0.025	0.198	0.021	0.399	0.035
	0.597	0.076	0.599	0.058	0.597	0.050
	0.799	0.097	0.800	0.077	0.798	0.064
	0.998	0.119	0.999	0.095	0.998	0.079
	1.197	0.139	1.197	0.110	1.197	0.093
	1.398	0.161	1.398	0.128	1.399	0.106
	1.598	0.179	1.598	0.143	1.598	0.117
	1.797	0.197	1.797	0.160	1.797	0.132
	1.997	0.216	1.997	0.173	1.997	0.145
	2.999	0.306	2.999	0.253	2.999	0.206
	298K		308K		318K	
	value	std dev	value	std dev	value	std dev
q_i^{sat}	1.450	0.092	1.594	0.142	1.050	0.099
b	0.089	0.007	0.062	0.006	0.081	0.009
R^2	99.957%		99.955%		99.906%	

Table A.19. N_2 Isotherms and Langmuir model fitting parameters UiO-66-NO_2

	UiO-66-NO_2					
	298K		308K		318K	
	P (bar)	n (mol N_2/kg)	P (bar)	n (mol N_2/kg)	P (bar)	n (mol N_2/kg)
	0.000	0.000	0.000	0.000	0.000	0.000
	0.198	0.036	0.199	0.029	0.198	0.026
	0.398	0.067	0.398	0.054	0.398	0.046
	0.597	0.097	0.597	0.078	0.597	0.066
	0.798	0.126	0.798	0.102	0.798	0.085
	0.998	0.153	0.999	0.124	0.999	0.102
	1.197	0.180	1.197	0.145	1.199	0.120
	1.398	0.206	1.397	0.166	1.399	0.137
	1.598	0.230	1.598	0.187	1.599	0.153
	1.797	0.256	1.797	0.207	1.797	0.172
	1.997	0.279	1.999	0.227	1.999	0.191
	2.999	0.387	2.998	0.323	2.999	0.268
	298K		308K		318K	
	value	std dev	value	std dev	value	std dev
q_i^{sat}	1.576	0.047	1.600	0.106	1.317	0.126
b	0.108	0.004	0.084	0.006	0.084	0.009
R^2	99.984%		99.951%		99.895%	

Table A.20. N_2 Isotherms and Langmuir model fitting parameters UiO-66-2,5-(OMe)$_2$

UiO-66-2,5-(OMe)$_2$						
	298K		308K		318K	
	P (bar)	n (mol N_2/kg)	P (bar)	n (mol N_2/kg)	P (bar)	n (mol N_2/kg)
	0.000	0.000	0.000	0.000	0.000	0.000
	0.400	0.087	0.200	0.041	0.200	0.032
	0.597	0.113	0.399	0.064	0.398	0.052
	0.799	0.151	0.597	0.093	0.598	0.067
	1.000	0.192	0.798	0.128	0.800	0.101
	1.197	0.221	0.998	0.154	1.001	0.122
	1.398	0.254	1.197	0.180	1.197	0.144
	1.598	0.283	1.398	0.203	1.398	0.164
	1.797	0.308	1.598	0.225	1.598	0.180
	1.997	0.335	1.797	0.250	1.797	0.196
	3.000	0.458	1.997	0.274	1.997	0.218
			2.998	0.374	2.997	0.297
	298K		308K		318K	
	value	std dev	value	std dev	value	std dev
q_1^{sat}	1.580	0.076	1.354	0.079	1.084	0.100
b	0.136	0.008	0.127	0.009	0.125	0.014
R^2	99.938%		99.921%		99.808%	

A.2 Chapter 4: Micro-Bed Breakthrough Study on a Set of Stable MOFs

A.2.1 *Instrument Design.*

A schematic of the instrument is provided in Figure A.4. and a photograph of the entire instrument contained within a fumehood is provided in Figure A.5. The instrument used in this study was designed for hazardous gas breakthrough testing, thus remote operation is used as opposed to more common methods of 4-way switching valve adjustment. Additionally, the entire apparatus is contained within a fumehood.

The components of construction are as follows:

1) MKS piMFC pressure insensitive mass flow controllers. The MFCs are calibrated for N2 flow where two are 100 sccm models and the third is a 10 sccm model.
2) MKS model 247D Four Channel Power Supply/Readout.
3) Hiden DSMS and Hiden MASoft (Hiden Isochema, Inc.).
4) Swagelok® VCR® face-seal gasket fittings.
5) PID controller, heat tape

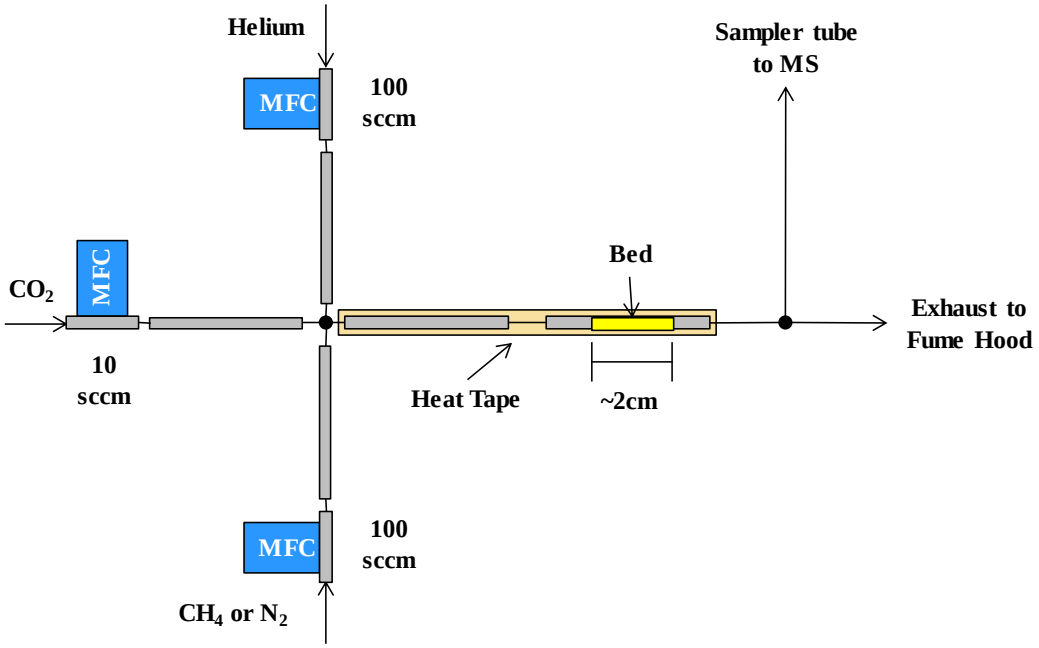

Figure A.4. Schematic of instrument. Flowrate capabilities are presented as values after gas correction factors have been applied.

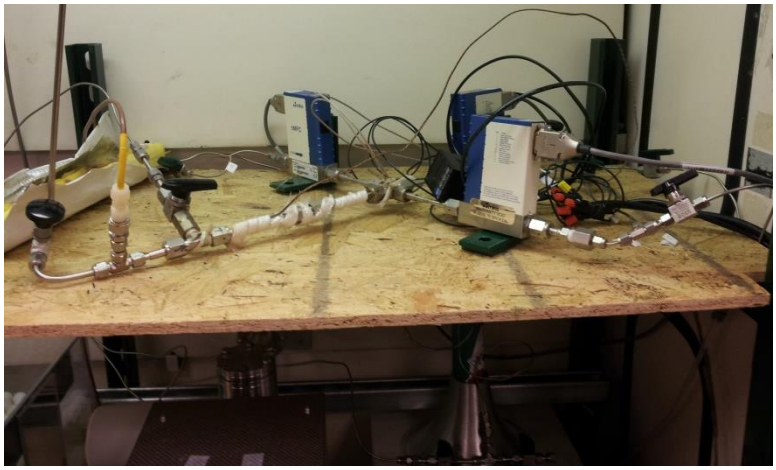

Figure A.5. Photograph of instrument ready for operation. Key features are PID temperature controller with heat tape and external thermocouple, three MKS piMFCs, and a heat traced line connected to a Hiden DSMS.

A.3 Mathematical Corrections for Simulation Comparisons

Multiple manipulations to the raw data were conducted in an automated and sequential manner to obtain the final results. This was only conducted for visual comparisons between samples and to simulation results. Any corrections did not affect calculation of dynamic capacities.

1) Raw data is recorded on m/z channels for the primary ion of each gas involved. Time required for measuring all channels is roughly 1.8 seconds.
2) Raw data is normalized to a 0-to-100 scale based on the maximum recorded value.
3) The raw, normalized data is used by a Mathematica program and a series of 4 functions are applied.
    a. Determine a timeframe sufficiently late in the experiment to be confidently considered "steady state." This is accomplished by taking the middle third of data between the maximum recorded signal and the end of the data record.
    b. Obtain a nonlinear model fit to the section of data using Eq. A.1. As can be expected on any 3 parameter fit, most R^2 values are 0.9999 or better.

$$y_t = z + (100 - \mathrm{z}) * \mathrm{a} * \exp[-\frac{\mathrm{b}(t - \mathrm{c_0})}{\mathrm{c_1} - \mathrm{c_0}}] \qquad \text{(A.1)}$$

where the fitting parameters are a, b, and z. The assigned variables are c_0 and c_1, which are the start and end times of the fitting interval, respectively. The known values are t and y.

c. For the time interval beyond 5% breakthrough, add the value obtained from Eq. A.2.

6)
$$y_{t,new} = y_t + \left(\left[z + (100 - \mathrm{z}) * \mathrm{a} * \exp[-\frac{\mathrm{b}(t_5 - \mathrm{c}_0)}{\mathrm{c}_1 - \mathrm{c}_0}]\right] - \left[z + (100 - \mathrm{z}) * \mathrm{a} * \exp[-\frac{\mathrm{b}(t - \mathrm{c}_0)}{\mathrm{c}_1 - \mathrm{c}_0}]\right]\right), when\ t > t_5 \quad \text{(A.2)}$$

where a, b, z, c_0 and c_1 are values obtained from previous fitting results. The values t_5 and y_t are determined from the raw, normalized data. The value t is the time for the recorded data point. The value $y_{t,new}$ is the resulting corrected data.

d. Normalize the corrected data to a 0-to-100 scale where the maximum value is selected at 3 minutes after the time where the maximum value in the raw data had occurred.

e. The corrected data, the raw data, and the fitted curve are plotted in order to visually verify the fit and correction.

i. Only in extreme cases, where external changes affected data collection, are corrections not accepted and the data rejected. Occasionally, these external effects were noted during data

collection, but the effects on final results were not apparent at the time.

ii. Examples where the correction was successful are given in Figure A.6. Examples where the corrections were unacceptable or failed are given in Figure A.7.

4) The corrected, normalized data obtained from the Mathematica code is imported to OriginPro 8.5.

a. As there are two or more data sets for each sample-experiment pair, the data was averaged using 'Average Multiple Curves' and an error obtained.

i. The averaged data was used for all further calculations.

5) The averaged curves are used for plotting, comparison to model results, and determination of gas uptake.

a. For calculations: the times for each sample are converted from seconds to minutes per gram of activated adsorbent.

i. Calculating the difference between the 5% breakthrough time for each sample-experiment pair and associated calibration-experiment pair allows for the basic determination of amount of gas adsorbed.

Examples	Information
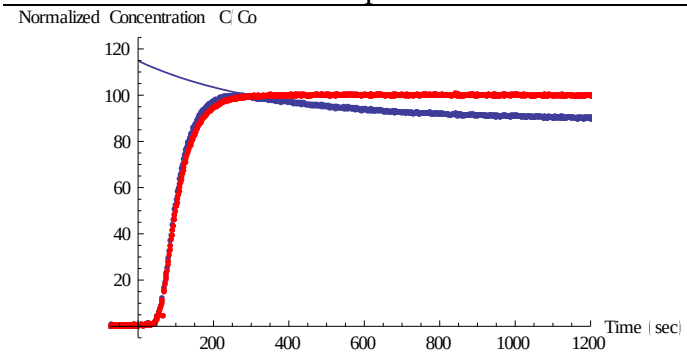	Raw data, corrected data, and correction fitting curve for CO_2 flowing through calibration bed.
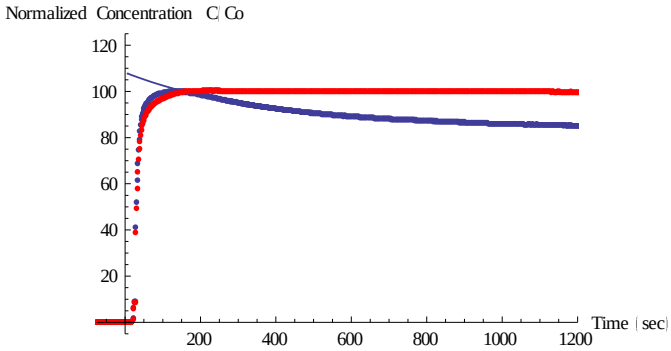	Raw data, corrected data, and correction fitting curve for N_2 flowing through calibration bed.
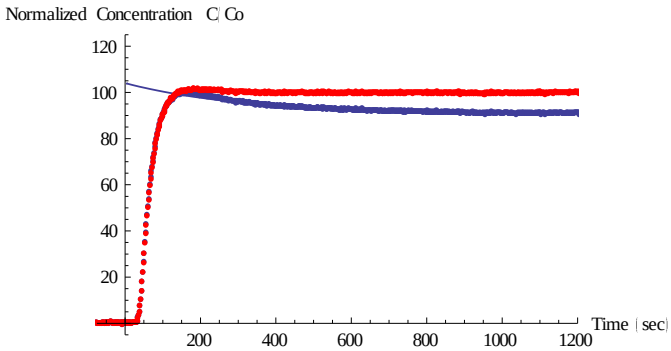	Raw data, corrected data, and correction fitting curve for CO_2 flowing through calibration bed.
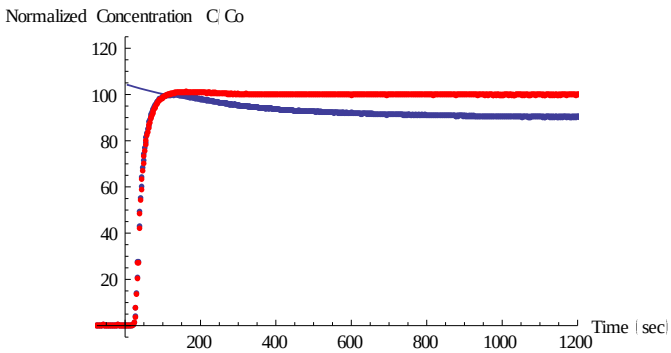	Raw data, corrected data, and correction fitting curve for N_2 flowing through calibration bed.

Figure A.6. Examples of successful or accepted corrections along with any required explanations.

Examples	Information
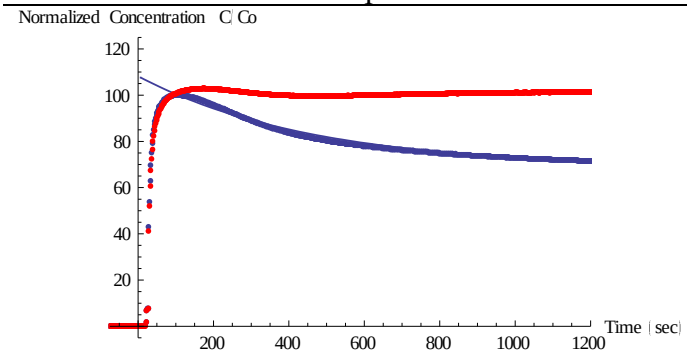	Raw data, corrected data, and correction fitting curve for N_2 flowing through calibration bed. Note the poor fit and uneven result, perhaps due to an unexpected change outside of the instrument such as shifting the fumehood sash position.
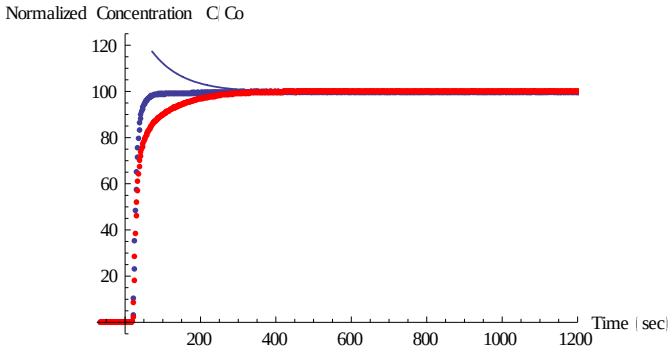	Raw data, corrected data, and correction fitting curve for N_2 flowing through calibration bed. Note the significant error introduced if the correction is used. A change in vacuum performance was noted between this and prior uses.
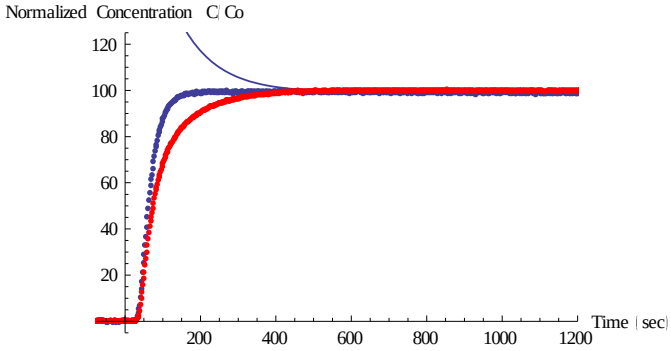	Raw data, corrected data, and correction fitting curve for CH_4 flowing through calibration bed. Note the significant error introduced if the correction is used. A change in vacuum performance was noted between this and prior uses.

Figure A.7. Examples of failed or unaccepted corrections along with any required explanations.

A.4 Offset Normalization

As the sample sizes and bed lengths varied, a difficulty arises in attempting to show all of the breakthrough results on a single plot. Comparing un-normalized breakthrough performance of two samples where one is half as massive would be incorrect and misleading. Standard normalization multiplies all time values by a factor,

but when one sample is half as heavy as another, this factor doubles. The result of this method of normalization is an artificially broadened breakthrough plot, a major problem when the plots are inherently diffuse.

An alternative method is to shift the data by only multiplying a single point by the normalization factor. What this accomplishes is that it maintains the shape of the breakthrough plots as they were measured in real-time while placing the results in positions for visual comparison of performance. By adding an offset factor, shown in Eq. A.3, to the data, this is accomplished. Results are shown in Figure A.8 through Figure A.18. Plots include error bars calculated from averaging of multiple curves as well as lines to help guide the eye to the locations of 5% and 100% C/C_o and time t=0.

7)
$$t_{expt,new} = (t_{expt} + (\frac{(1-m)t_{5,expt} - t_{5,cal}}{m})) * 1/60 \qquad \text{(A.3)}$$

where *t* is time, t_5 is the time at which normalized concentration equals five. Subscripts *cal, expt,* and *new* indicate calibration, experiment, and resulting offset curves, respectively.

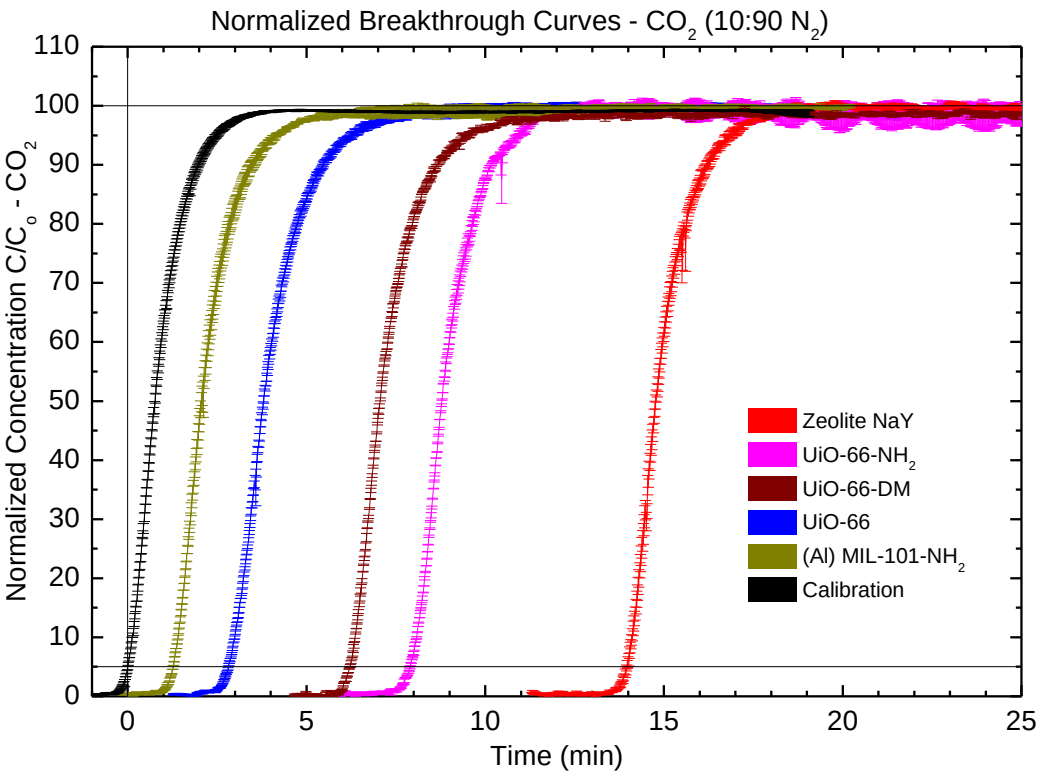

Figure A.8. Normalized CO_2 breakthrough curves offset along time axis to account for sample mass and allow for qualitative comparison of material performance.

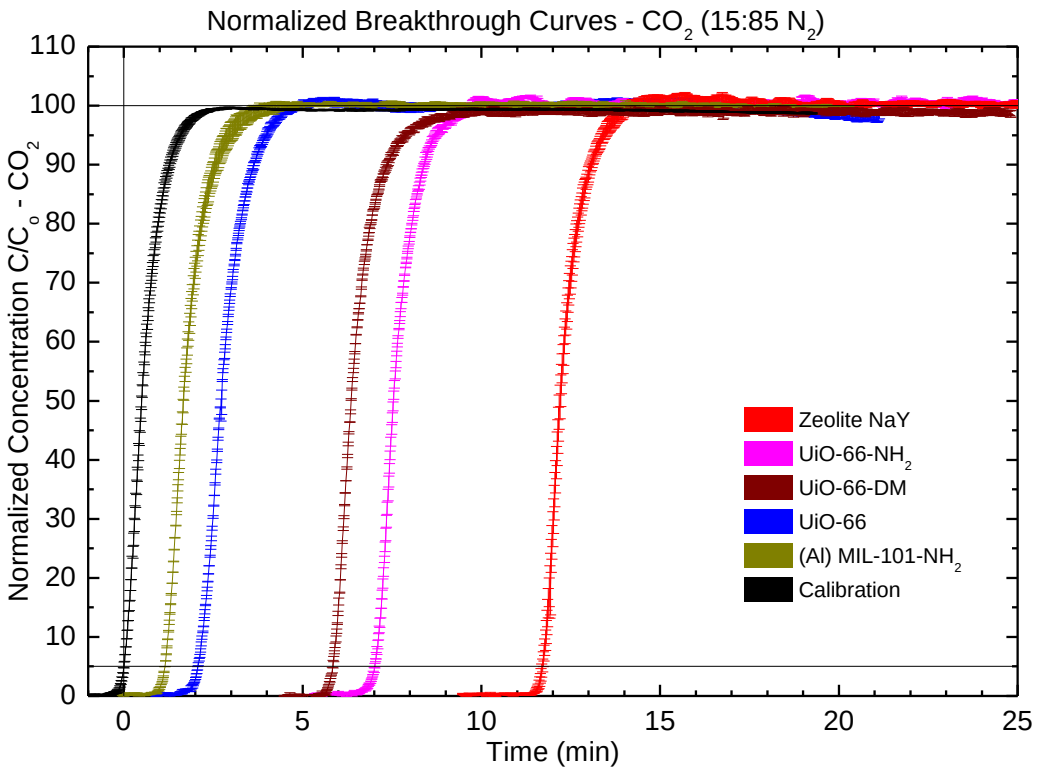

Figure A.9. Normalized CO_2 breakthrough curves offset along time axis to account for sample mass and allow for qualitative comparison of material performance.

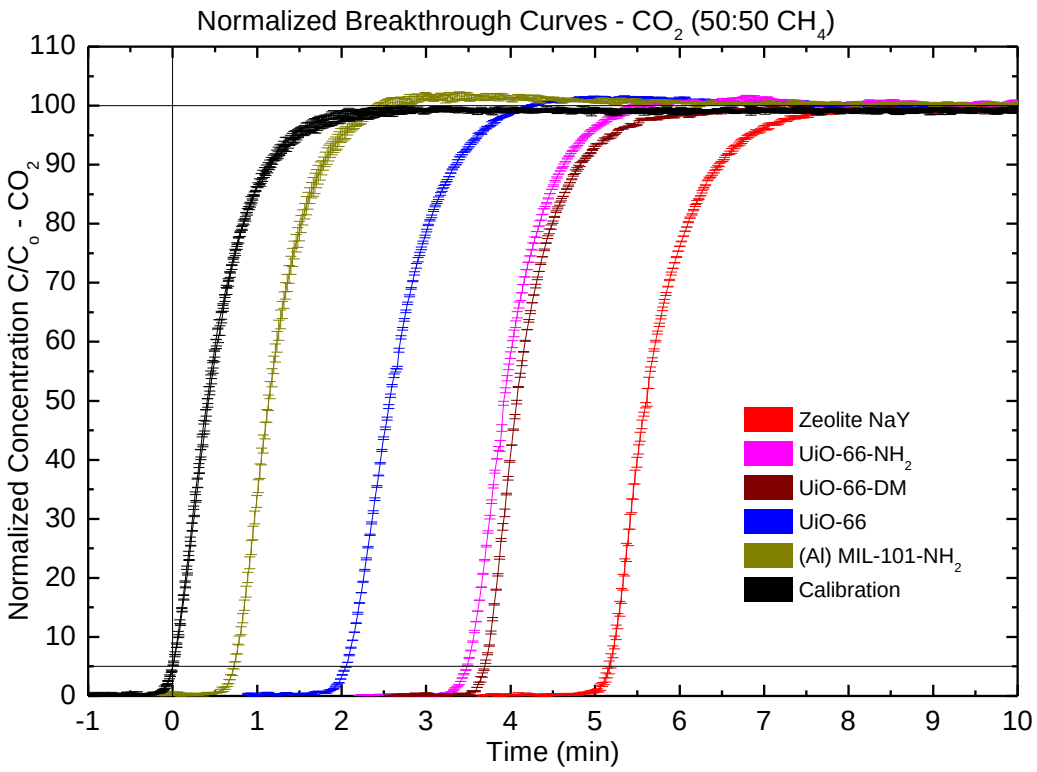

Figure A.10. Normalized CO_2 breakthrough curves offset along time axis to account for sample mass and allow for qualitative comparison of material performance.

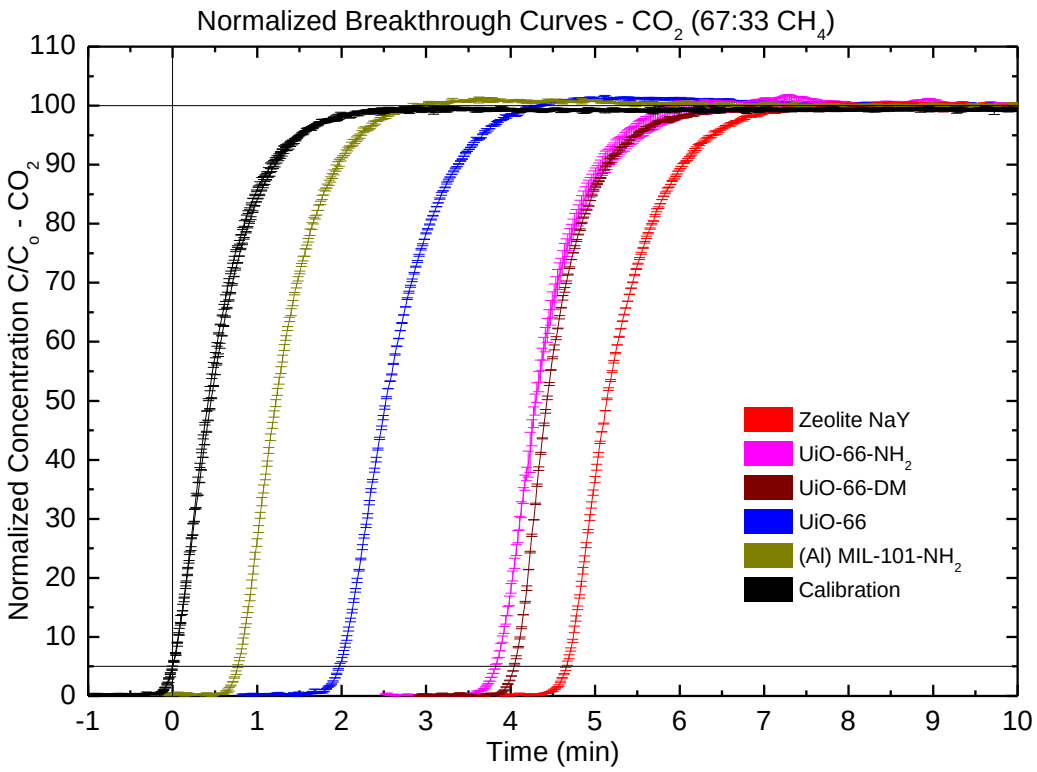

Figure A.11. Normalized CO_2 breakthrough curves offset along time axis to account for sample mass and allow for qualitative comparison of material performance.

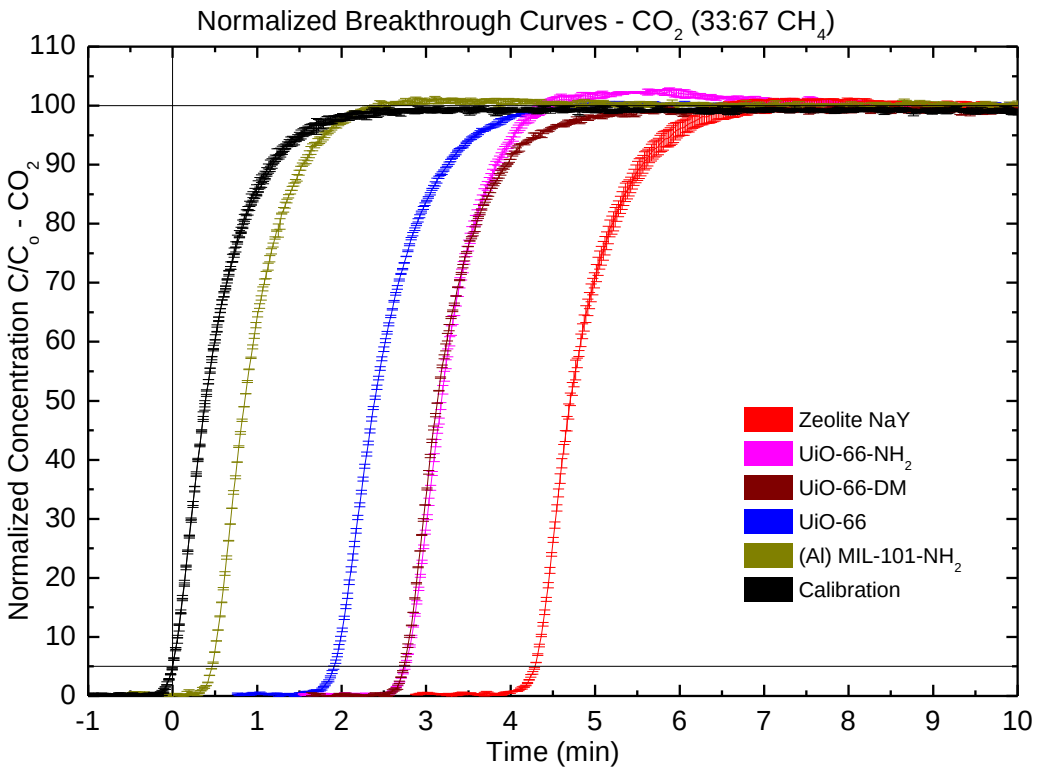

Figure A.12. Normalized CO_2 breakthrough curves offset along time axis to account for sample mass and allow for qualitative comparison of material performance.

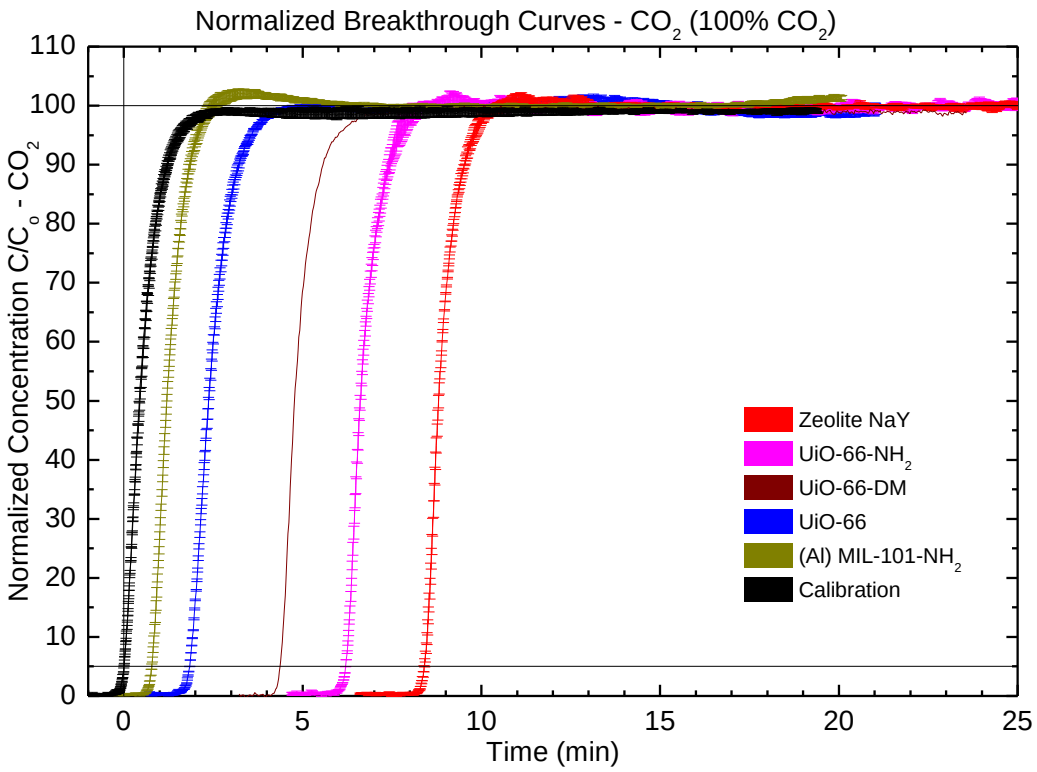

Figure A.13. Normalized CO_2 breakthrough curves offset along time axis to account for sample mass and allow for qualitative comparison of material performance.

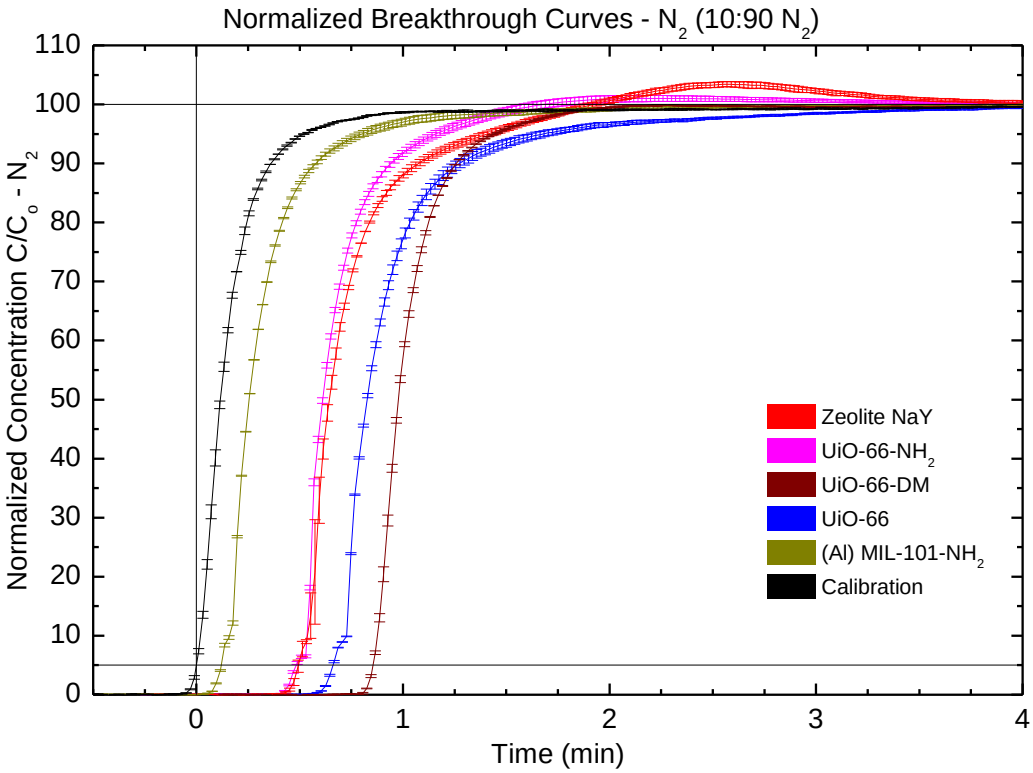

Figure A.14. Normalized N_2 breakthrough curves offset along time axis to account for sample mass and allow for qualitative comparison of material performance.

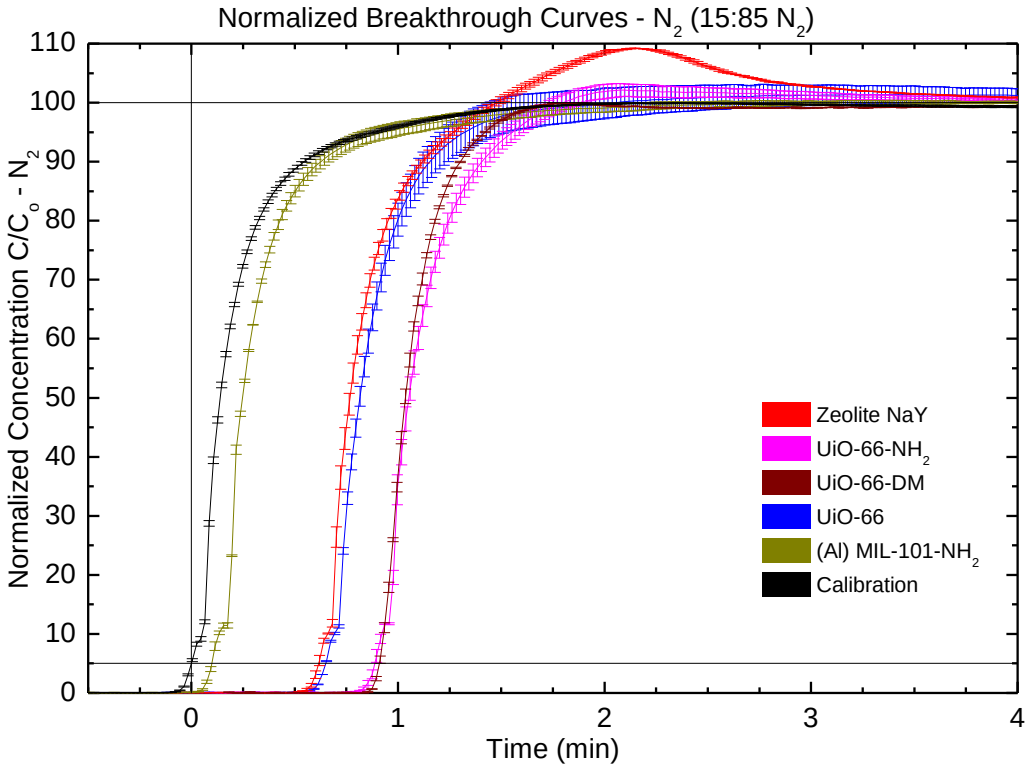

Figure A.15. Normalized N_2 breakthrough curves offset along time axis to account for sample mass and allow for qualitative comparison of material performance.

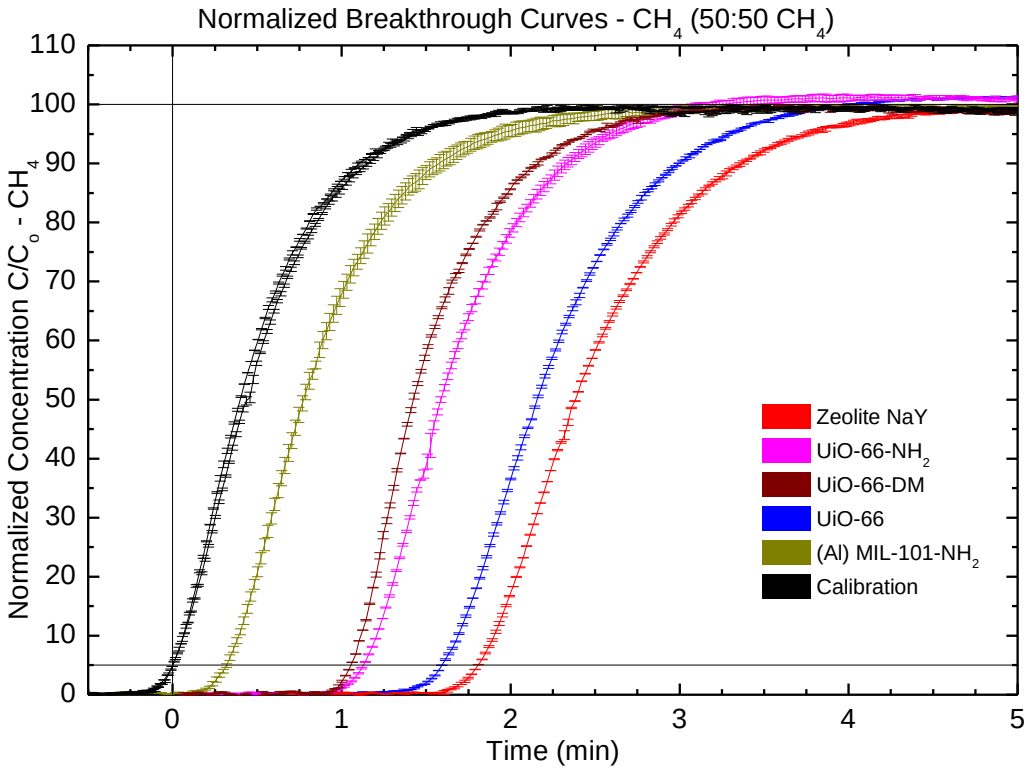

Figure A.16. Normalized CH_4 breakthrough curves offset along time axis to account for sample mass and allow for qualitative comparison of material performance.

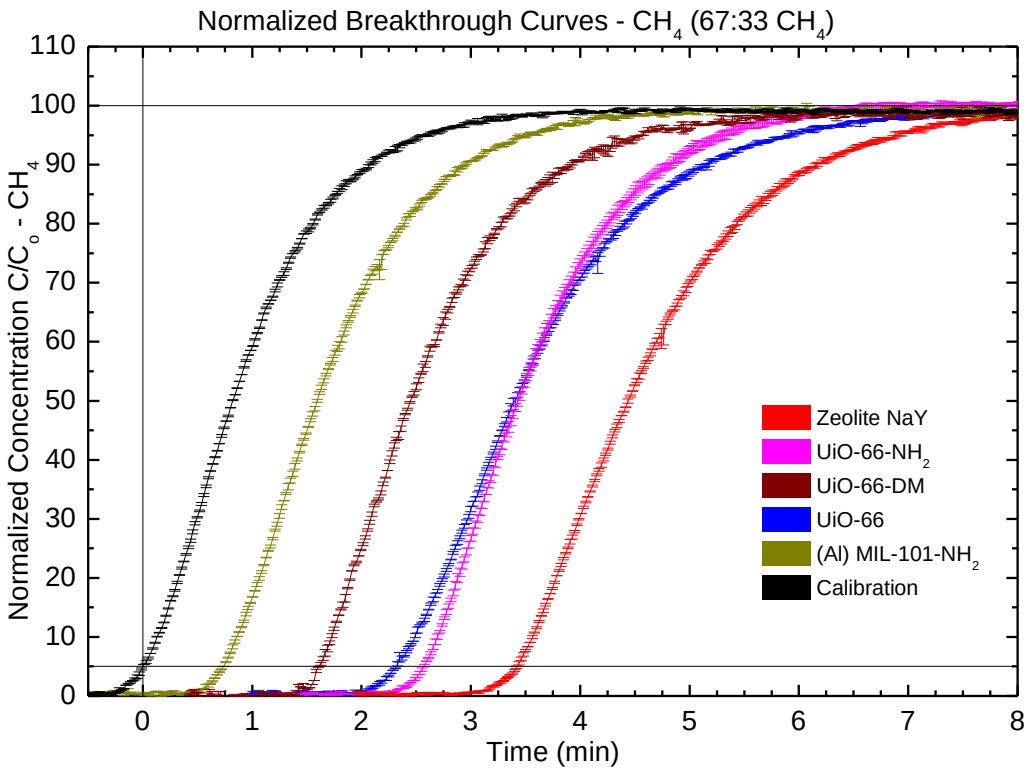

Figure A.17. Normalized CH_4 breakthrough curves offset along time axis to account for sample mass and allow for qualitative comparison of material performance.

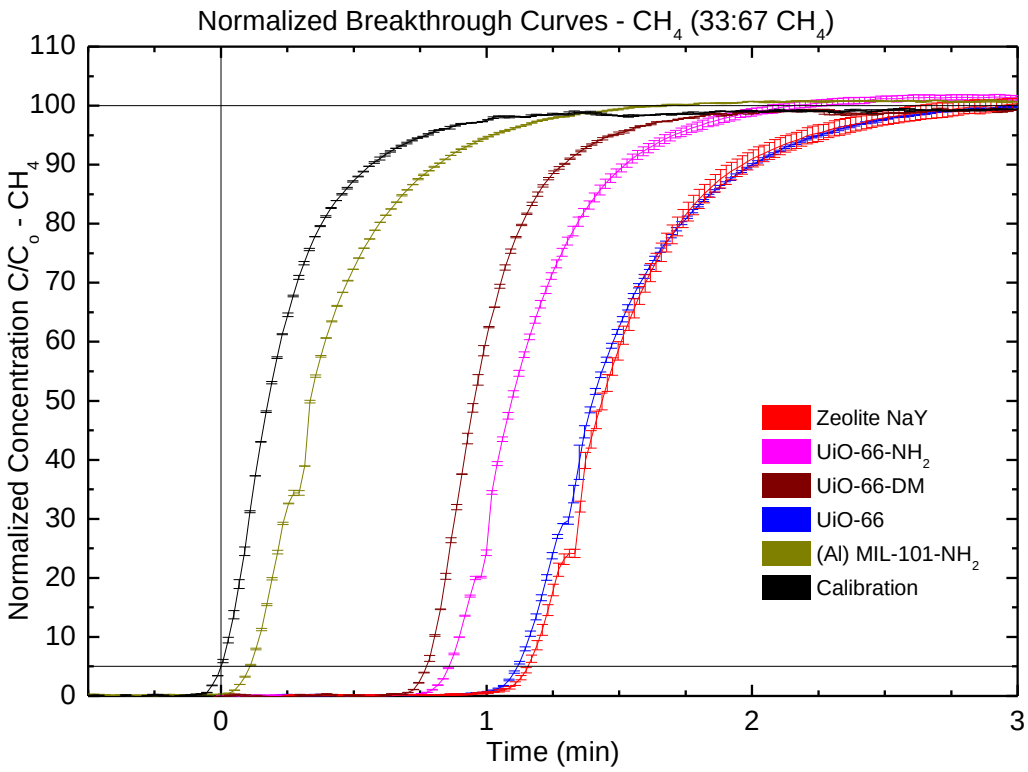

Figure A.18. Normalized CH_4 breakthrough curves offset along time axis to account for sample mass and allow for qualitative comparison of material performance.

A.5 Simulation Model Equations and Parameters

The model parameters are given in Table A.21 through Table A.23. The model equations are given in Eqs. A.4-A.20. In Figure A.19 through Figure A.23, the results of all simulation and experimental breakthrough data are plotted. Lines with symbols are obtained from simulations, solid lines are from experimental data, and dashed lines are from calibration data. Calibration results for each gas are in black and correspond to the experiment gas immediately following along the x-axis. Sample results are in color, CO_2 in red and N_2 or CH_4 in blue. Temperature rise, in K, is shown with pink squares and values are the same as is used for normalized concentration.

The results for the 67:33 CO_2:CH_4 mixture, shown in Figure A.22, were not sufficiently consistent nor reproducible. This is likely due to the low flowrate of CH_4, which approaches the lower limit for accurate operation of the MFCs as listed in the operating manual.

Table A.21. Parameters used in breakthrough simulation

Parameter	value	units	Description
D_e	0.025	cm^2/min	Effective Diffusivity
U_{total}	$2.4*10^3$	mJ/min/cm/K	Overall Heat Transfer Coefficient
Voidage	0.3	-	-
$2*R_p$	14	µm	Particle Radius
k_D (CO_2, N_2, CH_4)	42, 84, 420	1/min	Linear Driving Force Coefficient
R_g	$8.314*10^{-3}$	mJ/µmol/K	Ideal Gas Constant
C_p (CO_2, N_2, CH_4, He)	$6.42*R_g$, $5.5*R_g$, $5.23*R_g$, $2.5*R_g$	mJ/µmol/K	Molar Heat Capacity, Gas
C_p (solid)	920	mJ/g/K	Specific Heat Capacity, Solid
L	1.8	cm	Bed Length
V_o (at 35 sccm)	155	cm/min	Superficial Velocity

Table A.22. Isotherm parameters for Toth equation and Heat of Adsorption obtained from pure-component isotherms

CO_2		Zeolite NaY	UiO-66	UiO-66-NH_2	UiO-66-DM	NH_2-MIL-101(Al)
q_{sat}	mol/kg	6.56	18.08	11.61	14.3	15.13
b	1/bar	4.95	0.28	1.68	1.26	0.14
t	-	0.81	0.43	0.44	0.31	1
Q_{ads}	kJ/mol	-34	-25	-27.5	-27	-24
CH_4		Zeolite NaY	UiO-66	UiO-66-NH_2	UiO-66-DM	NH_2-MIL-101(Al)
q_{sat}	mol/kg	4.65	3.17	3.21	1.57	2.72
b	1/bar	0.09	0.19	0.35	0.31	0.07
t	-	1	1	1	1	1
Q_{ads}	kJ/mol	-16	-18	-21	-20.5	-17
N_2		Zeolite NaY	UiO-66	UiO-66-NH_2	UiO-66-DM	NH_2-MIL-101(Al)
q_{sat}	mol/kg	1.95	2.19	2.07	1.57	3.24
b	1/bar	0.06	0.06	0.12	0.07	0.04
t	-	1	1	1	1	1
Q_{ads}	kJ/mol	-9	-14	-17	-15	-12

Table A.23. Values used to obtain a match between simulation and calibration results. A and B are arbitrary values adjusted for each gas composition and flowrate to alter the error function step change shown in Eq. A.15

CO_2		N_2 or CH_4	
A	B	A	B
.30	1.5	.20	6.0
.26	2.0	.22	5.5
.25	2.5	3.0	10
.25	2.5	.20	2.5
.25	2.5	.25	1.5
.25	2.5	.26	5.0
.25	2.5	.26	5.0
.25	2.5	.20	6.0

A.6 Model Equations

The system of equations for prediction of equilibrium mixture adsorption amounts at various conditions using IAST is given in Eqs. A.4 and A.5. Assigned variables are P, y_1, and y_2 where subscripts indicate component 1: CO_2 and 2: N_2 or CH_4. If the sum of mole factions of the two adsorbing gases do not equate to unity, then it is assumed Helium accounts for the remainder as a non-interacting species existing only in the gas phase.

$$\int_0^{P_1^o} \frac{F_1(t)}{t}\,dt = \int_0^{P_2^o} \frac{F_2(t)}{t}\,dt\,, where\ F_i(t) = q_{i,eq}(p_i) \tag{A.4}$$

$$P_{tot} y_i = x_i P_i^o \tag{A.5}$$

The Toth equation is the isotherm chosen for solving Eq. A.6.

$$q_{i,eq}(P) = \frac{q_{i,sat} b_i P}{(1 + (b_i P)^t)^{1/t}} \tag{A.6}$$

The series of equations used to determine the amount of each component adsorbed at equilibrium according to IAST is given in Eqs. A.7-A.9.

$$n_i^o = \frac{q_{i,sat} b_i P_i^o}{(1 + (b_i P_i^o)^t)^{1/t}} \tag{A.7}$$

$$\frac{1}{n_{tot}} = \frac{x_1}{n_1^o} + \frac{x_2}{n_2^o} \tag{A.8}$$

$$n_{i,IAST} = n_{tot} x_i \tag{A.9}$$

The two component Langmuir isotherm is used to fit the mixture adsorption values obtained from IAST calculations (Eqs. A.10 and A.11).

$$P_{tot} y_i = p_i \tag{A.10}$$

$$q_{i,eq}(z,t) = \frac{q_{i,sat} b_i(z,t) * p_i(z,t)}{\left(1 + b_i(z,t) * p_i(z,t) + b_j(z,t) * p_j(z,t)\right)} \tag{A.11}$$

The equation for calculating selectivity is given in Eq. A.12.

$$S_{1,2} = \frac{x_1/y_1}{x_2/y_2} \tag{A.12}$$

The equations used in the simulation of breakthrough curves are given below. Equations are numerically integrated using the Automatic method in NDSolve in Mathematica.

Eq. A.13 gives the temperature dependence of the adsorption affinity parameter for Toth, Langmuir and multicomponent Langmuir equations.

$$b_i(z,t) = b_{i,o}\exp(\frac{-Q_i}{R_g}(\frac{1}{T(z,t)} - \frac{1}{T_o})) \tag{A.13}$$

Eq. A.14 gives the partial pressure for component *i*.

$$p_i(z,t) = R_g C_i(z,t) * T(z,t) \tag{A.14}$$

Eq. A.15 gives the error function to simulate step change of gas flow composition at bed inlet. The arbitrary parameters, *a* and *b*, are given in Table A.23.

$$\mathrm{f}(t,a,b) = \mathrm{erf}\big((b(t-a)-2)+1\big) * 0.5 \tag{A.15}$$

The Convection-Diffusion Equation for adsorptive breakthrough for each component is given in Eq. A.16.

$$\begin{aligned} D_{eff}\varepsilon\frac{\delta^2}{\delta z^2}C_i(z,t) \\ = \varepsilon\frac{\delta}{\delta z}(C_i(z,t) * u(z,t)) + \varepsilon\frac{\delta}{\delta t}C_i(z,t) + (1 \\ - \varepsilon)\rho_b\frac{\delta}{\delta t}\overline{q_i}(z,t) \end{aligned} \tag{A.16}$$

The differential adsorption behavior with Linear Driving Force assumption is given in Eq. A.17.

$$\frac{\delta}{\delta t}\bar{q}_i(z,t) = k_i(q_{i,eq}(z,t) - \bar{q}_i(z,t)) \tag{A.17}$$

The heat balance for the bed assuming instantaneous thermal equilibrium between adsorbent and gas is given in Eq. A.18.

$$\begin{aligned} C_{p,gas}A\varepsilon\frac{\delta}{\delta z}(C_{Tot}(z,t)*u(z,t)) + C_{p,gas}V_b\varepsilon\frac{\delta}{\delta t}(C_{Tot}(z,t)*T(z,t)) \\ + C_{p,solid}m(1-\varepsilon)\frac{\delta}{\delta t}T(z,t) + V_bU\varepsilon(T-T_o) \\ = \lambda V_b\varepsilon\frac{\delta^2}{\delta z^2}C_i(z,t) + \sum(-Q_i)(1-\varepsilon)\frac{\delta}{\delta t}\bar{q}_i(z,t) \end{aligned} \tag{A.18}$$

The total mass and momentum balances are simplified by Eq. A.19. This assumes constant flowrate through bed, where P_{inlet} is a value measured with each sample at the inlet MFC.

$$u(z,t) = \frac{V_o}{\varepsilon} * \left(\frac{T(z,t)}{T_o}\right) * \left(\left(\frac{100}{P_{inlet}} - 1\right) * \frac{z}{L} + 1\right)^{-1} \tag{A.19}$$

The total of concentration of all gas components is given in Eq. A.20.

$$C_{Tot}(z,t) = \sum C_i(z,t) \tag{A.20}$$

A.7 Simulation Results

In Figure A.19 through Figure A.23, the results of the simulations and their corresponding experimental data are shown.

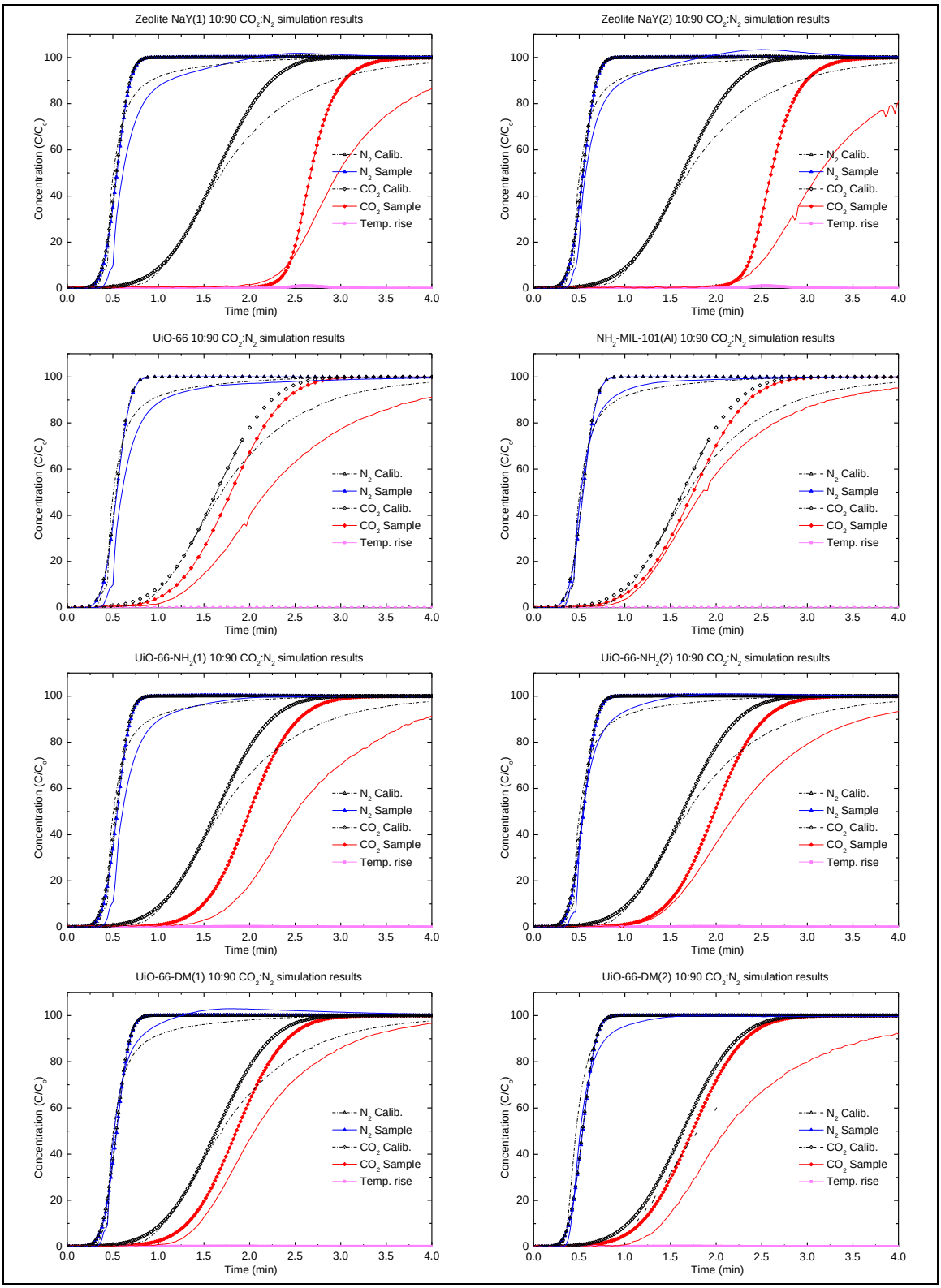

Figure A.19. Simulated and experimental breakthrough curves for 10:90 CO_2:N_2.

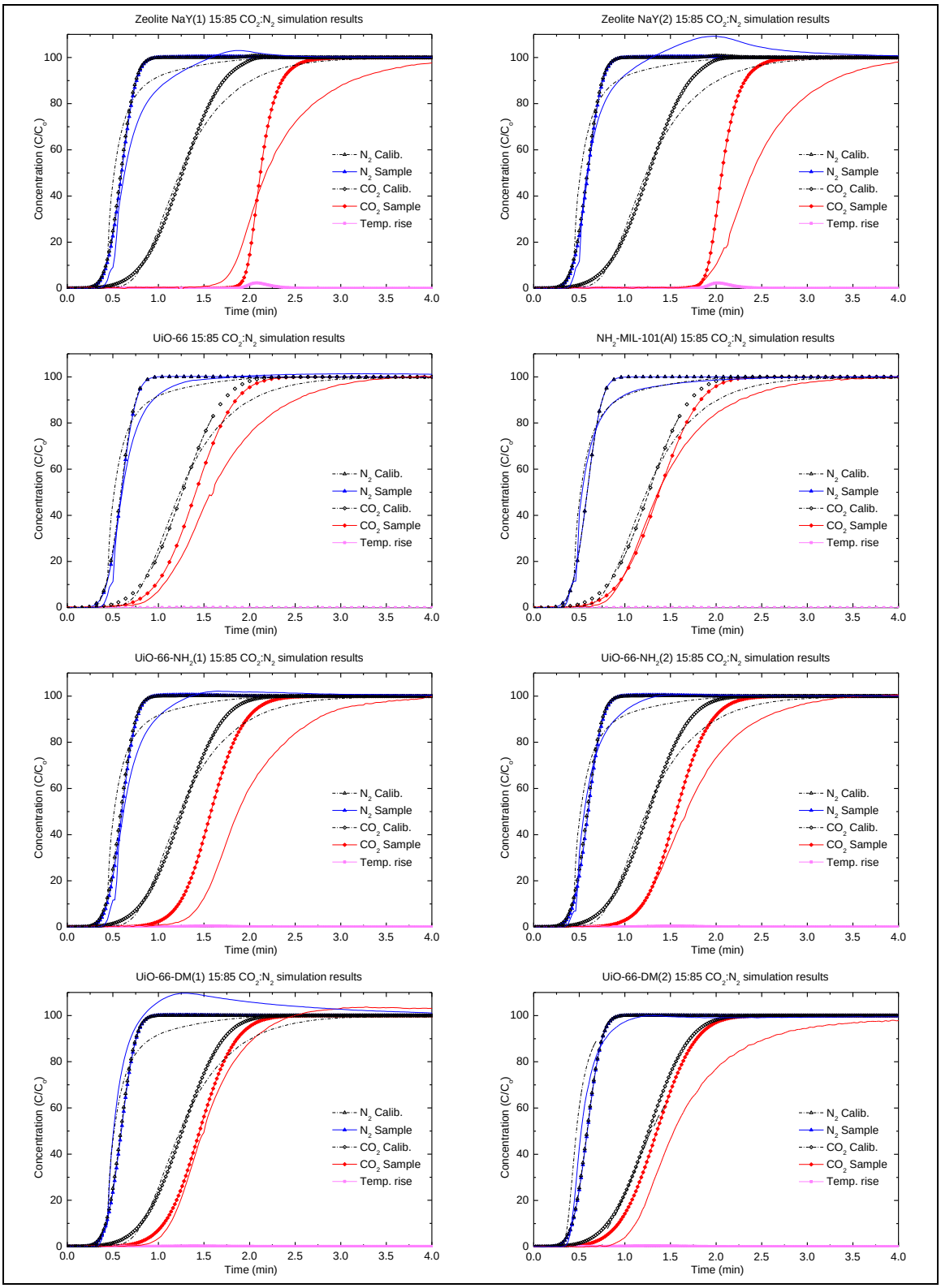

Figure A.20. Simulated and experimental breakthrough curves for 15:85 CO_2:N_2.

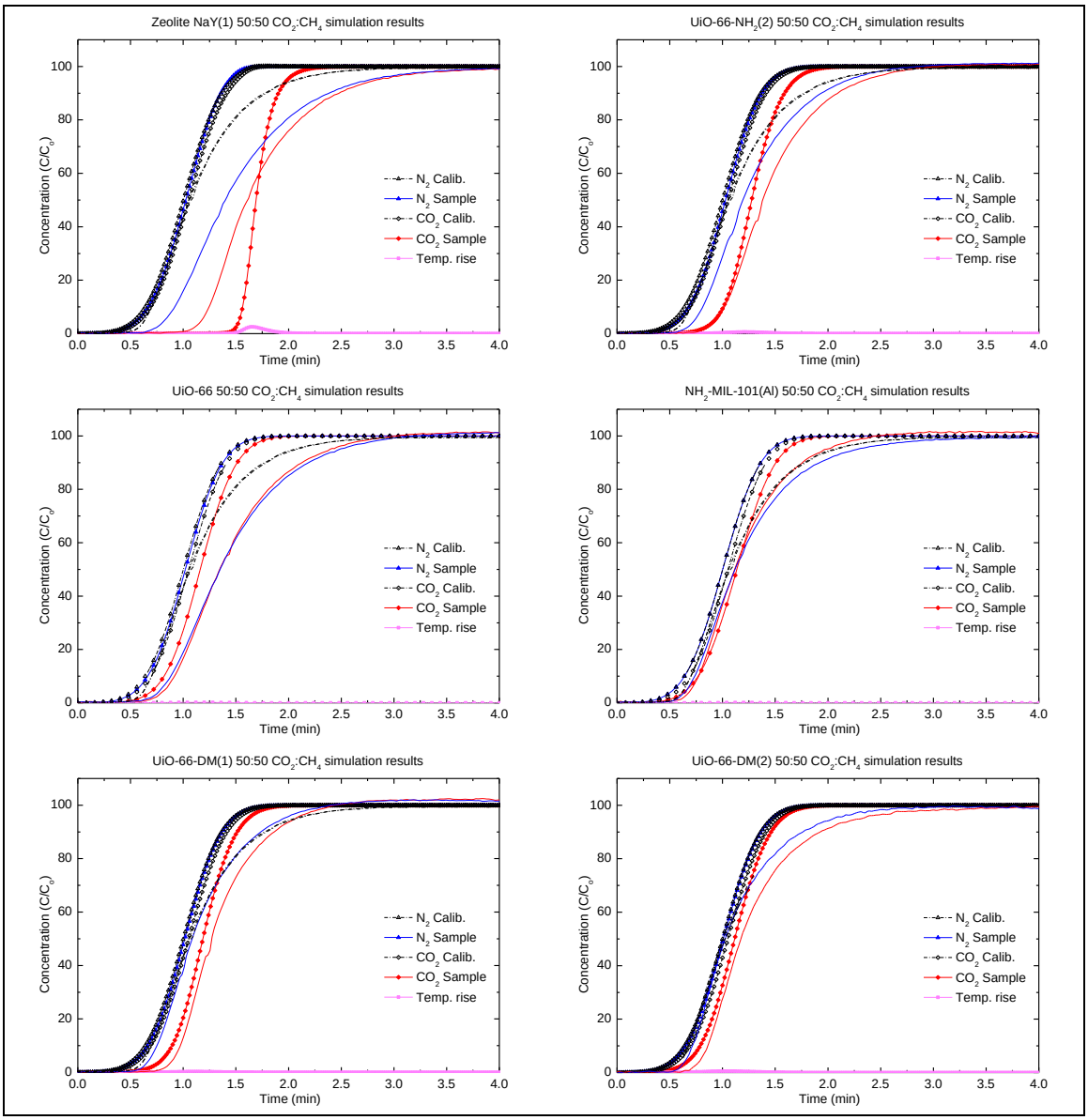

Figure A.21. Simulated and experimental breakthrough curves for 50:50 CO_2:CH_4.

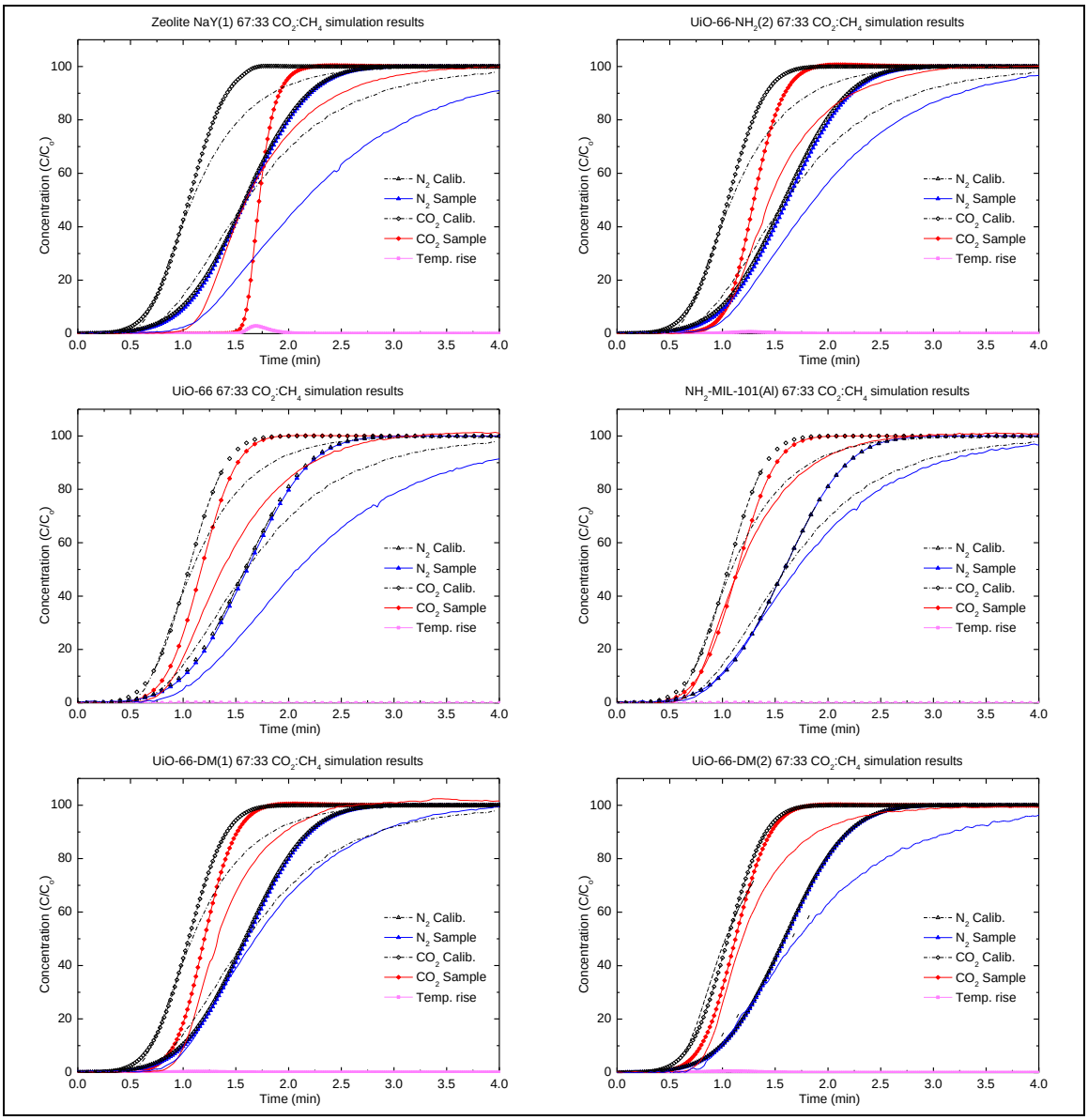

Figure A.22. Simulated and experimental breakthrough curves for 67:33 CO_2:CH_4.

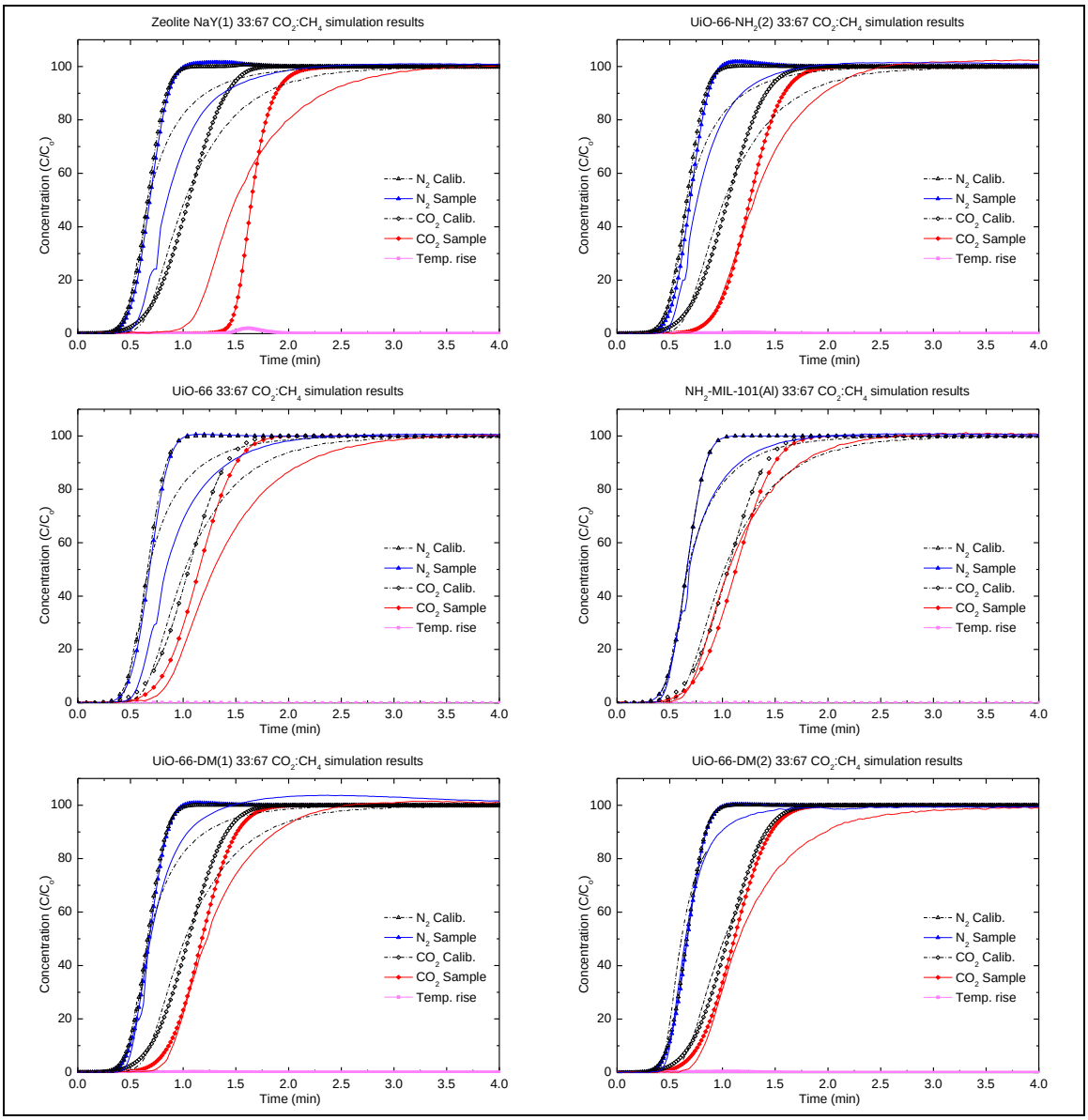

Figure A.23. Simulated and experimental breakthrough curves for 33:67 CO_2:CH_4.

APPENDIX B

DESIGN AND CONSTRUCTION OF A MODULAR ADSORPTION APPARATUS

B.1 Introduction

Equilibrium adsorption analysis is a slow process which places a constraint on the number of samples which can be studied. In order to correct for this apparent need, I designed an apparatus which measures adsorption via volumetric techniques. Among other needs and concerns is the future uses within the research group. The considerations include toxic gas adsorption, material handling, and chemical compatibility. Combining these factors produced a relatively low cost, reliable, and easy to use apparatus which has produced several important results within our research group.

B.1.1 *Design and Construction.*

B.1.1.1 Temperature Control

The simplest and most reliable method for obtaining temperature control is to immerse the sample cell in a temperature controlled bath. The two major fluids used to maintain temperature control are water and mineral oil. The bath is then controlled to a set temperature by a circulating pump with a heating and/or cooling element. The system is oriented so that the outlet of circulation pump is directed towards the two side-by-side sample cells.

The choice between water and mineral oil is dictated by required maximum operating temperatures required. Water is limited to roughly 80°C as the rate of loss by

evaporation rises rapidly, leading to a need to replenish with additional water, a process which affects the temperature. Evaporative losses can be reduced by reducing the effective surface area of the bath, such as using a floating layer of hollow polypropylene spheres. Mineral oil can be used up to 200°C or higher, as limited by the age-dependent flash point of the oil. A more practical advantage to water over oil is the ease of clean-up, storage, and transport. Water can be simply drained, wiped away, and left to dry in open air in order to prepare the bath for transport or handle the sample cells, an option not available for oil.

The heat transfer fluid must be contained in some vessel. The most common option is a stainless steel tub liner in a rigid box, which can provide sufficient insulation to handle over 200°C bath temperatures. Tubing and valves can be bolted directly to the body of the container. Another option is a plastic vessel, such as acrylic, which is lighter but cannot handle above 70°C due to the adhesives used. Additionally, tubing and valves must be attached to a panel which is adhered to the bath wall.

B.1.1.2 Pressure Control

The measured variable in this apparatus is the cell pressure. Two high accuracy pressure transducers are used for each unit, one for a reference cell and the second for the sample cell (thus a total of 4). The transducers are Honeywell model Super TJE with absolute measurement range from 0-100 psi. These units are factory calibrated along with a model SC2000 signal conditioner.

In order to minimize the leak rate of the cells, the valves and sealing surfaces must be of the highest quality. Naturally, if gas leaks out of the cells, the measurements taken will be invalid. Any tubing fitting which will be disconnected after first

construction must be VCR® face seal gaskets and the valves are long-stem, stainless steel bellows valves. The long stem is useful to allow for the water bath to be filled to a higher level. It was noted that slight rusting occurs to the stem, which are carbon steel, while the body is stainless steel.

B.1.1.3 Material Compatibility

The gases used for adsorption experiments in our research group have included: CO_2, CH_4, N_2, He, H_2S, CO, C_2H_2, C_2H_4, C_2H_6, nC_4H_{10}, iC_4H_{10}, among others. Of immediate note are the toxic gases, CO and H_2S, and the explosive gas, acetylene, which require careful handling. The safest method for handling such gases is to contain everything (apparatus, supply, and exhaust) within the confines of a fume hood. H_2S is highly damaging to most grades of steel and cannot be used without special alloys at all exposed surfaces. CO and C_2H_2 dangerously interact with Ni and Cu VCR® gaskets, respectively, which is easily avoided by using the alternate gaskets. The Ni and Cu gaskets are preferred over SS gaskets when the fitting is to be used often, as repeatedly using SS gaskets will damage the sealing surface, and they are significantly softer metals and easier to tighten. Cu gaskets have a temperature limit of 205°C, which can be a concern during sample activation.

The materials which may be exposed to the experiment gas are: SS316, carbon steel, Cu, Ni, Al, and graphite.

B.1.1.4 Sample Handling

Samples are loaded into a holder, such as a sintered stainless steel filter, with the open end capped by a piece of aluminum foil just large enough to remain in place. This sample cell can be weighed before or after experiment, allowing flexibility if fast loading

is required. Also, the sample powder can be loaded "wet," a process which utilizes a volatile solvent to protect samples from air exposure. The sample cell is sealed and the entire unit is connected to a vacuum line . This vacuum line is a separate set of fittings from the water bath manifold, as typical activation requires temperatures over 70°C. The sample cell is wrapped in heat tape allowing for effective heating to activation temperatures. Heat and vacuum are slowly applied to the sample cell where heat is controlled by a PID controller and vacuum is monitored via the pressure transducers.

B.1.1.5 Construction

Construction is a straightforward process which simply follows the recommendations provided in the tubing and fittings manuals supplied by vendors. The valves and pressure transducers are separated from the rest of the system by fritted filter VCR® gaskets.

The first things to consider is the layout of the gas manifold, which controls the gas flows from supply tanks and to vents and vacuum lines. To anchor the manifold, two layers of adhesive backed acrylic panels were used to provide a solid platform. The panels had holes drilled of two different sizes to match the head and body of a bolt, which was then sandwiched between the panels and the water bath. These bolts allow the manifold to be anchored to the bath via tubing clamps.

The connection between the manifold and each unit requires careful tube bending and welding. The most reliable approach is to use three bends perpendicular to each other so that the position of the unit can be tuned later.

Finally, the sample cells should be slightly elevated from the plane upon which the unit rests, in order to allow for space for heating tape or heat transfer fluid to envelop

the cell. This can be best achieved by placing the cell at a right angle to the rest of the unit and then angle it upwards roughly 30 degrees.

B.1.2 *Operation.*

B.1.2.1 Calibration

Calibration of this unit was conducted with Helium at a series of increasing pressures and with various filler materials to occupy the dead volume of the cells. Useful materials include glass beads, aluminum foil, and small pieces of metal. By weighing, the volume of these materials can be determined, and thus the volume of each sample chamber can be adjusted. When at least two different materials plus an empty run are conducted, the dead volume of each cell can be determined with confidence by calculations using the ideal gas law. It should be noted that the orientation of the valve can have an effect of several mL, due to internal construction.

B.1.2.2 General Use

Samples are prepared, loaded, and sealed into the sample cells. Typically, 50mg is sufficient. The entire unit is evacuated and the sample cell is heated, which, after some time, will activate the sample. Since initial and final weights cannot be taken of the entire unit, activation cannot be directly observed but must be determined by some other means. The pressure transducers are zeroed to the achieved vacuum, the valves are sealed, and the cell is allowed to cool. The units are then placed in the water bath, attached to the manifold, and the upstream sections are evacuated. At this point, the system is at set temperature and best achievable vacuum, and then the experiment is run.

The experiment consists of a series of incremental pressurizations of the reference cell, brief pause for equilibration, then transfer of gas from reference to sample cells. The

pressure can be controlled by opening the reference cell valve rapidly, via control at the regulator, or by careful partial evacuation. The former is preferable as supply line leaks are common, thus positive pressure in the supply lines is recommended. By recording the initial and final pressures of the two cells, a mass balance can be used to calculate the amount of gas adsorbed via an equation of state. A wait period of at least 1 hour is necessary for thermal equilibration of the sample cell after the initial near-adiabatic adsorption process. Eventually, the increments will approach the maximum measureable pressure (100 psia or ~6.5 bar), at which point the experiment can be conducted in reverse, repeated, or brought to lab pressure for removal.

B.1.2.3 Calculations

In order to calculate the amount of gas adsorbed, a mass balance must be conducted on the two cells of each unit. The void volume of the cell is known and the mass and density of the sample pan and aluminum foil cover are also known, allowing for easy subtraction of the occupied, non-adsorbing volume. The mass of sample can be obtained either from other experiments, measurement of dry mass immediately after experiment, or approximation from a TGA curve. The density of the sample is not critical to the calculation, but does fall in a gray area of definitions for adsorption[1]. By subtracting the volume of the materials in the sample cell, the number of moles in the gas phase can be determined. The mass balance between the reference and sample cells provides what amount of gas should have passed from the one chamber to the other. This amount of "missing" gas can only be attributed to adsorption, thus yielding the amount of gas adsorbed since the previously measured point. Larger pressure "steps" increase the accuracy of each measured adsorption point.

B.2 Observations and Discussion

This instrument had a number of benefits but also a number of drawbacks. The primary benefits are flexibility, accuracy, portability, and the capability to complete two measurements simultaneously in one day. This was heavily utilized by myself to screen samples of the UiO-66 family of materials. After a number of samples were measured, concerns about the accuracy were brought up by myself and I ceased using the instrument. Later literature would reveal the actual cause of the inconsistency was inherent to the adsorbent material, not the instrument. Other group members have successfully used this instrument for CO and acetylene adsorption and desorption measurements.

The drawbacks of this instrument include the manual operation, decreasing accuracy with smaller pressure steps, and slow thermal equilibration rate. The first drawback stems from the fact that humans are prone to error. The second is especially relevant in the low pressure regime where much of the most interesting and relevant adsorption occurs. Fitting an isotherm model can help alleviate this problem. The third drawback stems from the non-forced nature of the temperature control bath. The sample temperature is not measured directly and heat transfer rates are very low, which means the likely sample temperature when data is recorded is slightly above the bath setpoint.

B.3 References

1. Mertens, F. O. (2009). *Determination of absolute adsorption in highly ordered porous media.* Surface Science, **603**(10-12): p. 1979–1984.